Fall 12-21-2011

The Nanoaquarium: A Nanofluidic Platform for in SiTu Transmission Electron Microscopy in Liquid Media

Joseph M. Grogan
University of Pennsylvania, jgrogan@seas.upenn.edu

The Nanoaquarium: A Nanofluidic Platform for in SiTu Transmission Electron Microscopy in Liquid Media

Abstract
There are many scientifically interesting and technologically relevant nanoscale phenomena that take place in liquid media. Examples include aggregation and assembly of nanoparticles; colloidal crystal formation; liquid phase growth of structures such as nanowires; electrochemical deposition and etching for fabrication processes and battery applications; interfacial phenomena; boiling and cavitation; and biological interactions. Understanding of these fields would benefit greatly from real-time, *in situ* transmission electron microscope (TEM) imaging with nanoscale resolution. Most liquids cannot be imaged by traditional TEM due to evaporation in the high vacuum environment and the requirement that samples be very thin. Liquid-cell *in situ* TEM has emerged as an exciting new experimental technique that hermetically seals a thin slice of liquid between two electron transparent membranes to enable TEM imaging of liquid-based processes. This work presents details of the fabrication of a custom-made liquid-cell *in situ* TEM device, dubbed the nanoaquarium. The nanoaquarium's highlights include an exceptionally thin sample cross section (10s to 100s of nm); wafer scale processing that enables high-yield mass production; robust hermetic sealing that provides leak-free operation without use of glue, epoxy, or any polymers; compatibility with lab-on-chip technology; and on-chip integrated electrodes for sensing and actuation. The fabrication process is described, with an emphasis on direct wafer bonding. Experimental results involving direct observation of colloid aggregation using an aqueous solution of gold nanoparticles are presented. Quantitative analysis of the growth process agrees with prior results and theory, indicating that the experimental technique does not radically alter the observed phenomenon. For the first time, *in situ* observations of nanoparticles at a contact line and in an evaporating thin film of liquid are reported, with applications for techniques such as dip-coating and drop-casting, commonly used for depositing nanoparticles on a surface via convective-capillary assembly. Theoretical analysis suggests that the observed particle motion and aggregation are caused by gradients in surface tension and disjoining pressure in the thin liquid film.

Degree Type
Dissertation

Degree Name
Doctor of Philosophy (PhD)

Graduate Group
Mechanical Engineering & Applied Mechanics

First Advisor
Haim H. Bau

Keywords
in situ electron microscopy, wet electron microscopy, wafer bonding, nanofluidics, device fabrication, particle aggregation

THE NANOAQUARIUM: A NANOFLUIDIC PLATFORM FOR *IN SITU* TRANSMISSION ELECTRON MICROSCOPY IN LIQUID MEDIA

Joseph M. Grogan

A DISSERTATION

in

Mechanical Engineering and Applied Mechanics

Presented to the Faculties of the University of Pennsylvania

in

Partial Fulfillment of the Requirements for the

Degree of Doctor of Philosophy

2011

Supervisor of Dissertation

_____

Haim H. Bau

Professor, Mechanical Engineering and Applied Mechanics

Graduate Group Chairperson

_____

Jennifer R. Lukes

Associate Professor, Mechanical Engineering and Applied Mechanics

Dissertation Committee

Haim H. Bau, Professor, Mechanical Engineering and Applied Mechanics

Robert W. Carpick, Professor, Mechanical Engineering and Applied Mechanics,
Materials Science and Engineering

Jennifer R. Lukes, Associate Professor, Mechanical Engineering and Applied Mechanics

THE NANOAQUARIUM: A NANOFLUIDIC PLATFORM FOR *IN SITU* TRANSMISSION ELECTRON MICROSCOPY IN LIQUID MEDIA

Acknowledgments

I would like to foremost thank my advisor, Dr. Haim H. Bau, for his guidance, support, and encouragement. It was a long journey to get to this point, and he was with me all the way. I am grateful for the spoken lessons on topics that ranged from research to the classroom to conferences, as well as the unspoken example that he set as an impassioned researcher. Many thanks to my committee members, Dr. Robert W. Carpick and Dr. Jennifer R. Lukes; the feedback that I received after my thesis proposal was instrumental in shaping my thesis and helped to prepare me for the science world post-Penn. I would like to thank Dr. Howard H. Hu and all of the past and current members of the Bau & Hu research groups, especially Drs. Mark Arsenault, Robert Hart, Mian Qin, Michael Schrlau, Jason Thompson, Hui Zhao, Changchun Liu, and future Drs. Sean Anderson, Tong Gao, Michael Norton, Nicholas Schneider, and Jinzhou Yuan, for making my time as a doctoral student intellectually, culturally, and socially stimulating. Thanks to the entire faculty, students, and staff of the department of Mechanical Engineering and Applied Mechanics and throughout the School of Engineering and Applied Science. Special thanks to Maryeileen B. Griffith, Susan Waddington-Pilder, and Olivia Brubaker for all of their help throughout the years. Thanks to the student organizations MEGA, GSEG, and GAPSA, and the wonderful friendships they produced.

Dr. Frances M. Ross of the IBM T. J. Watson Research Center provided encouragement and advice throughout, and collaborated on electrochemical studies. Fabrication was carried out at the Cornell NanoScale Facility, a member of the National Nanotechnology Infrastructure Network, which is supported by the National Science

Foundation (Grant ECS-0335765). The facility's staff graciously shared their wealth of expertise. Additional fabrication was carried out at the Wolf Nanofabrication Facility at the University of Pennsylvania. The WNF has made great strides under the direction of Dr. Iulian Codreanu. Electron microscopy was performed at the Penn Regional Nanotechnology Facility. Dr. Lolita Rotkina of the Penn Regional Nanotechnology Facility provided valuable assistance with electron microscopy. Sumant Sood of SUSS MicroTec shared expertise on wafer bonding. Peter Szczesniak of the MEAM Machine Shop at the University of Pennsylvania constructed the device holder for use at Penn. Dr. Brian Edwards (Department of Electrical & Systems Engineering, University of Pennsylvania) provided assistance with electromagnetic calculations. Xingchen Ye and Professor Christopher B. Murray of the Chemistry department and Materials Science department at the University of Pennsylvania provided gold nanorods and advice throughout. Professor Yale Goldman (Department of Physiology, University of Pennsylvania) provided assistance with biological specimen. Thank you to Professor Kathleen J. Stebe and Dr. Lorenzo Botto (Department of Chemical and Biomolecular Engineering, University of Pennsylvania) for helpful discussions and input.

This work was supported, in part, by the NSF-NIRT (CBET 0609062), NSF-NBIC (NSF NSEC DMR-0425780), and the Nanotechnology Institute of Ben Franklin Technology Partners of Southeastern Pennsylvania.

Finally, I would like to thank my parents Ginny & Joe, my sister Katie, her husband Mario, my girlfriend Julia, and my extended family. My grandparents (Grogan and Valentino) instilled a love of learning in our family that continues to percolate

through the generations. I share this accomplishment with you all and could not have achieved any of it without your love and support. Also, thank you to my cat May for keeping me company while I wrote most of this dissertation.

Abstract

THE NANOAQUARIUM: A NANOFLUIDIC PLATFORM FOR *IN SITU* TRANSMISSION ELECTRON MICROSCOPY IN LIQUID MEDIA

Joseph M. Grogan

Haim H. Bau

There are many scientifically interesting and technologically relevant nanoscale phenomena that take place in liquid media. Examples include aggregation and assembly of nanoparticles; colloidal crystal formation; liquid phase growth of structures such as nanowires; electrochemical deposition and etching for fabrication processes and battery applications; interfacial phenomena; boiling and cavitation; and biological interactions. Understanding of these fields would benefit greatly from real-time, *in situ* transmission electron microscope (TEM) imaging with nanoscale resolution. Most liquids cannot be imaged by traditional TEM due to evaporation in the high vacuum environment and the requirement that samples be very thin. Liquid-cell *in situ* TEM has emerged as an exciting new experimental technique that hermetically seals a thin slice of liquid between two electron transparent membranes to enable TEM imaging of liquid-based processes. This work presents details of the fabrication of a custom-made liquid-cell *in situ* TEM device, dubbed the nanoaquarium. The nanoaquarium's highlights include an exceptionally thin sample cross section (10s to 100s of nm); wafer scale processing that enables high-yield mass production; robust hermetic sealing that provides leak-free operation without use of glue, epoxy, or any polymers; compatibility with lab-on-chip

technology; and on-chip integrated electrodes for sensing and actuation. The fabrication process is described, with an emphasis on direct wafer bonding. Experimental results involving direct observation of colloid aggregation using an aqueous solution of gold nanoparticles are presented. Quantitative analysis of the growth process agrees with prior results and theory, indicating that the experimental technique does not radically alter the observed phenomenon. For the first time, *in situ* observations of nanoparticles at a contact line and in an evaporating thin film of liquid are reported, with applications for techniques such as dip-coating and drop-casting, commonly used for depositing nanoparticles on a surface via convective-capillary assembly. Theoretical analysis suggests that the observed particle motion and aggregation are caused by gradients in surface tension and disjoining pressure in the thin liquid film.

Table of Contents

List of Tables

List of Figures

Chapter 1: Introduction

Since its inception in the 1930's, the transmission electron microscope (TEM), and later the scanning transmission electron microscope (STEM), has provided a powerful means to image features on the nanoscale. These tools provide image resolution in the single nanometer, or even sub nanometer range, far beyond what is possible with traditional light microscopy. In addition to high resolution imaging, the TEM and STEM allow for material characterization due to the unique interactions between the electron beam and the sample. These interactions provide qualitative information such as the relative densities of the constituents of an inhomogeneous sample, as well as precise elemental analysis through characteristic x-ray emission (energy dispersive x-ray spectroscopy) and characteristic electron scattering (electron energy loss spectroscopy). For these reasons, the TEM and STEM have become standard analytical tools in both the physical and the biological sciences.

Until recently, (S)TEM imaging has been limited to solid, frozen, or dried out samples, with very few (S)TEM studies focusing on dynamical processes taking place in liquid media because it has simply not been possible to perform. In the introduction to the oft cited (3000+ citations) article, "Wetting: statics and dynamics," P. G. de Gennes states that our understanding of phenomena at the liquid-solid interface is limited because "solid/liquid interfaces are much harder to probe than their solid/vacuum counterpart; essentially all experiments making use of electron beams become inapplicable when a fluid is present [1]." In other words, since standard electron microscopes require a high vacuum environment for imaging, most liquids will quickly evaporate in this environment and will

not be accessible for observations. Additionally, the TEM and STEM require very thin samples for imaging to avoid excessive scattering or absorption by the sample. Typically, to study a process occurring in liquid media, one must fix (freeze or dry out) samples at various stages of the process and carry out *ex situ* imaging. Although this procedure has resulted in major advances in disciplines ranging from materials science to biology, it suffers from some limitations. Imaging of fixed samples does not capture the dynamics of a process, only static snapshots along the way. Moreover, it is difficult to select the "right" moment to fix the sample, so critical observations may be precluded. Also, the essential sample preparation process may alter the sample in fundamental ways. Liquid-cell *in situ* (S)TEM is a burgeoning technique that makes it possible to view processes taking place in liquid media with a standard TEM or STEM and has the potential of producing new insights in many branches of science. For example, when forming colloidal crystals, it would be highly beneficial to image, in real-time, nanoparticle self and controlled assembly and inter-particle interactions. Such studies are likely to improve our understanding of these processes and enable us to rationally design and fine tune assembly processes to yield desired outcomes. Similarly, direct observations of interactions among macromolecules are likely to enhance our understanding of conformational changes in polymers and macromolecules. For instance, Walker et al. [2] studied motility of protein motors by imaging a large number of static samples, sequenced the images according to pre-conceived rules of motion, and formed an animation of motor locomotion. Their results are compelling, but it would be much more

desirable to directly observe the actual dynamical process in a liquid medium and in real-time.

There is a tool that addresses the aim of imaging liquid samples in an electron microscope: the environmental scanning electron microscope (ESEM). ESEMs make use of a differential pumping configuration to keep the electron beam column isolated from the chamber, which can then be filled with water vapor (a few Torr) to keep a liquid sample (e.g., a droplet) stable for imaging. The interaction of the electron beam with the water vapor produces a cascade effect that amplifies the signal to the gaseous secondary electron detector (GSED) and allows imaging of non-conducting samples and mitigates charge buildup effects [3]. While ESEM is a powerful technique, especially for imaging hydrated solid samples (e.g. imaging surface structure of biological material without the need for sample preparation/modification/fixing), it has drawbacks for imaging processes occurring in liquid media. Significant modification to a standard SEM is required to enable ESEM capabilities and thus it is preferable to buy an ESEM capable microscope from the start. However, the expense of a new microscope may not be feasible for all. While the evaporation issue is alleviated in an ESEM, it is not eliminated and care must be taken with the vapor pressure in the chamber to ensure favorable imaging conditions while also ensuring that the sample does not dry out. Most importantly, only the top layer of the liquid sample is imaged in ESEM, with minimal penetration of the beam into the liquid [4]. Observations are thus limited to the portion of the sample at the liquid-vapor interface (top of the drop), and one is prohibited from viewing the body of the sample or, in the case of a droplet, the part that is in contact with the solid substrate on which it is

supported. These limitations make ESEM inadequate for many studies and there is necessity for another technique to facilitate electron microscopy of liquid samples.

Two key issues, evaporation and sample thickness, must be addressed to enable (S)TEM visualization of liquid suspensions. Electron microscopes operate at high vacuum, and so most liquid samples, particularly aqueous solutions, must be confined in a sealed vessel to prevent evaporation. Water at 25 °C will boil at an approximate pressure of 24 Torr [5], which is much higher than a typical (S)TEM chamber's pressure. Additionally, to provide reasonable resolution and contrast between suspended objects and the suspending medium in all imaging modes (bright field, dark field, and high angle annular dark field), one must use very thin slices of sample (i.e., liquid). The last few years have seen a flare of efforts to develop devices that allow real-time, *in situ* (S)TEM imaging of dynamical, nanoscale processes in fluids [6–18]. In general, liquid-cell (S)TEM devices confine a thin slice of liquid sample in a sealed chamber sandwiched between two electron-transparent membranes, thus preventing evaporation while allowing the electron beam to pass through the sample to produce an image.

To form a liquid slice that is sufficiently thin to minimize electron scattering by the suspending medium, researchers have relied on microfabrication technology to produce a variety of devices based on the common theme of thin membranes separated by a spacer material to form a sealed chamber. The details of each device differ in the choice of membrane material, sealing method, and spacer material. The spacer material dictates the distance between the membranes and the height of the liquid-cell. Williamson et al. [6] and Radisic et al. [7] used 100 nm stoichiometric silicon nitride membranes with a 0.5

– 1 μm silicon oxide layer as the spacer and sealed the device with epoxy. Their device was used in a TEM to study electrochemical nucleation and growth of copper nanoclusters. Liu et al. [8] used 9 nm silicon oxide membranes with a 2 – 5 μm epoxy spacer that also served to seal the device. Their device was used in a TEM to study live E. coli and K. pneumoniae cells and monitor biological processes. de Jonge et al. [9] used 50 nm low stress silicon nitride membranes with 10 μm polystyrene microspheres as the spacer and sealed the device with a special sample holder. Their device was used in a STEM to study fibroblast cells with gold-tagged labels. Zheng et al. [10], [11] used 25 nm low stress silicon nitride membranes with a 200 nm indium layer as the spacer and sealing material. Their device was used in a TEM to study platinum nanocrystal growth and the diffusion of gold nanocrystals. Similarly, Creemer et al. [12] constructed a gas flow cell using a 4 μm thick silicon oxide layer as the spacer and sealed the device with epoxy. Observation windows were formed in 1.2 μm thick low stress silicon nitride membranes by locally thinning the membrane down to 10 nm. Their device was used for TEM imaging of copper nanocrystal growth at elevated temperature and hydrogen atmosphere. Additionally, commercial liquid-cell systems have recently been introduced by companies such as Hummingbird Scientific™ and Protochips™. Typically, these systems use low stress silicon nitride membranes (10's to 100's of nm thick) with a polymer spacer of some kind (beads or photopatterned epoxy) and seal with a custom holder as in the case of de Jonge et al. [9].

In this work, a nanofluidic platform for *in situ* (S)TEM of fluid samples, dubbed the nanoaquarium, is presented with results for studies on systems of nanoparticles as

well as other applications of the device. The nanoaquarium is made by direct bonding of silicon wafers coated with silicon nitride. One of the wafers also contains a thin film of patterned silicon oxide that defines the geometry and height of the chamber and conduits. The thickness of the silicon oxide film, and thus the liquid-cell's height, is controllable and can be prescribed to be tens to hundreds of nanometers. The first version of the nanoaquarium was made with a silicon oxide film that was 100 nm thick, and the imaging window was made of two 50 nm thick silicon nitride membranes. For the second version of the nanoaquarium, devices were produced with an oxide film that was up to 300 nm thick. The device fits into a custom-made holder and can sustain the high vacuum environment of the electron microscope for many hours without any noticeable loss of liquid. Some of the nanoaquarium's highlights include:

- An exceptionally thin sample cross-section, a distinction that translates to improved contrast and resolution. The technique could be used to produce channels and chambers as thin as a few tens of nanometers. The chamber spacing on each device is highly controllable thanks to the wafer bonding process. There is no risk of debris incorporation when assembling the device, which could modify the height of the chamber and is a concern in other individually assembled devices.
- Wafer scale processing that enables high yield mass production, as opposed to production on a device-by-device basis.
- Robust hermetic sealing that provides leak-free operation without the use of glues, epoxies, or polymer spacers. These materials are a potential source of

contamination and/or device failure. When the nanoaquarium is filled with a solution, the only materials in contact with the solution are silicon, silicon nitride, and silicon oxide (as well as titanium and platinum or gold when electrodes are present). At the inlet and outlet, the solution is also in contact with O-rings; however, the inlet and outlet are far from the imaging window and robust, chemically inert material can be selected for the O-rings such that there is no threat of contamination. This makes the nanoaquarium uniquely suited to handle harsh chemistries such as strong solvents, acids, or bases.

- Compatibility with lab-on-chip technology such as sample storage and manipulation (e.g. mixing, pumping).
- On-chip integrated electrodes for sensing and actuation thanks to use of a dielectric material as the spacer.
- The nanoaquarium can be used in either a static mode without through flow or a continuous flow mode. In static mode, the nanoaquarium is self-contained and does not require fluidic feed-throughs on the sample holder. This simplifies construction of the sample holder and minimizes the volume of solution consumed in an experiment.
- It is envisioned that the nanoaquarium will be used as a disposable device to avoid cross-contamination; however, devices can be reused when desired. The nanoaquarium can be removed from the holder, drained, and refilled with a new/fresh solution as needed for the experiment.

Chapter 2: Fabrication of the Nanoaquarium

Portions of what appears in this chapter can be found in the Journal of Microelectromechanical Systems [13], Copyright © 2010, IEEE.

The nanoaquarium consists of a hermetically sealed, liquid-filled chamber sandwiched between two freestanding silicon nitride membranes. The fabrication technique described here allows one to construct exceptionally thin chambers. Embedded electrodes are integrated into the device for sensing and actuation. Figure 2-1 schematically depicts the cross-section of the device, and Figure 2-2 schematically depicts the fabrication steps. Two versions of the nanoaquarium were fabricated; version 1 was produced during the summer of 2009 and version 2 was produced during the fall of 2010. After working with version 1 of the nanoaquarium, minor changes were made to the design and process flow in order to make improvements in version 2. In the following sections of this chapter, version 1 and version 2 of the nanoaquarium are distinguished from each other where appropriate.

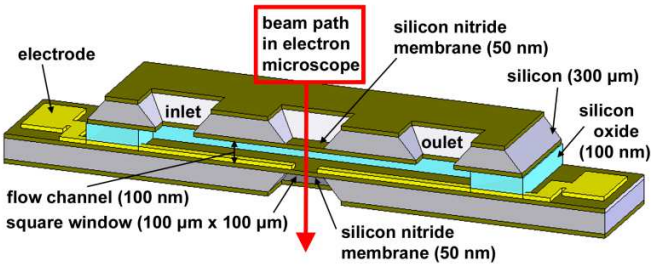

Figure 2-1: A schematic depiction of the nanoaquarium's cross section. Not drawn to scale.

Section 2.1: Starting Substrate

Superior to prime grade, 300 µm thick, 100 mm diameter, double-side polished <100> Si wafers were purchased from Semiconductor Processing Company (Boston,

MA). From a batch of 50 wafers, 20 wafers were characterized. The wafers ranged in thickness from 304.2 to 306.8 µm. Individual wafer specs included a total thickness variation (TTV) ranging from 0.2 to 1.6 µm and bow ranging from -4.7 to 2.5 µm. When direct wafer bonding is to be performed, the flatness and smoothness of the starting substrate are of paramount importance. Unlike adhesive or thermocompression bonding, direct bonding does not involve an intermediate layer that can reflow to compensate for warped or uneven surfaces. The physical specifications for prime grade wafers are generally considered sufficient for direct wafer bonding [19].

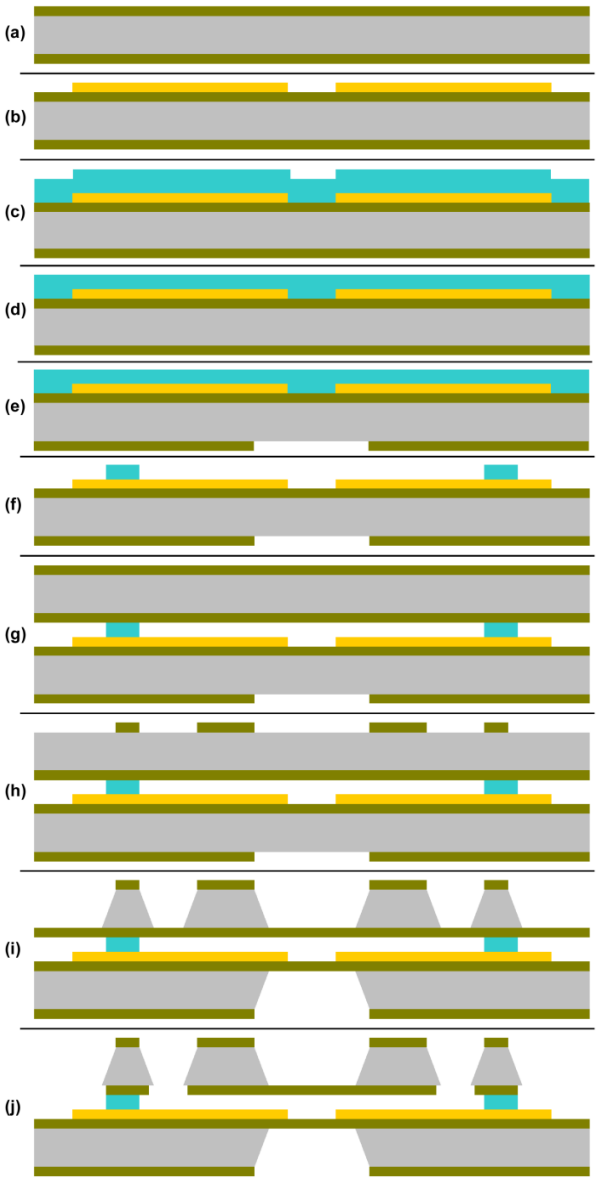

Figure 2-2: Depiction of the various fabrication steps. Color coded as follows: gray – silicon, green – silicon nitride, yellow – electrode stack, blue – silicon oxide. (a) 50 nm silicon nitride deposited by LPCVD. (b) 30 nm Ti / Au or Pt / Ti electrode stack deposited and patterned by evaporation and lift-off. (c) 150 nm – 450 nm silicon oxide deposited by PECVD. (d) Oxide planarization in a CMP. (e) Backside nitride patterned in RIE. (f) Frontside oxide patterned with BOE. (g) Plasma activated wafer bonding to a blank nitride-coated wafer. (h) Backside nitride on top wafer patterned in RIE. (i) Windows and vias etched with KOH. (j) Inlet, outlet, and electrodes are exposed.

Section 2.2: Depositing Films

50 nm of stoichiometric silicon nitride with a residual tensile stress of 800 MPa was deposited on both sides of all wafers by low pressure chemical vapor deposition (LPCVD) at a facility brokered by the MEMS and Nanotechnology Exchange (Figure 2-2(a)). Electrodes were patterned on some of the wafers' frontsides by lift-off technique (Figure 2-2(b)). The electrodes consisted of a Ti / Au / Ti stack (4 nm / 22 nm / 4 nm) in version 1 and a Ti / Pt / Ti stack (4 nm / 22 nm / 4 nm) in version 2, deposited by e-beam evaporation. Ti was used above and below as an adhesion layer to the substrate as well as to the subsequent film deposited on top of the electrodes. Silicon oxide was deposited by plasma enhanced chemical vapor deposition (PECVD) on the wafers' frontsides (Figure 2-2(c)). Silicon oxide films with a thickness of 100 nm – 450 nm were deposited on wafers with electrodes and wafers without electrodes (simplified devices without electrodes were also produced). A greater thickness of oxide was applied to wafers with electrodes to allow for subsequent planarization.

The Ti / Au / Ti stack in version 1 was replaced with a Ti / Pt / Ti stack in version 2 of the nanoaquarium because the electrodes in version 1 presented micron-size patches of missing metal all over the electrodes (see Figure 2-3) and did not function properly in many devices. We suspect that the gold layer and the surrounding layer of silicon oxide (which, as a result of the PECVD deposition technique, was not pure stoichiometric SiO_2) interdiffused and reacted during one of the high temperature annealing steps that were needed for wafer bonding. The change of material from gold to platinum appeared to fix

the problem. The Ti / Pt / Ti electrode stack “looked pristine” and functioned properly (as illustrated in the electrochemical experiment discussed in Section 2.11.2.

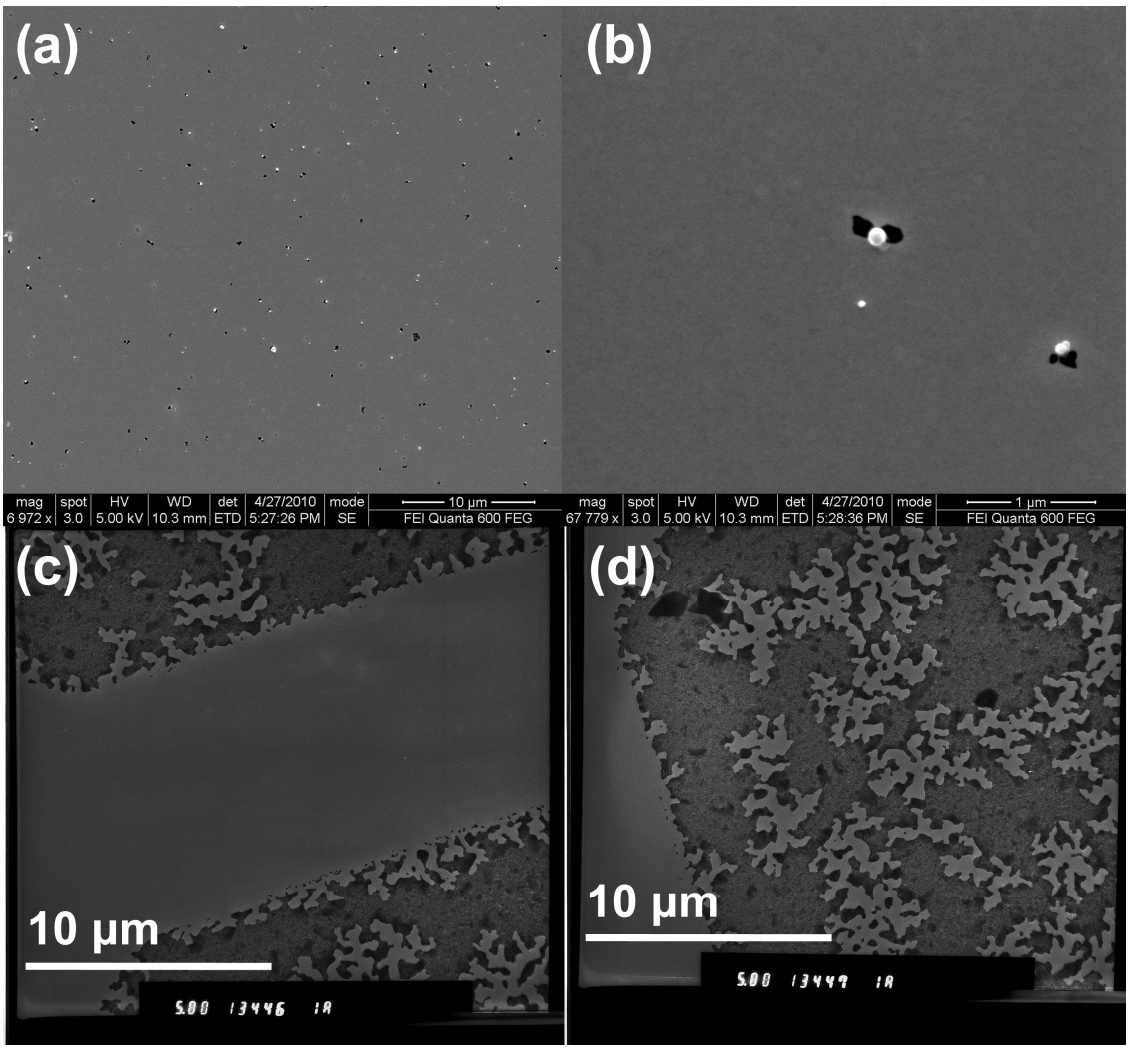

Figure 2-3: Images of problem electrodes in completed version 1 devices. (a) and (b) Scanning electron microscope images of electrodes, showing the presence of patches throughout the electrode surface. Many patches had an associated bead of material, as pictured in (b). (c) and (d) TEM images of electrodes with an especially bad patchy electrode problem.

Section 2.3: Film Densification

Following oxide deposition, wafers were annealed in a tube furnace with nitrogen ambient to densify the oxide films. In version 1, wafers with electrodes were annealed for 4 hours at 350°C, and wafers without electrodes were annealed for 4 hours at 400°C, followed by an additional 4 hours at 350°C. In version 2, all wafers were annealed for 4 hours at 350°C. Preliminary wafer bonding tests demonstrated that insufficient film densification can lead to film outgassing during the bond anneal step. Typically, bond strength is the metric that one seeks to maximize when bonding wafers as part of a permanent structure. As bond strength improves, the ability of trapped gas to diffuse along the bond interface diminishes [20]. Without sufficient film densification, incorporated gases and reaction gases produced during the bond annealing step are unable to escape and lead to incomplete bonding.

In the preliminary process development tests, bonding was performed between prime grade 500 μm thick, 100 mm diameter, single side polished <100> Si wafers. Figure 2-4(a) is an infrared (IR) image of a room temperature bonded wafer pair. Wafer 1 was coated with 50 nm of LPCVD stoichiometric silicon nitride followed by 75 nm of PECVD silicon oxide that had been densified at 350°C for 1 hour. Wafer 2 was coated with 50 nm of LPCVD stoichiometric silicon nitride. According to the image, good contact formed along nearly the entire interface of the wafers. After room temperature bonding, the wafers were annealed for 13 hours at 300°C. IR imaging subsequent to the annealing process (Figure 2-4(b)) revealed the presence of multiple voids due to film outgassing. Apparently, the desorbed gas formed high pressure bubbles that deformed the

wafers locally. The resulting interference fringes are visible in the IR image. Similar observations have been reported by others [20–22]. The area outside the bubbles formed a high strength bond that prevented the wafers from separating and the gas in the bubbles from escaping. Inspection of the same wafer pair nine months later (Figure 2-4(c)) revealed that some of the smaller bubbles disappeared and some of the larger bubbles shrank, as indicated by the fringe pattern. Comparison between Figure 2-4(b) and Figure 2-4(c) indicates that the voids are dynamic and some of the gas can diffuse out of the voids, either through the interface, or through the film and substrate [23]. The diffusion process, however, is extremely slow.

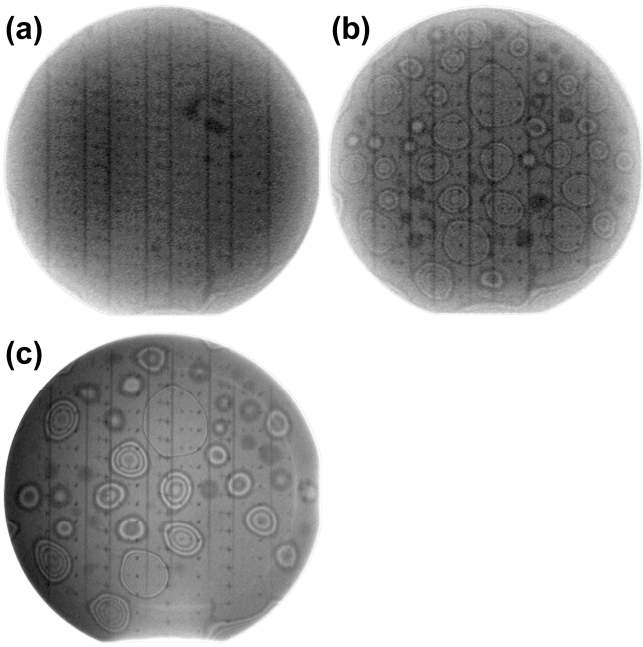

Figure 2-4: IR images of bonded wafer pair. Bond was between 75 nm PECVD silicon oxide film on wafer 1, and 50 nm LPCVD stoichiometric silicon nitride film on wafer 2. Dark vertical lines and periodic squares are from etched nitride on the backside of wafer 1 and are not part of the bond interface. (a) Room temperature bonding results in a nearly perfect bond. Only a few unbonded regions are present around the perimeter. (b) After annealing for 13 hours at 300°C, many voids are visible due to film outgassing. (c) Nine months later, voids are still present; although they evolved and shrank slightly in volume (as evidenced by the decreased number of interference fringes), presumably due to gas diffusion

The degassing issue seems to be significant for silicon oxide deposited by techniques such as PECVD and LPCVD, but not for thermally grown oxide [24]. It has been demonstrated that patterned films can produce void free bonds, even without

densification, because grooves provide escape paths for gases produced during the bond anneal step [25–28]. This is a useful unintended benefit of working with wafers that have features patterned on them. Film densification, however, should not be ignored.

Section 2.4: Polishing

The silicon oxide film that was deposited on the wafers with electrodes provided a conformal coating that retained the stepped topography of the embedded electrode pattern (Figure 2-2(c)). The oxide film on these wafers was planarized using a Strasbaugh 6EC Chemical Mechanical Polisher (CMP) (Figure 2-2(d)). It was discovered during version 2 fabrication that polishing of the wafers without electrodes should be performed, even though there is no embedded topography. Polishing proved to be the second most challenging step of the fabrication process, next to wafer bonding.

2.4.1 Polishing of Version 1 Devices

Wafers with embedded electrodes were temporarily glued to a 500 μm thick handle wafer using SPR220-7.0 photoresist to ensure that the CMP head had a sufficiently thick specimen to grip during polishing. Wafers were polished until the steps were smoothed out and the oxide thickness was approximately 70 nm above the electrodes and 100 nm elsewhere. After polishing, the handle wafer was released by soaking the sample in resist stripper (Shipley Microposit Remover 1165) for 24 hours.

2.4.2 Polishing of Version 2 Devices

In addition to polishing the wafers with embedded electrodes, the silicon oxide on the non-electrode devices was also polished. This was necessary due to a surface

roughness issue, explained further in Section 2.5. The use of photoresist as temporary glue between device wafers and handle wafers proved problematic during fabrication of version 2 devices. In most cases, the surface of the sample was extremely uneven after polishing (see Figure 2-5). This was likely due to uneven photoresist that caused some parts of the wafer to be polished more than others.

The level of non-uniformity depicted in Figure 2-5 was unacceptable because large regions of the wafers remained essentially unpolished, and thus the electrode topology persisted. Device wafers were released from the handle wafers by soaking them in resist stripper (Shipley Microposit Remover 1165) for one to three days. On several wafers that possessed significant gashes/burn marks from uneven CMP, additional oxide was deposited by PECVD so that the sample could be polished further in order to remove the sharp steps of the embedded electrode topology. The retaining ring of the CMP head was carefully adjusted and multiple tests were performed with dummy wafers to make

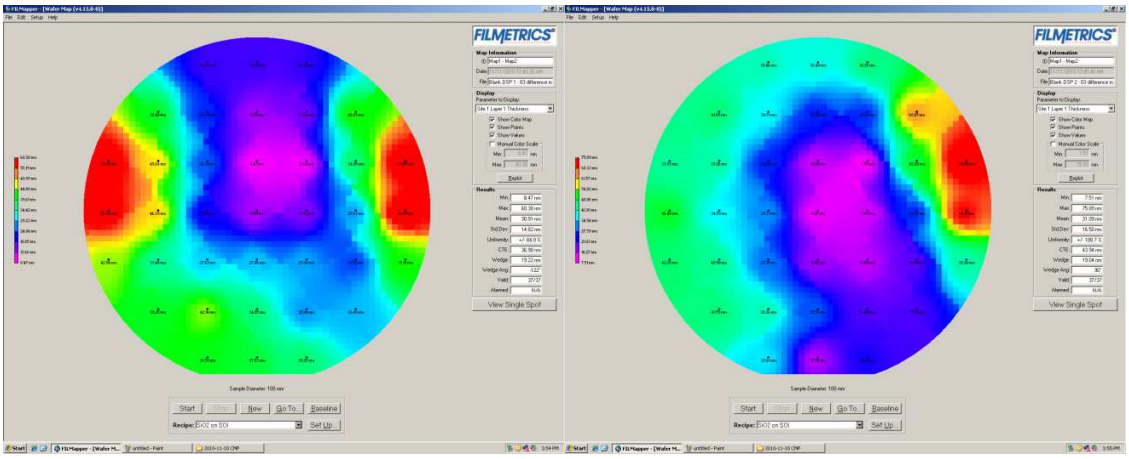

Figure 2-5: Film thickness measurements that show the amount of material removed from two wafers that were polished while glued to a handle wafer with photoresist. Uniformity is terrible; the first sample has a minimum removal of 8.47 nm and a maximum removal of 60.38 nm, and the second sample has a minimum removal of 7.51 nm and a maximum removal of 75.09 nm.

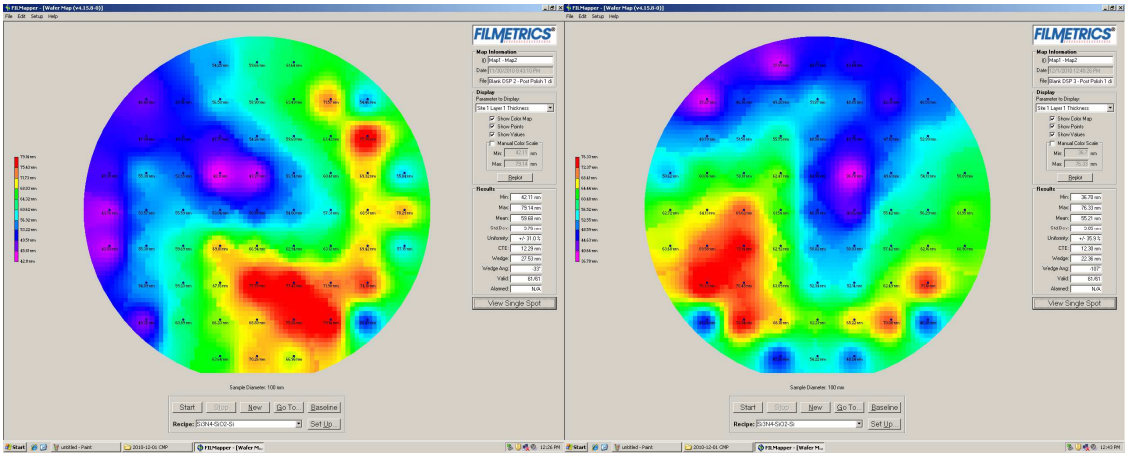

Figure 2-6: Film thickness measurements that show the amount of material removed from two wafers that were polished without use of a handle wafer. Uniformity is better than that of Figure 2-5; the first sample has a minimum removal of 42.11 nm and a maximum removal of 79.14 nm, and the second sample has a minimum removal of 36.70 nm and a maximum removal of 76.33 nm.

sure that the wafers would remain gripped by the CMP head. Device wafers were then polished in the CMP without use of a handle wafer. Representative reflectometer scans that show the amount of material removed during a CMP run are depicted in Figure 2-6. Although some wafers were lost during polishing (6 out of 9 survived), it was necessary to polish the wafers in this manner in order to ensure the most uniform planarization.

Polishing uniformity was improved by forgoing the handle wafer. Still, in many cases the planarization that resulted from several CMP runs was insufficient, but there was not enough oxide material left to allow for further polishing. In such cases, additional silicon oxide was deposited by PECVD and the wafer was polished again. Sometimes several iterations of deposition and polishing were necessary to achieve satisfactory planarization. The material removal patterns from the two different wafers featured in Figure 2-6 actually look quite similar, simply rotated. This implies that the nonuniformities were related to the CMP head and the orientation it happened to be in

when it picked up the wafer for polishing. For this reason, the polishing process on a single wafer was often broken up into several runs. For example, rather than polishing a wafer for 2 minutes continuously, the process was broken up into four 30 second polishing runs. Doing so introduced variability into the orientation of the wafer relative to the CMP head so that the pattern of nonuniformity would be rotated by some random angle during each polishing run.

Section 2.5: Surface Roughness

Surface roughness measurements were taken with an atomic force microscope (Digital Instruments Dimension 3100) to ensure that wafer surfaces were sufficiently smooth for direct bonding. RMS surface roughness was measured in tapping mode by scanning 2 μm x 2 μm squares at several locations on each wafer. Measurements were taken throughout the fabrication process of version 1, the results of which are presented in Table I and representative scans are pictured in Figure 2-7. The surface roughness should be as low as possible for direct wafer bonding. Comparison of sample 3 and sample 4 (Table I) demonstrates that the surface roughness of a sample can be reduced greatly by polishing with a

TABLE I

SURFACE ROUGHNESS

	Sample	RMS Roughness
1	LPCVD nitride coated wafer - as deposited	0.30 nm
2	PECVD oxide coated wafer (without electrodes) - as deposited	0.79 nm
3	PECVD oxide coated wafer (with electrodes) - as deposited	1.24 nm
4	PECVD oxide coated wafer (with electrodes) - post CMP	0.47 nm

Surface roughness measurements at various steps of the fabrication process as measured by AFM in tapping mode (2 μm x 2 μm scan area with 4 – 6 scan locations per wafer). Samples 1, 2, and 4 were device wafers used for bonding. The oxide on samples 2 and 3 was deposited using different tools.

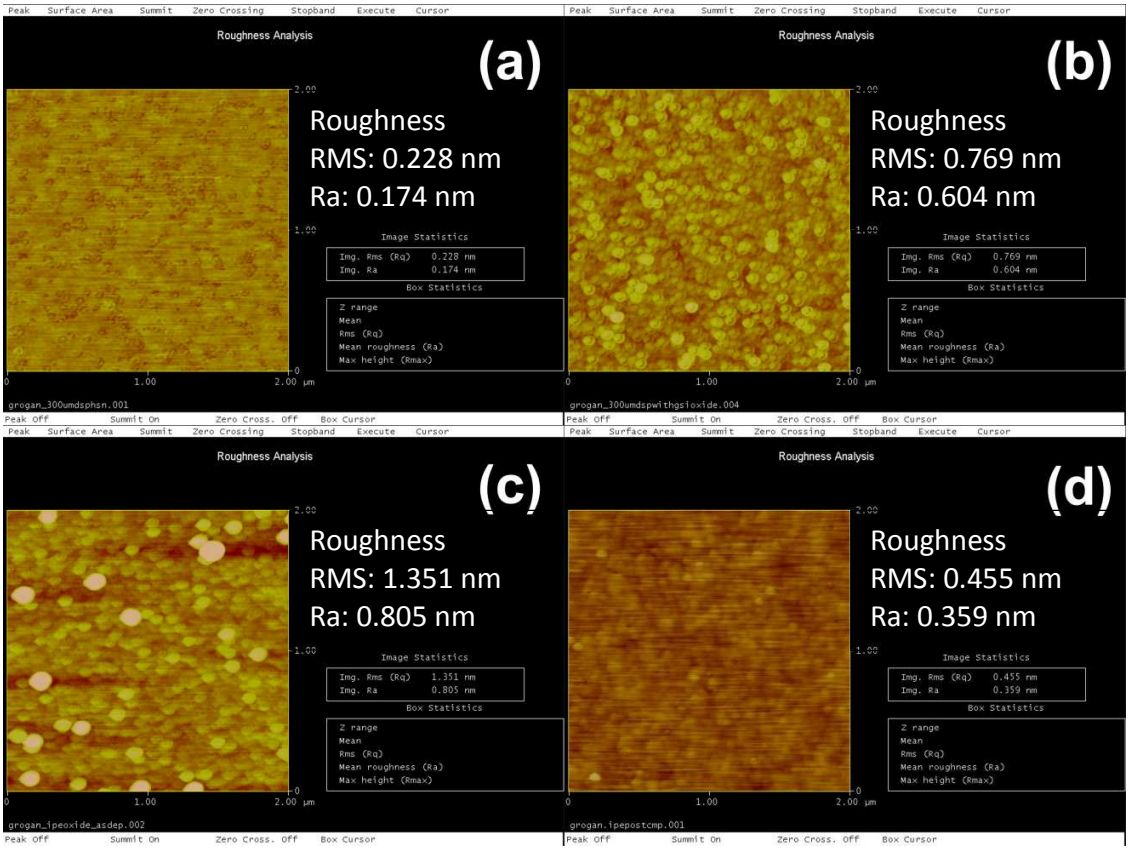

Figure 2-7: Examples of the AFM scans presented in Table I. (a) LPCVD nitride coated wafer - as deposited. (b) PECVD oxide coated wafer (without electrodes) - as deposited. (c) PECVD oxide coated wafer (with electrodes) - as deposited. (d) PECVD oxide coated wafer (with electrodes) - post CMP. The oxide that was deposited on samples (b) and (c) was done using different tools, which is likely the reason for the difference in as deposited roughness.

CMP. Using the appropriate polishing pad and slurry materials, the RMS roughness can ultimately be brought down to as low as 0.1 nm [29]. Realistically, 1 nm or lower is a good target for RMS roughness [19], though prior wafer bonding tests demonstrated successful bonding of wafers with RMS roughness as large as 2 nm.

During version 1 fabrication, oxide that was deposited on blank wafers for the production of nanoaquarium devices without electrodes did not need to be polished in the CMP (see sample 2 in Table I). However, while fabricating version 2 devices, almost all

of the oxide that was deposited on wafers with and without electrodes was found to contain scattered narrow spikes with height up to 100 nm. The spikes represented some form of contamination, and while the exact source is unclear, there are two possible explanations. One possibility is simply a dirty PECVD chamber with excess material on the chamber walls that flaked off and deposited on the wafers. The other possibility is homogenous nucleation during the PECVD process. The chemical reaction that occurs during PECVD does not occur exclusively on the wafer surface, as is the case in a process like epitaxy. Under the right (or more accurately, “wrong”) conditions, source gases react in the bulk of the plasma field and nucleate nanoscale product throughout the chamber; this is called homogeneous nucleation. The material produced during homogenous nucleation remains suspended in the plasma field until the end of the process and then lands on the sample when the plasma shuts off. In order to make use of the samples that had already received PECVD oxide and to avoid troubleshooting the PECVD tool (which would likely be complicated), all wafers, with and without electrodes, were polished with the CMP. As illustrated in Table I, CMP polishing produces surfaces superior to even the best as deposited PECVD oxide, so in general, polishing all samples should yield better outcomes for wafer bonding. Representative surface profilometer scans of wafers at various stages of processing during the fabrication of version 2 devices are presented in Figure 2-8 to Figure 2-11.

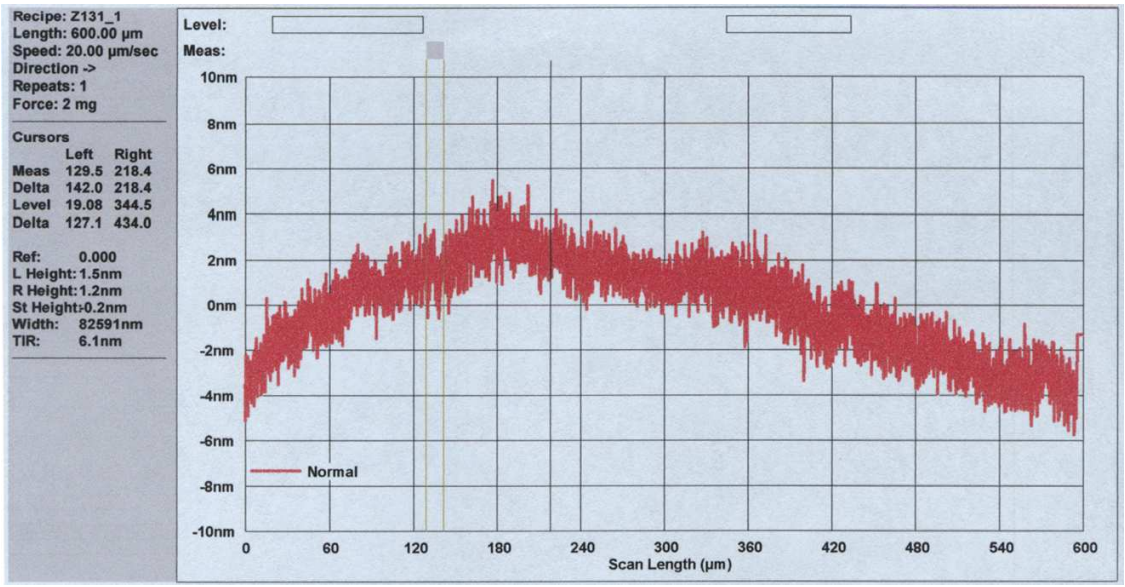

Figure 2-8: Surface profilometer scan of a bare LPCVD nitride coated wafer that did not yet received any further processing.

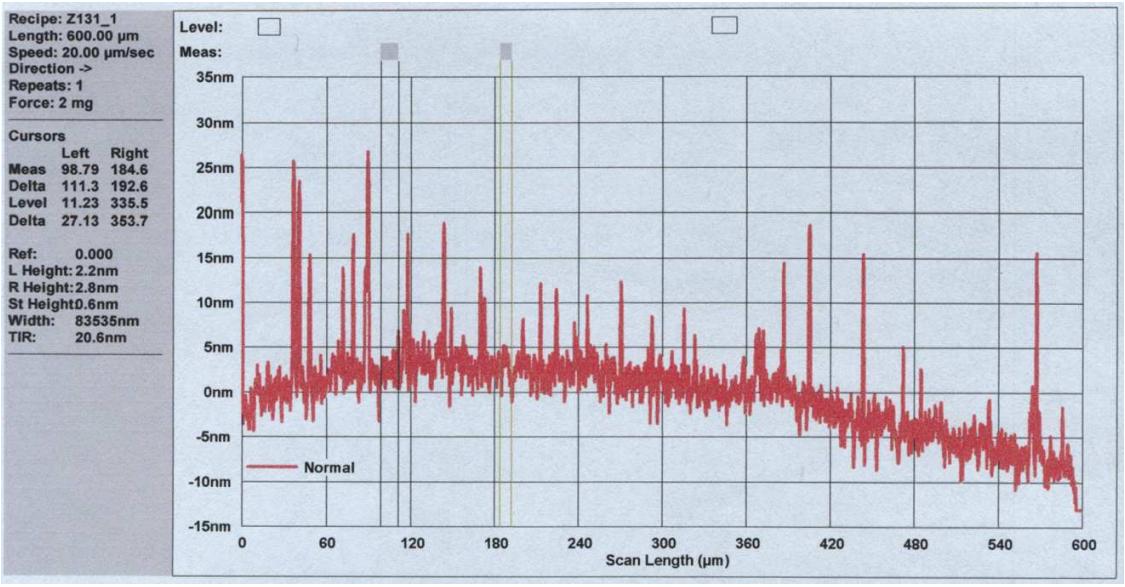

Figure 2-9: Surface profilometer scan of a wafer (without electrodes) that was coated with approximately 160 nm of PECVD silicon oxide. Spikes are present throughout the scan. The issue of spikes was present, irrespective of whether the wafer contained electrodes, thus ruling out contamination from the wafer itself as the cause of the problem.

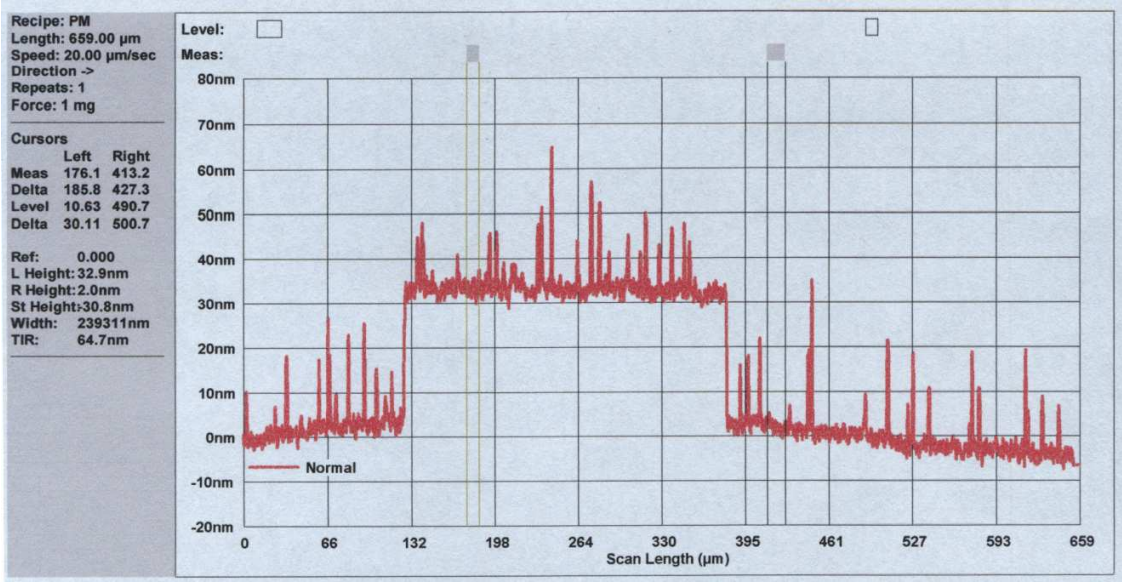

Figure 2-10: Surface profilometer scan of a wafer with patterned electrodes that was coated with approximately 160 nm of PECVD silicon oxide. Spikes are present throughout the scan.

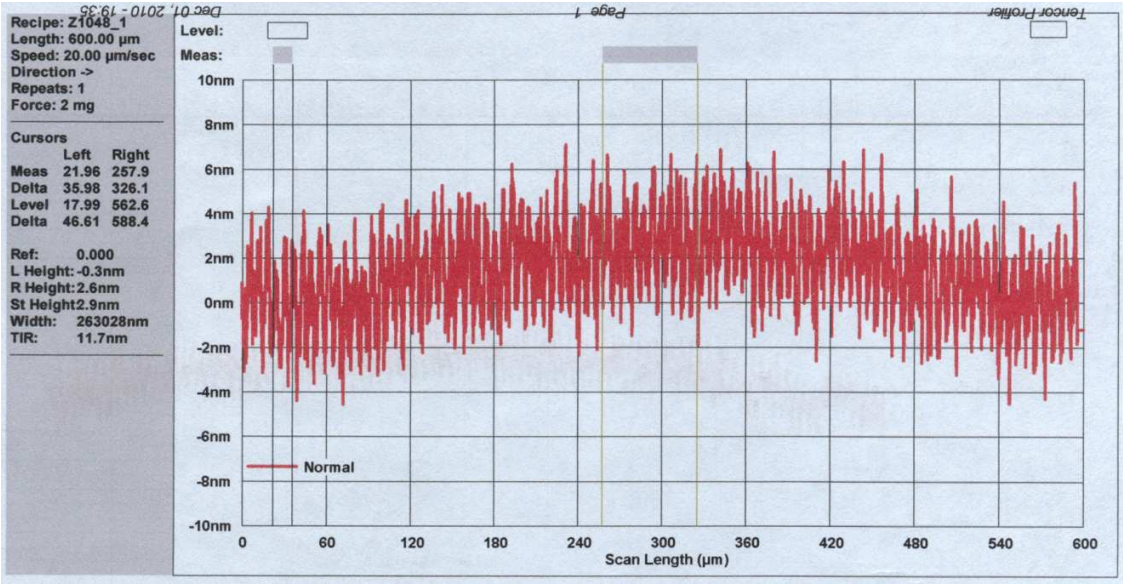

Figure 2-11: Surface profilometer scan of a wafer with patterned electrodes after polishing in a CMP. This scan was performed over an area with an embedded electrode, similar to the scan in Figure 2-10. Several iterations and deposition and polishing, as described in Section 2.4, were performed to achieve an acceptably smooth surface.

Section 2.6: Etching Oxide & Nitride

Wafer backsides were patterned and etched in a reactive ion etcher (RIE) to define the membrane window pattern in the silicon nitride film (Figure 2-2(e)). Care was taken to ensure that the pattern was aligned with the crystallographic structure of the wafer. This was accomplished by including a feature at the bottom of the photomask that was used to align the major flat of the wafer to the orientation of the mask. Wafer frontsides were patterned and etched with 5:1 buffered oxide etch (BOE) to define the conduit pattern in the silicon oxide film (Figure 2-2(f)). The pattern for the silicon oxide spacer layer was modified in version 2 to include four 8 μm pillars in the window region to anchor the top and bottom membranes to each other in order to mitigate outward bowing of the membranes when the device is clamped in its fixture/holder (see Section 2.10) or when high pressure develops in the cell as in the case of gas formation. Backside alignment was performed to align the conduit pattern on the frontside with the window pattern on the backside. When the wafers contained electrodes, the BOE also etched the top layer of Ti

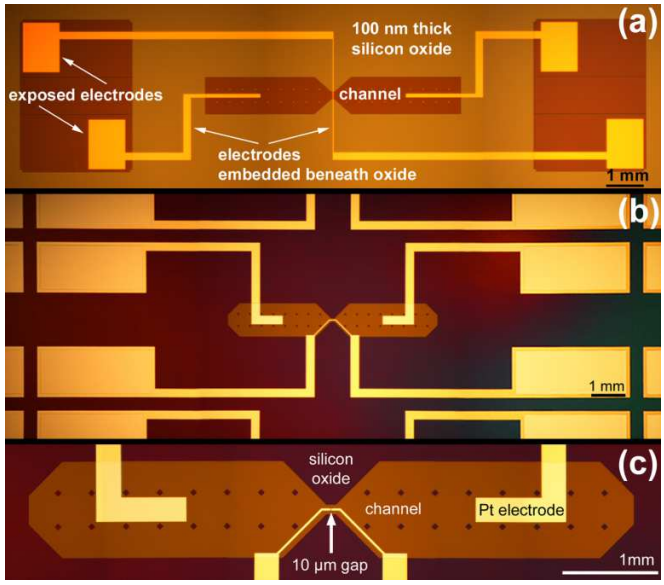

Figure 2-12: Top view of a single device on the bottom wafer prior to capping with the top wafer. (a) Version 1. (b) and (c) Version 2.

in the electrode stack, thus exposing the gold/platinum layer in the channel and at the contact pads. Figure 2-12 shows partially fabricated devices at this point in the process.

Section 2.7: Surface Cleaning, Plasma Activation, and Direct Bonding

Direct bonding of silicon wafers is an attractive method for sealing cavities and forming channels because hermetic seals are possible with low temperature, low force, and no electric field [19], [30–33]. When the wafers satisfy appropriate bow/warp, total thickness variation (TTV), surface roughness, and cleanliness criteria, spontaneous bonding at room temperature is possible. Following this initial weak bond, attributed to van der Waals forces and hydrogen bonds, wafer pairs are typically annealed at elevated temperature to increase the bond strength. For wafers whose surfaces were activated by wet chemistries alone, anneal temperatures as high as 1000 °C are necessary to maximize bond strength. However, when wafer surfaces are plasma treated prior to bonding, the anneal temperature can be lowered significantly to 200 – 300 °C. This is especially important when materials such as metal electrodes are present on the wafers, prohibiting the use of extreme temperatures. Wafer cleaning and plasma treatment are therefore critical steps in preparing wafers for bonding. In this section, the procedures for optimizing the bonding process and the final recipe are described.

First, the wafers were thoroughly cleaned to remove any contaminants and activate the surfaces for bonding. For direct bonding involving a silicon oxide surface, the cleaning process should leave the surfaces hydrophilic. Piranha (sulfuric acid and hydrogen peroxide) and RCA 1 (ammonium hydroxide, hydrogen peroxide, and water)

cleaning solutions were examined, which are commonly used to remove organic contaminants and leave surfaces hydrophilic. Both solutions bubble aggressively due to the presence of hydrogen peroxide, an effect that dislodges and removes stubborn inorganic particle contaminants. Miyashita et al. studied cleaning effectiveness and surface roughening of Si wafers and demonstrated that piranha causes no significant surface roughening, but the traditional RCA 1 solution ($NH_4OH:H_2O_2:H_2O$ = 1:1:5) causes slight roughening [34]. Thus, a modified RCA 1 solution (MRCA 1) was used with a reduced concentration of ammonium hydroxide ($NH_4OH:H_2O_2:H_2O$ = 0.25:1:5) [35]. Min et al. demonstrated that in glass-to-silicon direct wafer bonding, combinations of cleaning solutions improved bond quality [36]. Indeed, our experience indicated that cleaning both wafers with piranha followed by MRCA 1 yielded the best results. Subsequent plasma activation and bonding was performed immediately after the wet chemistry treatments (within several minutes).

It has been demonstrated extensively that plasma activation improves bond strength at low annealing temperature. The recommendations for the plasma process, however, such as process gas, duration, pressure, and power vary greatly in the literature and are material and tool-specific. Hence, the appropriate conditions for this circumstance were investigated.

Argon, nitrogen, and oxygen have all been reported as effective process gases for plasma activation. Doll et al. examined the effect of process gas and anneal temperature on bond strength for various material combinations [25]. For Si–SiO_2 bonds, anneal temperature was shown to have minimal effect on surface energy when wafers were

treated with oxygen plasma. The surface energy was generally high for all temperatures (~ 2 J/m^2) with a slight peak around 250 °C. Anneal temperature was shown, however, to be directly proportional to surface energy when wafers were treated with argon plasma. Oxygen plasma yielded stronger bonds below 250 °C, but argon plasma was more effective above 250 °C. For Si–Si_3N_4 and Si_3N_4–Si_3N_4 bonds, surface energy was directly proportional to the anneal temperature for oxygen and argon plasma treatments alike. Thus, we selected oxygen as the plasma process gas due to its effectiveness at low temperature (< 300 °C) bonding of SiO_2. Moriceau et al. demonstrated that SiO_2 surfaces treated with oxygen plasma at 50 mTorr experienced a decrease in surface roughness when the treatment time exceeded 10 seconds [37]. Process pressures of tens of mTorr are also recommended in many other reports [20], [25], [38], [39]. Additionally, Moriceau et al. showed that for Si–SiO_2 bonds, surface energy as a function of plasma treatment time has a peak around 30 seconds [37]. Thus, wafers were plasma treated for 30 seconds at 60 mTorr.

Plasma activation was performed with an Oxford PlasmaLab 80+ RIE system, which is part of a multi-user facility and is regularly exposed to various photoresist and etch byproducts that could adversely affect bond quality [25]. To minimize chamber-induced contamination, the chamber was cleaned before wafer treatment with oxygen plasma for one hour at 60 mTorr with a gas flow rate of 50 sccm and platen power of 150 W.

Plasma activation of wafer surfaces with platen power values in the range of 15–100 W have been frequently reported [20], [25], [37], [38]. To determine the optimal

value of our tool's platen power, bond tests were performed using prime grade, 500 μm thick, 100 mm diameter, single side polished <100> Si wafers coated with 60 nm of PECVD silicon oxide. Pairs of wafers were treated with oxygen plasma for 30 seconds at 60 mTorr, a gas flow rate of 50 sccm, and platen powers of 15, 75, and 100 W. Wafers were then rinsed in deionized (DI) water for 60 seconds, spun dry for 2 minutes, and mated by hand. The post-plasma DI water rinse washed away particles from the wafer surface that might have accumulated from the RIE chamber and provided water molecules that adsorb to the wafer surface to assist in forming hydrogen bonds between the wafers [25], [38]. Previous wafer bond tests on troublesome wafers with 25 μm bow and 35 μm warp demonstrated that a 4% NH_4OH wash in place of the DI water wash can help establish a stronger room temperature bond. Following the DI water rinse, the samples were annealed for 12 hours at 250°C in nitrogen ambient.

The bonded area for each pair of wafers was imaged with an IR camera, and the bond strength was inspected with the Maszara crack-opening method in which a razorblade is inserted between the bonded wafers and the resulting debonded area is measured [40]. Although this method is inaccurate for quantifying the surface energy of bonded wafers [41–43], consistent application of the technique to sets of similar wafers provides an easy qualitative method to assess bond quality without having to dice samples. Examination with a razor blade revealed that all samples partially debonded and then fractured, but the sample treated at 15 W debonded the least prior to fracture. During fabrication of version 2 devices, 15 W proved insufficient to activate the wafers surfaces and 30 W was used instead.

Additional bond tests were carried out with the silicon nitride coated custom wafers to confirm that the bonding process was, indeed, optimized. Two wafers were coated with 100 nm PECVD silicon oxide and two wafers were left bare to test SiO_2–Si_3N_4 bonding. The bonding process is detailed in Table II. Two different post-plasma washes were tested (DI water and 4% NH_4OH in DI water), but there did not appear to be any difference in the bond quality. In both cases, the razor blade could hardly be inserted anywhere between the pair of bonded wafers. When the blade was forced, one of the wafers simply chipped off, tearing out chunks of material from the opposite wafer with it. This result indicated that the bond was as strong as the underlying substrate.

The bonding process detailed in Table II was used to bond device wafers (with and without electrodes) to their blank nitride-coated partners (Figure 2-2(g)). Blank nitride-coated wafers were used as the bonding counterparts to avoid potential complications of wafer-to-wafer pattern alignment. The major and minor flats of the feature-containing device wafer and the feature-free blank wafer were aligned by hand. This ensured similar crystallographic orientations of the wafers. Patterning of the blank wafer took

TABLE II

PLASMA ACTIVATED WAFER BONDING RECIPE

Step	Process
1	Piranha clean • H_2SO_4:H_2O_2 = 1:3 for 10 min
2	MRCA 1 clean • NH_4OH:H_2O_2:H_2O = 0.25:1:5 for 10 min at 80°C
3	Plasma activate • O_2 plasma for 30 seconds at 60 mTorr with a gas flow of 50 sccm and platen power of 15 W – 30 W
4	Rinse & Dry • Dunk in DI water or 4% NH_4OH in DI water for 4 min • Dry in Verteq spin rinse dryer or Hamatech-Steag wafer processor
5	Version 1: Mate wafers by hand • Push center together first • Manually spread bond interface by squeezing wafers together while inspecting with IR camera Version 2: Bond wafers in Suss SB8e wafer bonder • 1E-3 – 1E-4 mbar chamber pressure • 1100 – 2200 N force for 5 – 10 min
6	Anneal • 250°C for 2.5 hours (ramp up and down)

place after bonding (as described in the following section).

Due to material restrictions in the RIE tool, the wafers with gold electrodes were not plasma treated, but did receive the wet chemical cleanings. While plasma treatment of both wafers is ideal, the process still works when only one wafer is treated; however, a decrease in surface energy of 15 – 50 % is expected [37]. The inability to put gold in the plasma tool was part of the motivation for changing the electrode material from gold to platinum in version 2, for which plasma activation was performed on all wafers.

In the literature there is evidence of a beneficial aging effect, where bond strength improves over the course of days and weeks for wafers stored in room conditions [23], [38], [44]. Thus, bonded wafers were allowed to rest for 12+ days before further processing.

Section 2.8: Etching nitride, KOH etching, and final steps

The backsides of the blank bonded top wafers were patterned and etched in an RIE to define the complementary membrane window pattern as well as inlets/outlets to the channel (Figure 2-2(h)). Additionally, narrow lines were defined that would self-terminate in the KOH etch to allow easy separation of the individual chips. Backside alignment with an EV620 Contact Aligner or Suss MA6 Contact Aligner was used to align the mask for patterning the top wafer's backside to the existing pattern on the bottom wafer's backside. Bonded wafer stacks were etched for several hours in 30% KOH at 80 °C until the inner nitride membrane was reached (Figure 2-2(i)). During earlier process development tests, membranes were etched on individual wafers and their

shape was inspected after the etching process. The released membranes did not exhibit any apparent deformations.

Windows measured 100 μm × 100 μm and inlets/outlets measured 300 μm × 300 μm at the bottom of the tapered KOH etch. The alignment precision of the top and bottom windows was ultimately set by the precision of the contact aligner, which had a stated front-to-back alignment accuracy of 1 μm. Inspection of the samples revealed that the membrane window edges were generally aligned to better than 3 μm.

Individual chips were separated without the use of a dicing saw thanks to the self-terminating lines that served as scribe marks for manual cleaving. The scribe marks were laid out in a grid pattern that traced the perimeter of each individual chip, but did not intersect at the corners (convex corners result in rounded features in KOH etching). After KOH etching, the wafer stacks were mounted on removable dicing tape to keep debris off of the membrane windows. Chips were then separated by manually snapping the wafer stack along the scribe marks. This technique is gentler than a dicing saw and minimized the risk of damage to the membrane windows. A completed device is shown in Figure 2-13.

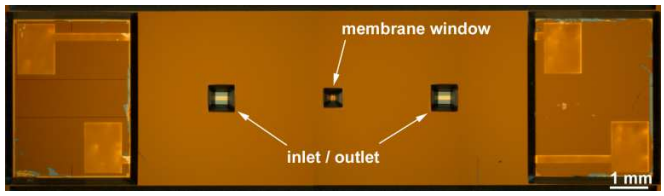

Figure 2-13: Top view of a completed single version 1 device (18 mm x 5 mm x 0.6 mm).

Completed devices contained freely suspended silicon nitride membranes at the inlets/outlets in addition to the imaging windows. To gain access to the channel, the nitride membranes at the inlets/outlets were popped with tweezers (Figure 2-2(j)).

Alternatively, the imaging membrane window was shadow masked (e.g., with tape), and the nitride in the inlets/outlets was etched with a RIE ($SF_6 + O_2$ chemistry).

Functional device yield was ≥90% in version 1, with loss occurring primarily during the KOH etch step, which caused some membranes to break. In all cases when breakage occurred, the larger, 300 μm membrane at the inlet/outlet broke, never the 100 μm viewing window. The broken membrane at the inlet/outlet allowed KOH into the conduit and these devices later proved difficult to fill with solution. Device yield was high in version 2 as well, ≥80%, with loss presenting itself during chip separation. Due to the uneven polishing that the wafers were subjected to (see Section 2.4), many wafers contained gashes or burn marks/streaks where a great deal of material was removed, to the point where the bulk silicon was exposed. Obviously, these regions of the wafer could not bond or produce functional devices, and fell apart while separating the chips from the wafer.

Section 2.9: Filling and Sealing

Devices were filled by placing a droplet of solution at the inlet and letting the solution fill the conduit by capillary imbibition. The nitride window was inspected in an optical microscope to check for color change, indicating that fluid was present. Once the conduit was filled, another droplet was placed at the opposite end. If a bubble was visible in the window during filling then the fluid was withdrawn using filter paper and the filling process repeated. Rubber O-rings (Markez -002 O-rings, Marco Rubber) were placed over the inlet and outlet, and the device was clamped in a custom-made titanium

fixture as illustrated in Figure 2-14. In some devices, the top and bottom membranes of the viewing window were collapsed, touching each other and preventing the fluid from freely entering the viewing chamber. This was remedied by a) simply waiting for the fluid to creep in and separate the membranes or b) clamping the device in the fixture to increase the pressure of the fluid, which then pushed the membrane apart (see Figure 2-15).

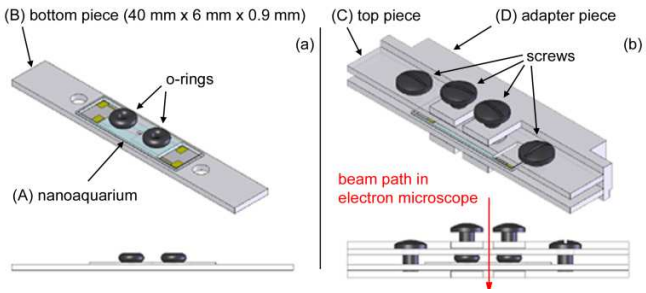

Figure 2-14: Illustration of the nanoaquarium mounted in a custom-made, titanium holder. (a) The nanoaquarium positioned in the holder's bottom with O-rings placed around the inlet and outlet ports. Top: isometric view. Bottom: side view. (b) The nanoaquarium in the fully assembled titanium holder. Top: isometric view. Bottom: side view.

The titanium fixture was designed for easy loading and unloading of nanoaquarium devices. The bottom piece (**B**) contained a recessed rectangular groove that the nanoaquarium (**A**) snugly sat in (Figure 2-14(a)). While in the groove, the membrane window of the nanoaquarium lined up with a thru-hole in the bottom of the fixture such that there was an unobstructed path for the electron beam. The top piece (**C**), which also contained a through-hole at its center, screwed onto the bottom piece with two plastic screws, thus compressing the O-rings to form a tight seal against the inlet and outlet of the chip. The assembled top and bottom pieces were inserted into a third titanium adapter piece (**D**) that snapped into a fixture in the STEM. Two plastic screws were used to secure the assembly within the adapter piece (**D**) and to provide additional compression on the O-rings to ensure a leak-proof seal (Figure 2-14(b)).

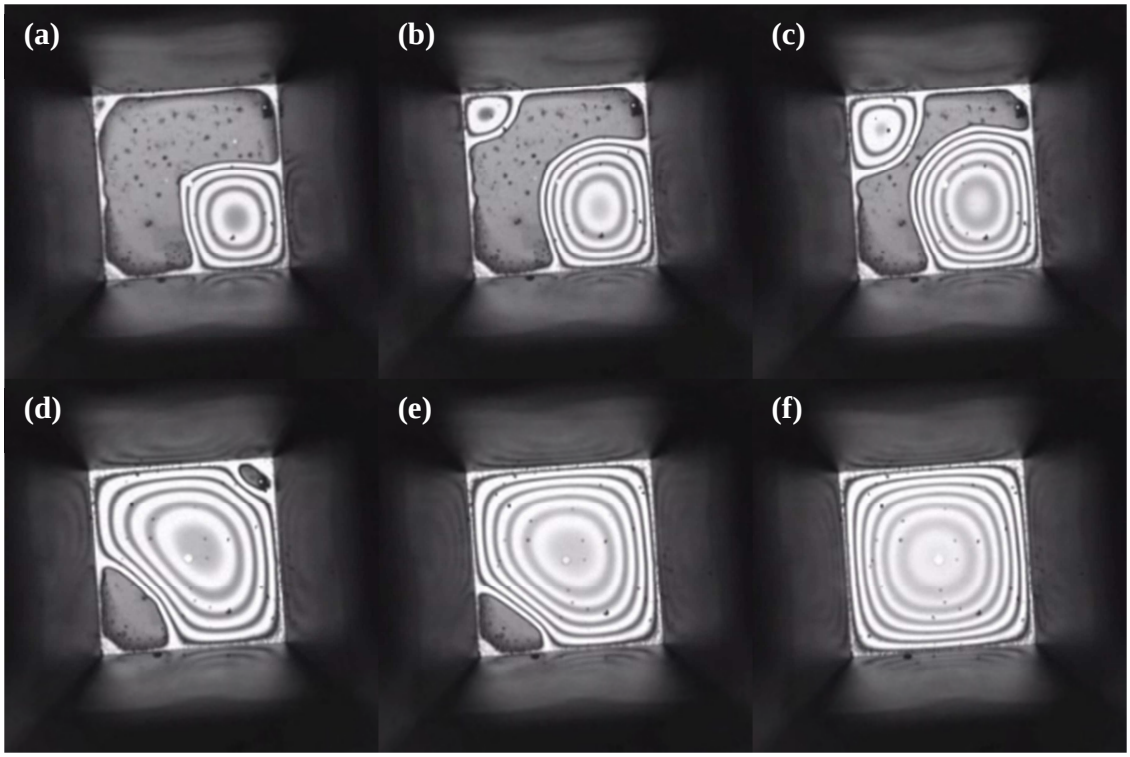

Figure 2-15: A series of bright field microscope images of a collapsed window being filled with a solution of nanoparticles in a glycerine-water mixture. The device is clamped firmly in the holder in order to drive fluid into the window. Approximately four seconds elapse between each frame.

The O-ring sealing approach was employed for experimental ease, as opposed to sealing with glue, epoxy, or the like, as in several of the other liquid-cell *in situ* (S)TEM devices discussed earlier [6–8], [10], [11]. In practice, we found that nanoaquarium devices could be filled with solution, clamped in the fixture, and loaded into the microscope for imaging in a matter of minutes. When an experiment was completed, the device was readily removed from the fixture and replaced with a new device.

The clamping fixture illustrated in Figure 2-14 was designed for closed-cell applications where the contents of the chip remain sealed for the duration of the experiment. However, the fixture/adapter design can readily be altered to include ports

for external tubing to allow the transmission of liquids through the device while it is in the vacuum chamber of the microscope.

Section 2.10: Shape of the Silicon Nitride Window

The silicon nitride imaging membrane of the device is relatively large (edge size of 100 μm) and extremely thin (thickness of 50 nm), and thus can deform a great deal without breaking. It was observed that when the device was filled with liquid, inserted into the titanium holder, and the screws were tightened, the liquid contents were inadvertently pressurized. The liquid, in turn, deformed the membrane. As the membrane deformed, light fringes in the nitride window, similar to Newton's rings, were observable with an optical microscope (Figure 2-16(a)). By adjusting the force with which the O-rings were clamped, the number of fringes changed, indicating that the membrane flexed outward due to the internal pressure of the liquid in the channel. As the height of the

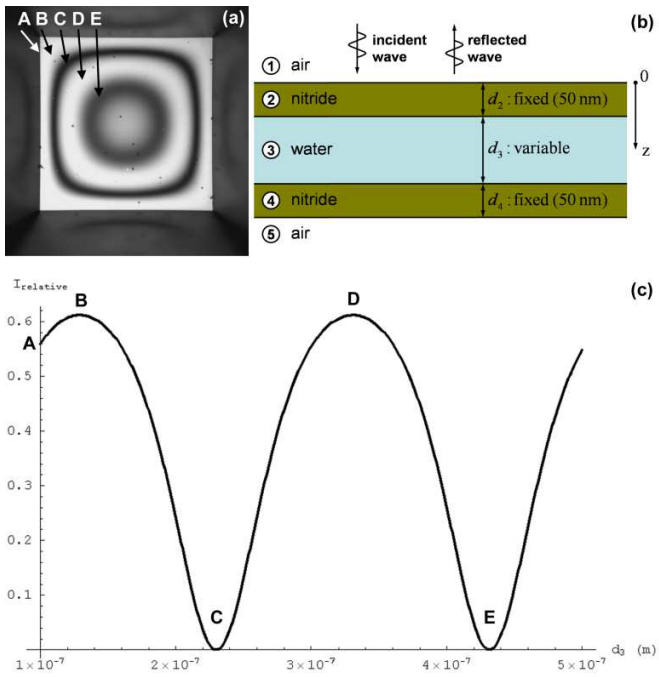

Figure 2-16: (a) Bright field light microscope image of a bowed membrane for a channel filled with water. (b) Illustration of the multiple-interface problem to be solved to estimate membrane deformation. (c) The relative intensity of the reflected light as a function of channel height when the device is filled with water and illuminated with green light (λ = 540 nm). The peaks and valleys of the plot correspond to light rings and dark rings, respectively, in the microscope image.

encapsulated channel changed with the curvature of the membrane, incident and reflected light interfered constructively and destructively to produce light and dark fringes. The precise shape of the window can be determined by modeling the light reflection and transmission in the multiple interface stack.

The nanoaquarium viewing window consists of multiple layers with four interfaces and five optically transparent media (Figure 2-16(b)). We ignore the slight curvature of the membranes' surfaces and assume normal incidence of the light. In each medium, there is a forward and a reverse instantaneous electromagnetic field traveling in the *z*-direction, represented as

$$\begin{aligned} E_{\text{forward},i} &= F_i \cdot E_0 \cdot e^{-j\beta_i z} \\ E_{\text{reflected},i} &= R_i \cdot E_0 \cdot e^{+j\beta_i z} \\ H_{\text{forward},i} &= E_{\text{forward},i} / \eta_i \\ H_{\text{reflected},i} &= -E_{\text{reflected},i} / \eta_i \,. \end{aligned} \tag{2-1}$$

In the above, E is the electric field, H is the magnetic field, subscript i denotes the medium, β is the phase constant, η is the intrinsic impedance ($\eta_i = \sqrt{\mu_i / \varepsilon_i}$), μ is the permeability, ε is the permittivity, and F_i and R_i are complex coefficients that represent the magnitude and phase of the wave. F_i and R_i are determined by enforcing continuity of the electric and magnetic fields at the interfaces:

$$\begin{aligned} E_{\text{forward},i} + E_{\text{reflected},i} &= E_{\text{forward},i+1} + E_{\text{reflected},i+1} \quad \{i = 1, 4\} \\ H_{\text{forward},i} + H_{\text{reflected},i} &= H_{\text{forward},i+1} + H_{\text{reflected},i+1} \; \{i = 1, 4\}. \end{aligned} \tag{2-2}$$

Without a loss of generality, the problem is normalized by the incident wave that illuminates the window in medium 1. Accordingly, F_1=1. Also, it is assumed that the wave that exits the stack to medium 5 does not reflect back. In other words, R_5=0. The

system of equations (2-1) and (2-2) is solved for F_i and R_i as functions of channel height (d_3) when the illumination is monochromatic.

The intensity of a wave is given by

$$I = \left|\vec{S}\right|_{\text{average}} \tag{2-3}$$

where $\vec{S} = \vec{E} \times \vec{H}$ is the Poynting vector. By taking the intensity of the reflected wave in medium 1 and scaling it by the intensity of the incident wave in medium 1, we end up with the following expression:

$$I_{\text{relative}} = \left|{R_1}^2\right|. \tag{2-4}$$

The relative permeability, μ_r, of all the layers (air, nitride, and water) was taken to be approximately equal to 1 because they are nonmagnetic materials. For illumination with monochromatic green light (wavelength λ = 540 nm), the refractive index, n, was taken to be approximately 1 for air [45], 2.03 for silicon nitride [46], and 1.34 for water [47]. Figure 2-16(c) depicts I_{relative} as a function of the channel height (d_3). Witness the periodic interference pattern. The peaks and valleys correspond, respectively, to light and dark fringes of the bowed membrane. The channel height at the edge of the membrane is a fixed quantity (100 nm) because the membrane is connected to a massive silicon structure with negligible deformation. Thus, the quantity and position of the light and dark fringes provides a means for characterizing the shape of the membrane window. For example, when two dark fringes are visible, the height of the conduit is estimated to be 230 nm at the outer fringe and 430 nm at the inner fringe. More generally, for a channel filled with water and two 50 nm thick silicon nitride membranes, a dark fringe appears

every 201.5 nm in liquid height. Additionally, for a channel filled with air and two 50 nm thick silicon nitride membranes, a dark fringe appears every 270 nm in chamber height.

Due to the very high aspect ratio of the membrane (a length to thickness ratio of 2000), the membrane can deform a great deal without breaking. When several dark fringes are visible in a sealed device, indicating that the membrane is severely bowed, then the pressure on the O-rings that seal the inlet and outlet can be relaxed until the membrane is sufficiently flat. In some of our experiments, the membranes were allowed to remain bowed out and the large deformation required us to restrict the imaging to regions close to the membrane's edges, where the thickness of the liquid layer was approximately 100 nm. The higher thickness liquid close to the window's center made it difficult to resolve the smallest features in the sample.

Observation of the shape of the bowed membrane provides a simple means to estimate the pressure inside the nanoaquarium. Maier-Schneider et al. [48] provide an analytical expression that relates the center deflection h of a square suspended thin film membrane to an applied pressure p given by

$$p(h) = 4\,C_1\,\frac{t\,\sigma}{a^2}\,h + 16\,C_2(\nu)\,\frac{t\,E}{a^4}\,h^3\,. \tag{2-1}$$

Creemer et al. [17] used this expression to estimate the deflection of the membrane in their high pressure *in situ* gas-cell. In this expression, a is the length of the membrane side, t is the membrane thickness, σ is the residual stress in the film, E is Young's modulus, and C_1 and $C_2(\nu)$ are numerical constants given by

$$C_1 = 3.45 \tag{2-2}$$

and

$$C_2(\nu) = 1.994\ (1 - 0.271\,\nu)/(1 - \nu) \tag{2-3}$$

where $C_2(\nu)$ depends on the in-plane Poisson's ratio ν. Non-deflected membranes are separated by a distance equal to the channel height. It is useful to consider the internal pressure p of the fluid in the device as a function of the change in separation distance at the center of the membrane window, given by total deflection $\Delta d = 2h$ (there are two membranes). When $a = 100$ μm, $t = 50$ nm, $\sigma = 800$ MPa, $E = 325$ GPa [49], and $\nu = 0.25$ [48], we find the relationship depicted in Figure 2-17. The applied pressure expression from equation (2-1) (plotted in Figure 2-17) represents the pressure of the fluid relative to the pressure on the other side of the membrane. When the measurement is made in a lab environment using an optical microscope, the applied pressure is relative to atmosphere, i.e., gauge pressure. In order to determine the absolute pressure of the fluid, we must add 101.325 kPa (1 atm) to the value in equation (2-1).

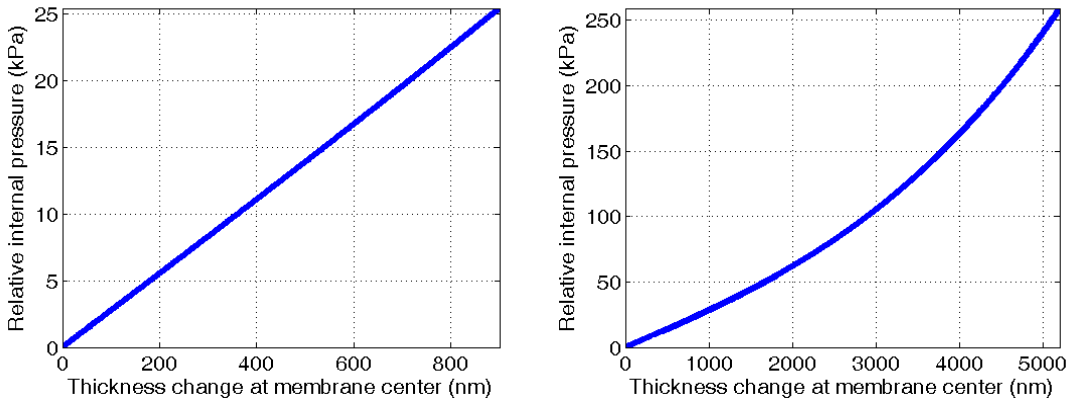

Figure 2-17: Relative internal pressure of the fluid in the nanoaquarium as a function of the change in height of the bulging observation window at its center. The pressure is relative to the ambient pressure of the environment on the other side of the membrane (1 atm when the measurement is performed in a lab environment). Two ranges of thickness change are displayed in order to highlight the initially linear trend, which becomes nonlinear for large change in thickness.

Section 2.11: Device Validation

2.11.1: Leak Tests & Basic Imaging

Device performance was demonstrated using an aqueous solution containing 5 nm gold particles (EM.GC5, BBI Life Sciences), 50 nm gold particles (EM.GC50, BBI Life Sciences), and 50 nm fluorescent polystyrene particles (Fluorescent Yellow Particles, Spherotech) suspended in water. The fluorescent particles enabled imaging with a fluorescent optical microscope during the initial debugging stage of the device. Brownian motion of the fluorescent particles was observed through the silicon nitride window. The device remained sealed for approximately 20 hours, at which time the window was observed again and fluorescent particles were seen still diffusing randomly. There had been no appreciable loss of fluid in that time interval. The sealed device was then placed in an FEI Quanta 600 FEG Mark II scanning electron microscope with STEM detector. The microscope was operated in high vacuum mode (~1E-5 Torr) with an acceleration voltage of 20 kV. Real-time video lasting several minutes was recorded; though, there is no limitation on observation time. The video showed individual gold nanoparticles and aggregates of various sizes diffusing through the field of view, sometimes bumping into each other to form larger aggregates. The motion of individual particles as well as aggregates was clearly visible with good resolution. Figure 2-18(a) features an instantaneous bright field STEM image taken from the recorded video. Figure 2-18(b) is a higher magnification bright field STEM image of a single 50 nm gold particle. Witness the excellent contrast between the high density gold particle and the suspending water. Clearly, the STEM provides high contrast images of the suspended particles at a

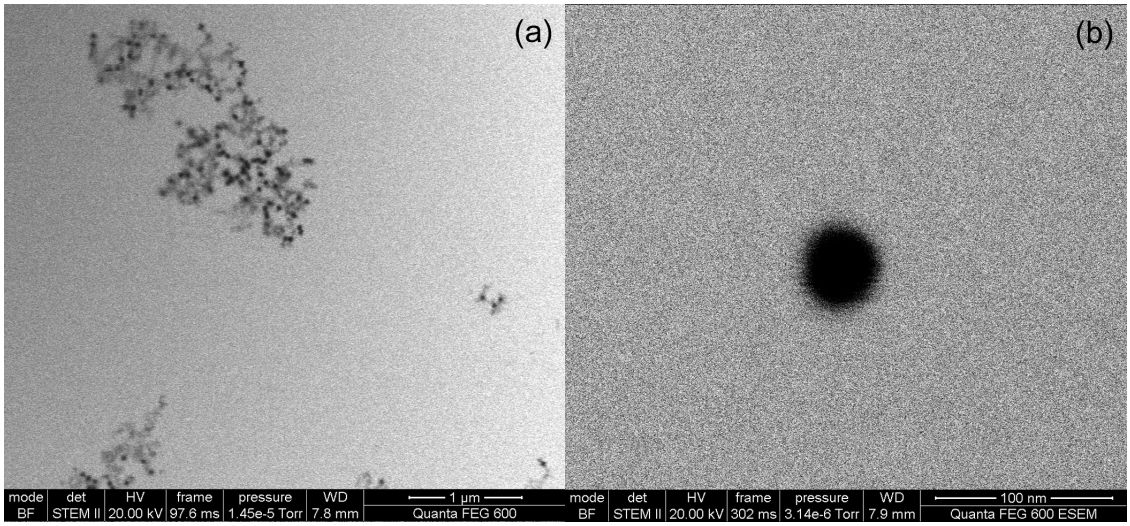

Figure 2-18: (a) A bright field STEM image of an aqueous solution containing 5 nm gold particles, 50 nm gold particles, and 50 nm fluorescent polystyrene particles. Individual particles as well as aggregates are visible with excellent resolution. 50 nm gold particles are seen most prominently decorating the aggregates. (b) A bright field STEM image of a single 50 nm gold particle in water.

relatively low acceleration voltage. Even higher resolution images should be attainable with a TEM or STEM that is capable of higher acceleration voltages with correcting electron optics.

The device used in this initial experiment remained sealed in the fixture for 2 days of observation with no appreciable loss of fluid. Several STEM videos recorded over the course of this 2 day period demonstrated that particles/aggregates were continuously diffusing about in a random manner. The motion of these particles/aggregates verified that they were in fact suspended in liquid and that the device was leak-free in the high vacuum microscope chamber.

Another device filled with an aqueous solution of 5 nm gold particles remained sealed in the fixture for 13 consecutive days. STEM imaging performed at the start and end of this time period confirmed there had been no significant loss of fluid, as evidenced

by the persistent diffusive motion of suspended particles. This indicates excellent device hermeticity.

In the course of the imaging experiments, with beam intensities up to 30 kV, no bubbles were observed to form in the liquid-cell. This indicates that the liquid remained well below its boiling temperature. The lack of excessive heating may be due to both the relatively low energy of the electron beam and the thinness of the liquid-cell that facilitates efficient heat transfer to the silicon substrate.

2.11.2: Electrode Functionality

Functionality of the electrodes in version 1 of the nanoaquarium proved problematic. As mentioned in Section 2.2, the appearance of the gold electrodes in version 1 devices was troubling. Not surprisingly, they did not seem to function properly in most of the devices tested. Section 4.1 describes a strange outcome produced by the gold electrodes in a version 1 device. As also mentioned in Section 2.2, the electrode material was changed from gold to platinum in version 2 of the device. In collaboration with a research group headed by Dr. Frances M. Ross at the IBM T. J. Watson research center, version 2 of nanoaquarium was used for *in situ* imaging of deposition and stripping of copper in a copper sulfate solution (copper sulfate and sulfuric acid, 0.1M $CuSO_4$ + 0.18M H_2SO_4). The nanoaquarium was loaded into the TEM (Hitachi H9000) using a custom-made sample holder with electrical connections, constructed at IBM. In the experiment, deposition and stripping was performed through cyclic voltammetry and under potentiostatic conditions at a variety of potentials. In a “low” voltage potential sweep (-0.6V to +0.6V relative to open circuit potential), sparse nucleation and growth of

distinct clusters was observed (Figure 2-19). In a “medium” voltage potentiostatic deposition and stripping process (+0.8V relative to open circuit potential), dense nucleation that coalesced to form a continuous film was observed, along with some lateral growth beyond the electrode edge (Figure 2-20). And in a high voltage potentiostatic deposition process (+1.2V relative to open circuit potential), rapid coverage of the electrode followed by lateral growth of dendrites was observed (Figure 2-21). The relationship between applied potential and morphology of deposited copper is in keeping

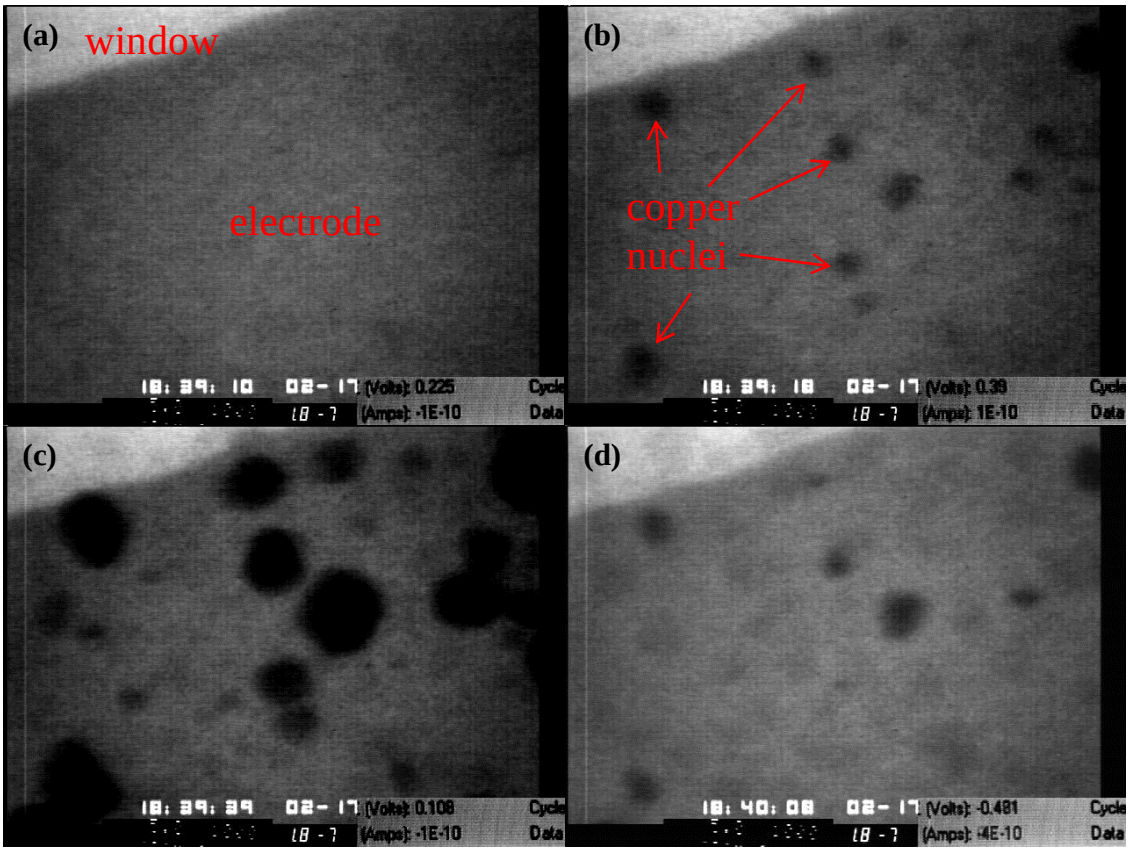

Figure 2-19: *In situ* TEM images of electrodeposition of copper on platinum electrodes from a solution of copper sulfate. The potential was swept from -0.6V to +0.6V relative to the open circuit potential. The image sequence shows the nucleation, growth, and then stripping of copper deposits on the electrodes. Horizontal field of view in each image is 1850 nm.

with expectations [6], [7] and successfully demonstrates functionality of the electrodes. It also confirms that the nanoaquarium can handle harsh chemistries with no failure issues and can be used for electrochemical studies.

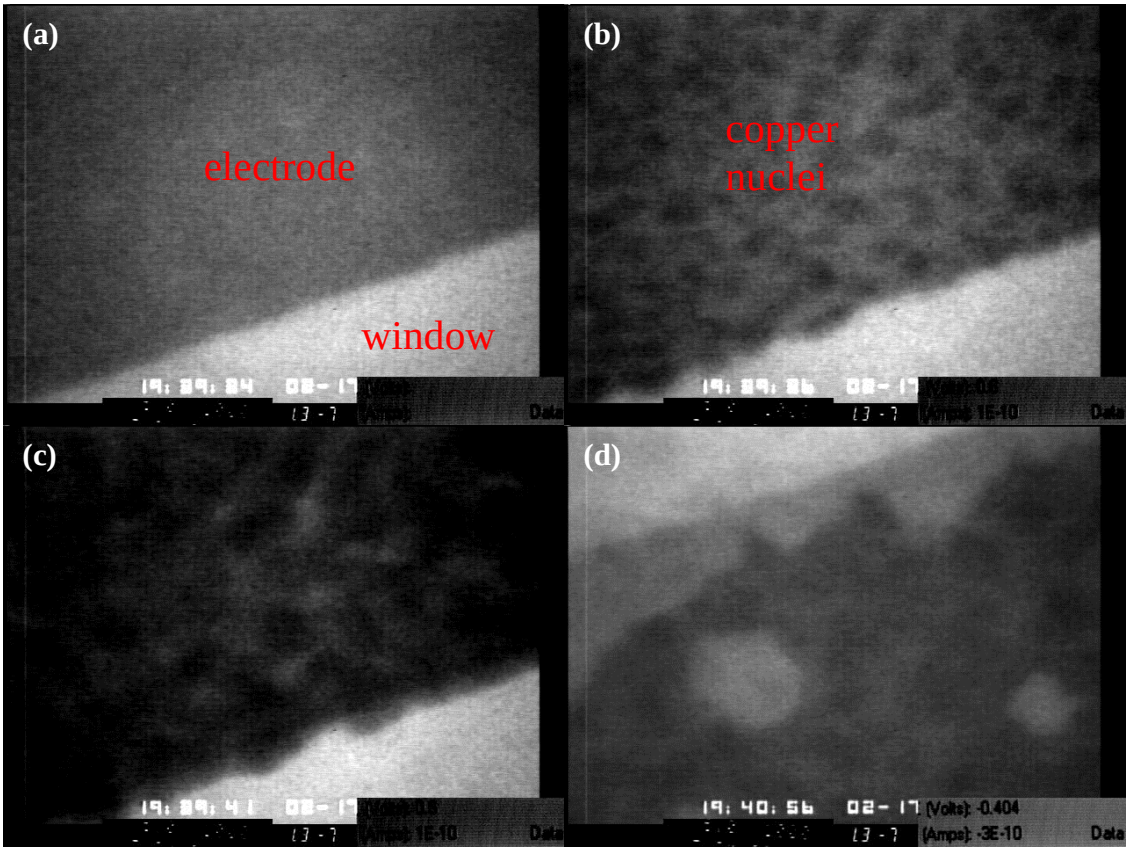

Figure 2-20: *In situ* TEM images of electrodeposition of copper on platinum electrodes from a solution of copper sulfate. (a)-(c) Potentiostatic deposition at +0.8V relative to the open circuit potential. Nuclei are more numerous than in Figure 2-19. (d) Potentiostatic stripping of the copper film at a different location on the electrode. Horizontal field of view in each image is 1850 nm.

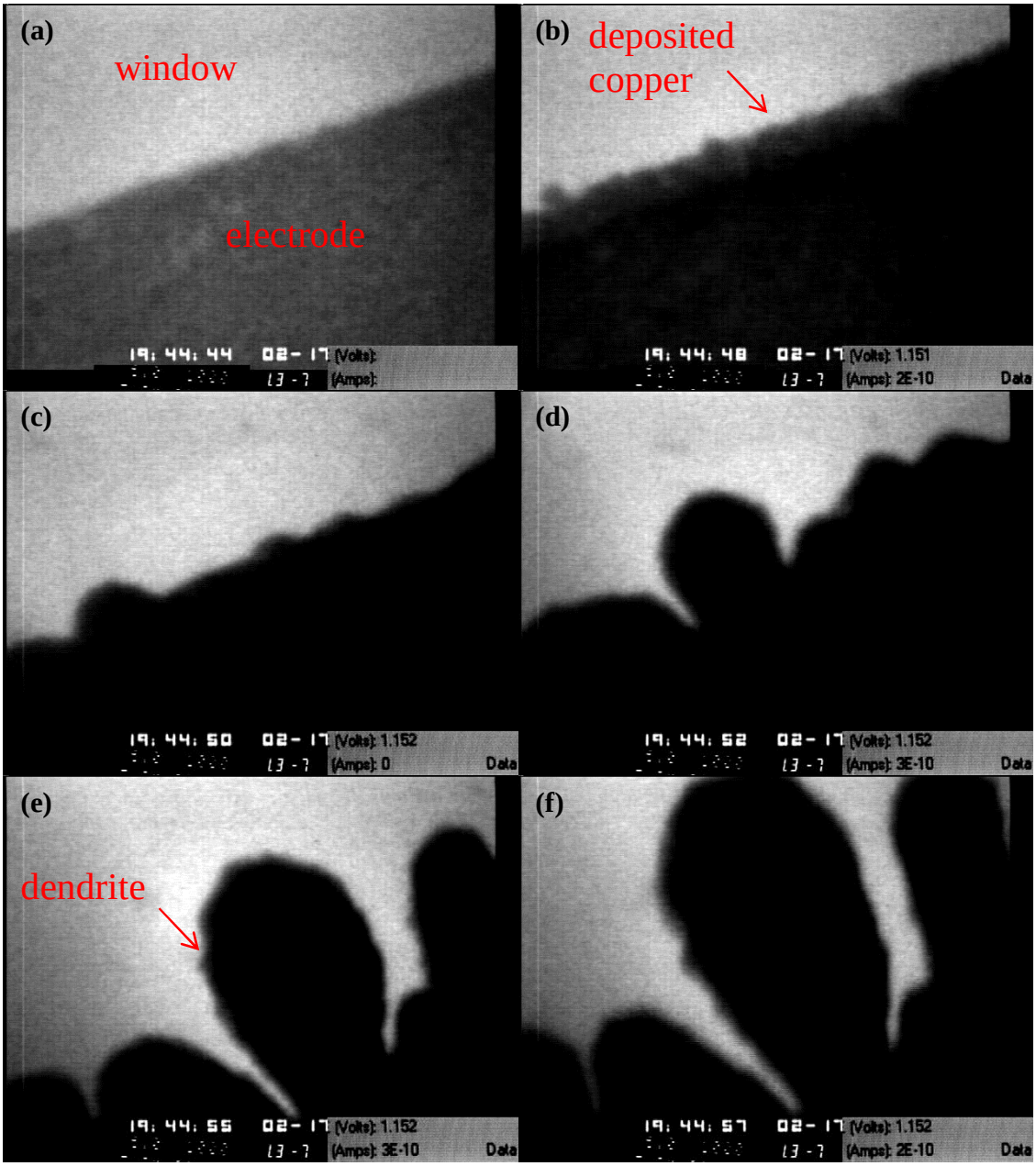

Figure 2-21: ***In situ*** **TEM images of electrodeposition of copper on platinum electrodes from a solution of copper sulfate. (a)-(f) Potentiostatic deposition at +1.2V relative to the open circuit potential. Rapid coverage of the electrode followed by growth of dendrites is seen. Horizontal field of view in each image is 1850 nm.**

Chapter 3: Diffusion Limited Aggregation

Section 3.1: Background

Aggregation is a classical topic of broad interest in disciplines such as condensed matter physics, material science, air and water pollution, and medicine. Nanoparticle aggregation is of interest, among other things, for the synthesis of colloidal crystals and the formation of meta and ceramic materials with unique properties. Some of the earliest experimental work in the field of nanoscale colloid aggregation & growth was performed by Weitz et al. [51], [52] and Lin et al. [53], [54] on systems of aqueous gold colloids undergoing irreversible kinetic aggregation to form tenuous, chainlike fractal structures. Since then, a rich theoretical and modeling framework has been developed with emphasis on kinetic models [55–57] and computer simulations with applications of the Smoluchowsky theory [58–62]. To this day, however, experimental work that captures the dynamics of nanoscale colloid assembly/crystallization is scarce [63], due in large part to the difficulty of *in situ* observation of complicated nanoscale phenomena in liquid media with an appropriate level of spatial and temporal resolution. A common experimental approach is to grow aggregates/crystals under prescribed conditions (e.g. by hydrothermal coarsening) and then freeze or dry out the sample to examine the resultant structure with TEM to indirectly infer details of the growth mechanism [64–67]. Except for some unique cases [64], [68], this technique does not capture dynamics of the

aggregation process. Dynamic light scattering and static light scattering are common experimental techniques for studying particles in solution. While these techniques provide dynamical information regarding aggregate size and fractal dimension, they are ensemble techniques that give bulk statistics averaged over the cluster mass distribution [54] and cannot capture individual events. In contrast, with the nanoaquarium, one can collect statistical information on an ensemble of clusters in view while also observing interactions between individual particles/clusters.

Zheng et al. studied nanoparticle migration in a liquid-cell TEM device and reported on anomalous diffusion behavior [10]. In their experiment, the observed phenomena may have been influenced by leakage from the liquid-cell. In contrast to Zheng et al.'s device, the nanoaquarium is perfectly sealed and is ideally suited for the study of nanoparticles in solution.

The nanoaquarium was used for real-time STEM imaging of diffusion limited aggregation/assembly of gold colloids. The deduced kinetics of the observed phenomenon in the early stages of aggregate growth agreed well with predictions based on three-dimensional cluster-cluster diffusion-limited aggregation models. Large aggregates exhibited properties of clusters grown in a three-dimensional regime, even when the characteristic size of the clusters exceeded the height of the nanoaquarium (tens of nanometers) and two-dimensional growth characteristics may have been expected. The mechanism for this seemingly paradoxical result was revealed through direct observation of the aggregation process, facilitated by the nanoaquarium.

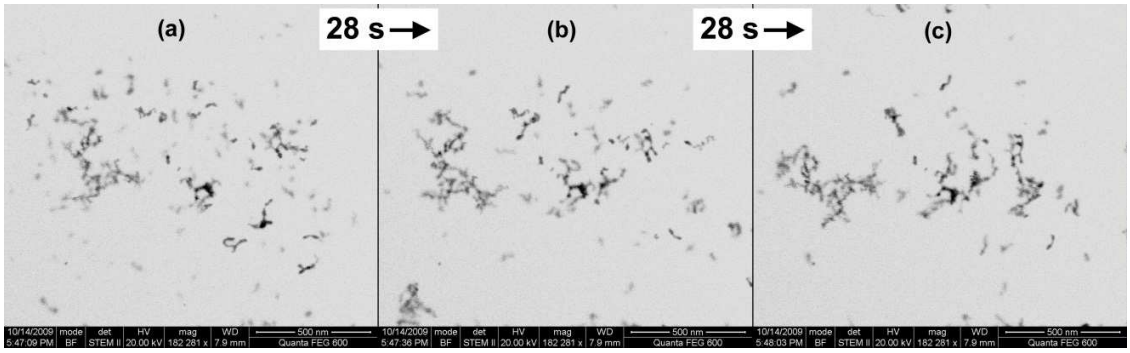

Figure 3-1: Aggregating nanoparticles. Three frames from recorded video of 5 nm gold particles and clusters composed thereof, as observed *in situ* with STEM.

Section 3.2: Experiment

An aqueous solution of amorphous, charge-stabilized, 5 nm diameter gold colloids (EM.GC5, BBI Life Sciences) was drawn into the nanoaquarium by surface tension forces. Imaging was carried out with a FEI Quanta 600 FEG Mark II with a STEM detector. The microscope was operated at 20-30 kV. Better resolution would likely be attained with higher power TEMs (acceleration voltage of up to 300 kV). The nanoaquarium was translated within the microscope to observe various regions of the imaging window. Some of the

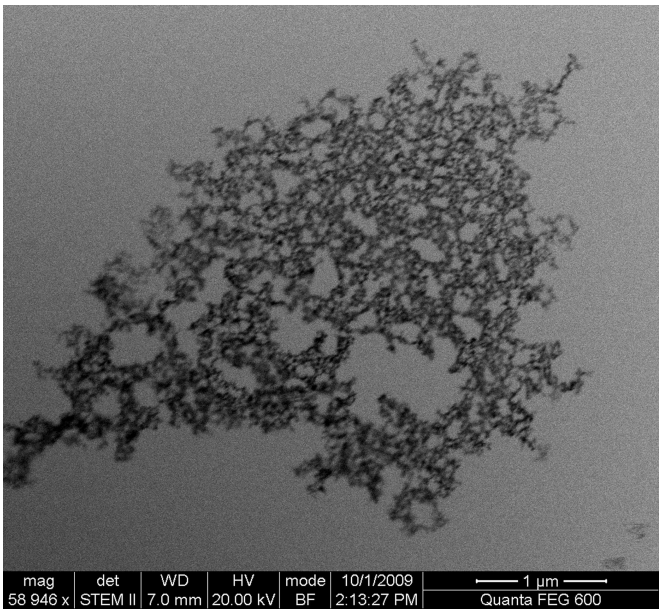

Figure 3-2: An aggregate composed of 5 nm diameter gold particles. The fractal dimension, D_f ~ 1.77, is consistent with three-dimensional cluster-cluster diffusion-limited aggregation.

regions featured small clusters of particles in the process of aggregating (Figure 3-1) and others contained sizable aggregates (Figure 3-2).

Section 3.3: Modeling and Analysis

A simple kinetic model that characterizes the aggregation process was proposed by Meakin [69]. Briefly, the number of clusters (N) is inversely proportional to the mean cluster size (S) measured by the number of primary particles composing the cluster:

$$N \sim S^{-1}. \tag{3-1}$$

The mean cluster radius (R) measured by a bounding circle is

$$R \sim S^{1/D_f}, \tag{3-2}$$

where D_f is the fractal dimension of the clusters. A coarse grain model describes the rate of decrease in the number of clusters:

$$\frac{dN}{dt} \sim -(N)\left(N \cdot R^d\right)\left(R^2/S^\gamma\right)^{-1}. \tag{3-3}$$

The second term in the parenthesis on the r.h.s. of equation (3-3) represents the probability that a cluster will encounter another cluster. The exponent d (= 3) is the space dimension. The third term represents the inverse of the average time interval between collisions. The diffusion coefficient of a cluster containing S particles is

$$D \sim S^\gamma. \tag{3-4}$$

Substituting equations (3-1) and (3-2) into equation (3-3) yields

$$\frac{dN}{dt} \sim -N^\nu, \tag{3-5}$$

where

$$\nu = 2 + 2/D_f - d/D_f - \gamma . \tag{3-6}$$

Integrating equation (3-5), we have

$$N \sim (t + t_0 + 1)^{1/(1-\nu)} . \tag{3-7}$$

In the above, t = 0 is the time when observations began, and t = -t_0 is the start of the aggregation process. According to the Stokes-Einstein equation, the diffusion coefficient is

$$D = \frac{k_B \cdot T}{6 \cdot \pi \cdot \mu \cdot R} = \frac{k_B \cdot T}{6 \cdot \pi \cdot \mu \cdot S^{1/D_f}} , \tag{3-8}$$

where μ is the viscosity of the suspending medium, k_B is the Boltzmann constant, T is the temperature, and the relation in equation (3-2) has been applied. With the aid of equation (3-4), we conclude that the exponent

$$\gamma = -1/D_f . \tag{3-9}$$

Substituting equation (3-9) into equation (3-6) with d = 3 results in ν = 2. Thus,

$$N \sim (t + t_0 + 1)^{-1} , \tag{3-10}$$

$$S \sim (t + t_0 + 1), \tag{3-11}$$

and

$$R \sim (t + t_0 + 1)^{1/D_f} . \tag{3-12}$$

The video footage for the process pictured in Figure 3-1 was analyzed using ImageJ, and nonlinear least squares fitting of the data was performed with Matlab. Figure 3-3 depicts D_f (mean for all clusters in view) and N_0, the number of primary particles present in the image (whether alone or as part of a cluster) (a); N (b); S (c); and R (d) as functions of time for a single set of analyzed images (see Appendix A for further details

of the image processing and image analysis, as well as details of the subsequent data fitting). As time progresses, D_f increases slowly towards its asymptotic, long term value of D_f ~ 1.77 (measured for Figure 3-2), which is in good agreement with Meakin's computational results for cluster-cluster aggregation (D_f ~ 1.75 – 1.80) [69] and Weitz et al.'s experimental results for diffusion-limited aggregation of gold nanoparticles (D_f ~ 1.75) [51]. The fitted exponent for N is -1.0 ± 0.1 and the fitted exponent for S is 1.0 ± 0.1, in close agreement with theory. The fitted exponent for R is 0.5 ± 0.2, which is

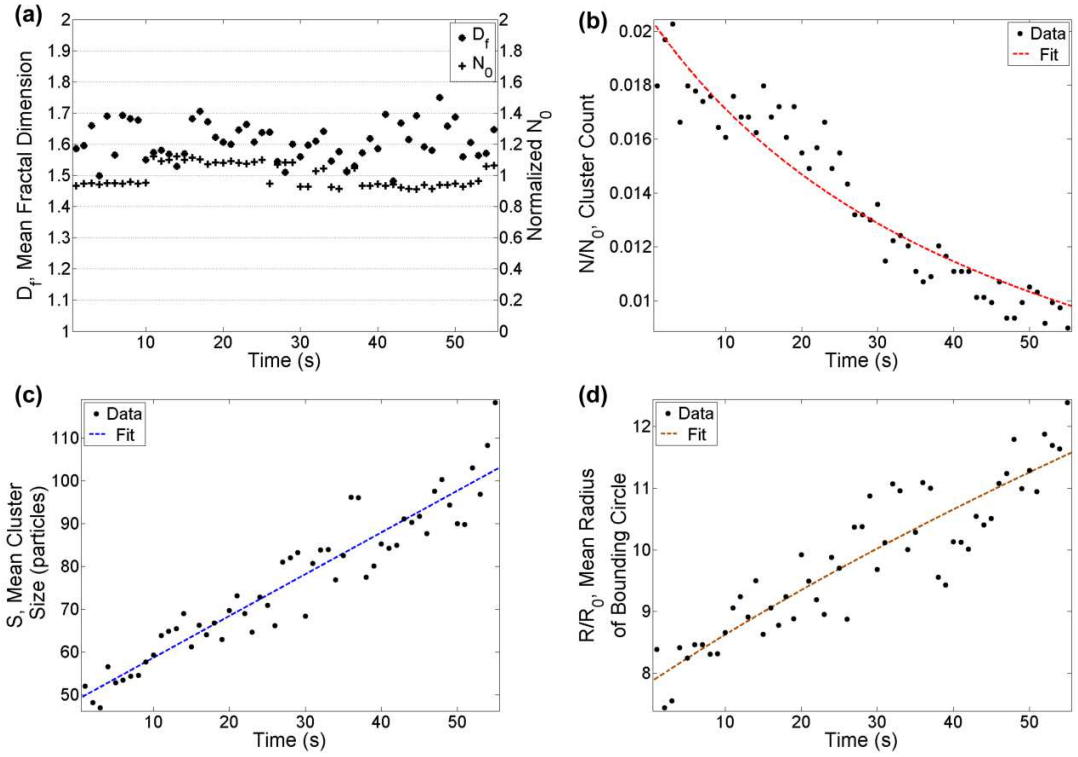

Figure 3-3: Analysis of the diffusion-limited aggregation process pictured in Figure 3-1. The symbols and lines correspond, respectively, to raw data and least squares fits. (a) The mean fractal dimension (D_f) increases slowly as a function of time as the aggregates acquire individual particles and small clusters. The number of primary particles (N_0) accounted for in the image, normalized by the time average of N_0, varies by < 20 % and indicates that mass is conserved. (b) The number of clusters decays as $(t + 1)^{-1}$. (c) The mean cluster size increases nearly linearly with time. (d) The mean cluster radius grows with an exponent of $1/D_f$ = 0.5. The scatter of the data can be attributed, in part, to particles and clusters moving in and out of the field of view from one frame to the next.

approximately the inverse of the time-averaged fractal dimension (Figure 3-3(a)): $(< D_f >)^{-1} \sim 0.63$. The good agreement between theory and experiments indicates that the Stokes-Einstein equation adequately describes the diffusion of nanoparticles in the nanosize fluid cell. This is in contrast to the results of Zheng et al. [10], whose liquid-cell was subject to leakage and associated effects that could include evaporation, convective flow, capillary forces, and nucleation of vapor bubbles.

Interestingly, the lateral dimension of the cluster pictured in Figure 3-2 is an order of magnitude larger than the cluster's height (dictated by the nanochannel's height); yet the fractal dimension is consistent with three-dimensional growth, rather than two-dimensional growth. Theoretical models for simple diffusion-limited aggregation, in which particles are added one at a time to a single immobile growing cluster via random walk trajectories, predict clusters with $D_f \sim 1.72$ for two-dimensional growth and $D_f \sim 2.5$ for three-dimensional growth [69]. These models are, however, inappropriate for our experiments. In our experiments, clusters are not immobilized; they clearly move and combine (see Figure 3-1 and Figure 3-4). Theoretical models for cluster-cluster diffusion-limited aggregation, in which particles and clusters are allowed to move via random walk trajectories and combine, predict clusters with $D_f \sim 1.4 - 1.45$ for two-dimensional growth and $D_f \sim 1.75 - 1.8$ for three-dimensional growth [69]. This raises the question: why do relatively large clusters exhibit characteristics of three-dimensional growth when two-dimensional growth might have been expected?

Our *in situ* imaging helps to shed light on the formation of large aggregates in a shallow conduit. Initially, clusters assemble from individual particles that are small relative to the conduit height, and follow a three-dimensional growth habit, as illustrated in Figure 3-3. Subsequently, when the size of the clusters approaches the height of the channel, the clusters' movement is confined to a plane and growth is dominated by lateral cluster-cluster aggregation. Since these aggregating clusters already possess characteristics of growth in a near-three-dimensional regime, these characteristics are preserved in the resulting aggregate. Figure 3-4 depicts two clusters with fractal dimensions of ~1.67 and ~1.65 (appropriate values considering the upward trend of D_f in Figure 3-3(a)) coming together to form a larger cluster with a fractal dimension of ~1.64. Additionally, small clusters and individual particles are free to diffuse into the body of a large cluster, further adding to the structural complexity of the aggregate. Figure 3-5 depicts the fractal dimension as a function of aggregate size for several aggregates observed in our experiments. As the cluster size

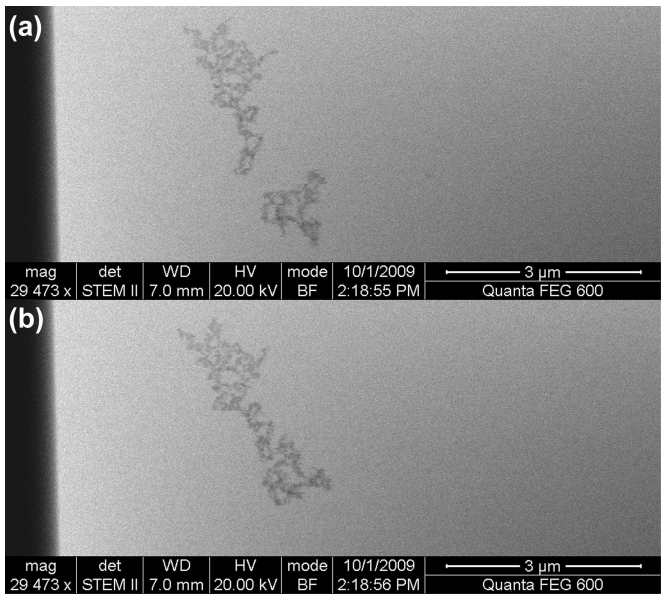

Figure 3-4: Cluster-cluster aggregation. Two distinct clusters (a), come together to form a single cluster one second later (b). Small clusters formed in a three-dimensional growth regime go on to aggregate two-dimensionally, resulting in large aggregates with three-dimensional characteristics, despite confinement in a narrow channel.

increases, there is a narrowing of the variation in fractal dimension, along with an upward trend in the fractal dimension towards the long term value consistent with three-dimensional growth.

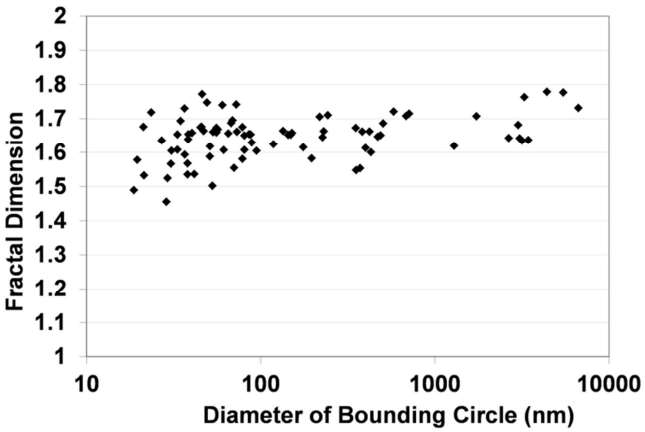

Figure 3-5: Fractal dimension as a function of size for 84 aggregates. Large aggregates possess fractal characteristics consistent with three-dimensional growth.

Chapter 4: Particle Motion in an Evaporating Thin Liquid Film: Experiments

In Chapter 3, we saw that the nanoaquarium is an effective tool for investigating nanoparticle aggregation in solution when the nanoparticles are completely submerged in the suspending liquid and absent of interfaces. The nanoaquarium can also be used to investigate the behavior of nanoparticles confined to interfaces and to study the effect of interface shape on particle motion and aggregation. In this chapter, experimental observations of the motion of particles in an evaporating thin film of liquid, as well as at a three phase contact line are described. The observations and results reported herein are relevant to techniques such as dip-coating and drop-casting, which are commonly used for deposition of nanoparticles on a surface via convective-capillary assembly. In Chapter 5, the underlying physics responsible for the observations reported in this chapter will be delineated.

Section 4.1: Experimental Setup

The circumstances leading to the series of experiments discussed in this chapter occurred serendipitously. Once it became apparent that an interesting set of phenomena was presenting itself, the experiments were steered in such a way as to exploit the unique circumstances and investigate the phenomena at hand.

Version 1 of the nanoaquarium was filled with an aqueous solution of gold nanorods (20 nm x 40 nm) with surfactant CTAB (cetrimonium bromide). The suspension was provided by Xingchen Ye and Professor Christopher B. Murray of the

Chemistry department and Materials Science department at the University of Pennsylvania.

Imaging was performed in a FEI Quanta 600 FEG Mark II with a STEM detector, operated at an acceleration voltage of 30 kV. An AC electric potential was applied to the two embedded window electrodes in an effort to observe *in situ* dielectrophoretic assembly of the nanorods to form nanowires, as was previously demonstrated *ex situ* by Hermanson et al. [70]. As discussed in Section 2.2, there was something wrong with the electrodes in version 1 of the nanoaquarium. The magnitude and frequency of the applied potential was varied (0 – 5 V, 100 – 1000 Hz), yet no dielectrophoretic assembly was seen. Instead, the gold electrodes eroded and gold was deposited on the silicon nitride membrane windows (Figure 4-1), most likely as hemispherical deposits. The applied potential was raised until it reached approximately 15V at 500Hz, at which point a bubble formed, displacing liquid to the perimeter of the imaging window, but leaving a thin film of liquid on the membrane surface. The gas/vapor bubble (bright region) can be seen clearly in the microscope image featured in Figure 4-2. The bubble is illustrated schematically in Figure 4-3. The electric potential was turned off and remained off for the rest of the experiment. From Figure 4-2(b) we can count approximately 16 dark fringes present for a medium of air or water vapor (both of which have a refractive index close to 1). Referring back to Section 2.10, where the shape of the bowed membrane window was characterized, we can estimate that at the center of the window, the change in height of the channel is ~4300 nm. Using equation (2-1), or referring to Figure 2-17, we conclude that pressure of the gas is approximately 180 kPa relative to atmosphere.

The nanoaquarium was translated in the microscope to interrogate various regions of the window. Gold particles, deposited from the eroded electrodes, were found scattered across the membrane in the gas/vapor-filled region of the window, along with occasional nanorods. Most of the nanorods, however, were carried to the perimeter of the imaging window and remained in the liquid region. The confluence of events that

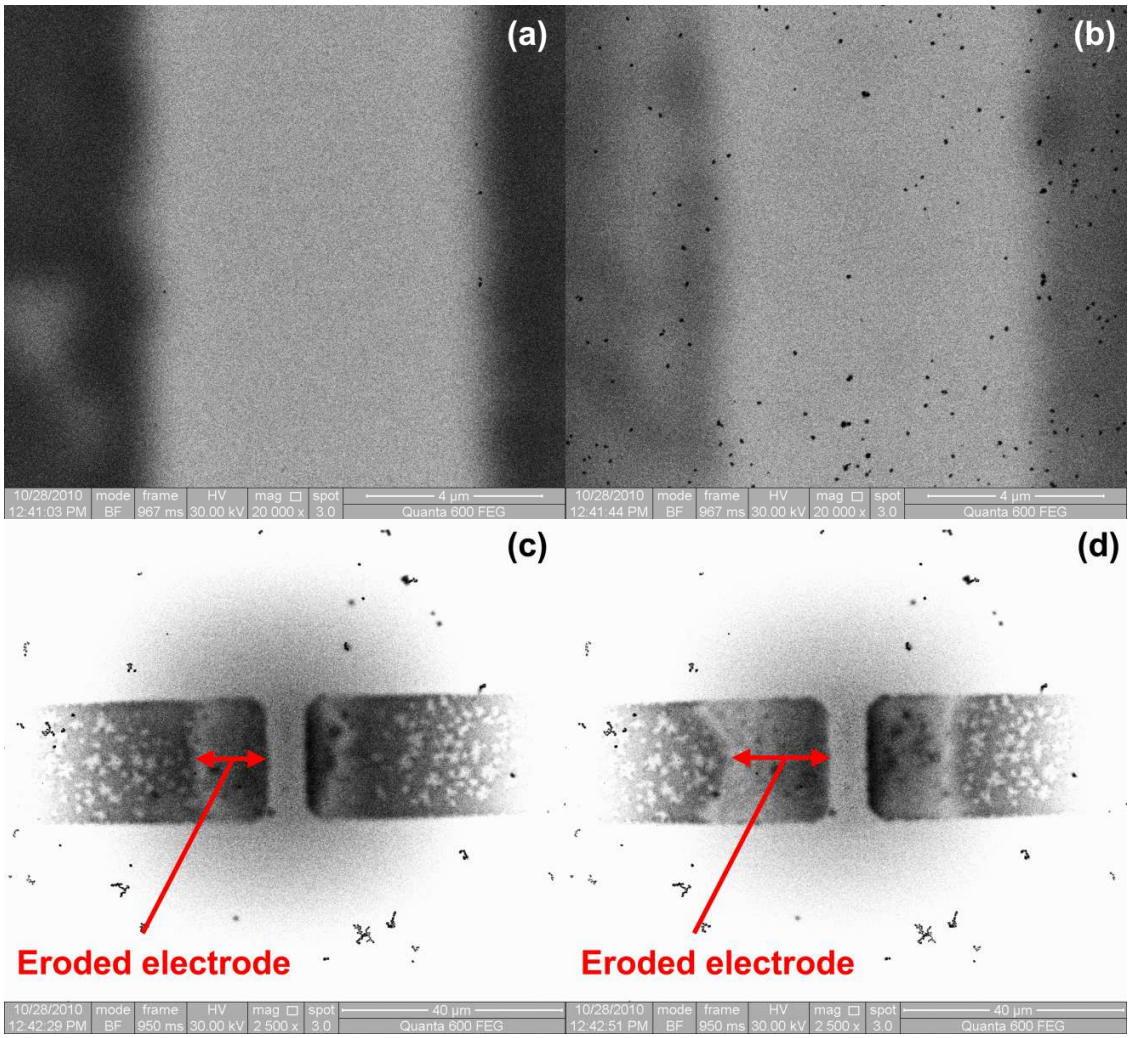

Figure 4-1: Electrochemical erosion of gold electrodes in version 1 of the nanoaquarium. (a), (b) As the electrode (dark regions) material dissolves, gold is deposited on the nitride membrane window. (c), (d) With time, the electrodes erode significantly. 41 second elapse between (a) and (b), 22 seconds elapse between (c) and (d).

occurred makes this a difficult experiment to reproduce exactly. However, one could certainly reproduce this experiment with a different approach. Generating a bubble with the electrodes is not difficult; in fact, bubble generation in microfluidic devices is often a problem that researchers must combat. Regarding nanoparticle deposits on the membrane, it has been demonstrated by Donev and Hastings [71] that electron beam-induced deposition (EBID) from liquid precursors can yield precisely controlled nanoscale deposits of materials such as Pt. With liquid-phase EBID, one could deposit metallic nanoparticles deterministically on the nanoaquarium window, and then generate a gas bubble with the electrodes, resulting in a scenario similar to the one described in this chapter.

Experimental observations were focused on two regions of the imaging window.

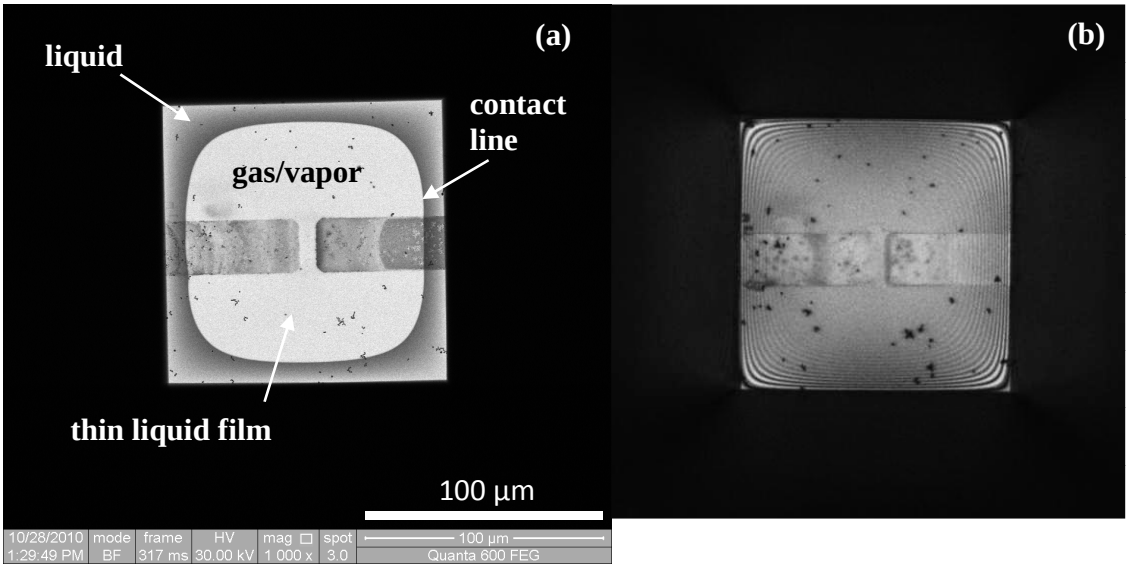

Figure 4-2: (a) Scanning transmission electron microscope image of the device imaging window with a gas/vapor bubble occupying most of the imaging window, with liquid present around the perimeter. (b) Bright field optical microscope image taken several hours later. During that time the liquid front receded and the bubble came to occupy nearly the entire imaging window. There is a small amount of liquid visible in the four corners.

One region was the interface between the bubble and the "bulk" liquid around the perimeter of the window (see Figure 4-2(a) and Figure 4-3). We refer to this interface as the contact line and our observations of particles at the contact line are detailed in Section 4.3. The term contact line can imply a liquid/vapor/solid interface, while in our case we have a liquid/vapor/thin liquid film interface. However, as details emerge about the complex nature of contact lines and the wetting of surfaces [1], [72], it seems that a liquid/vapor/thin liquid film interface is in fact the reality, and not unique to our case. Later in Chapter 5, we make reference to a contact line model, which applies to this region. The other region of interest was away from the contact line, in the thin liquid film

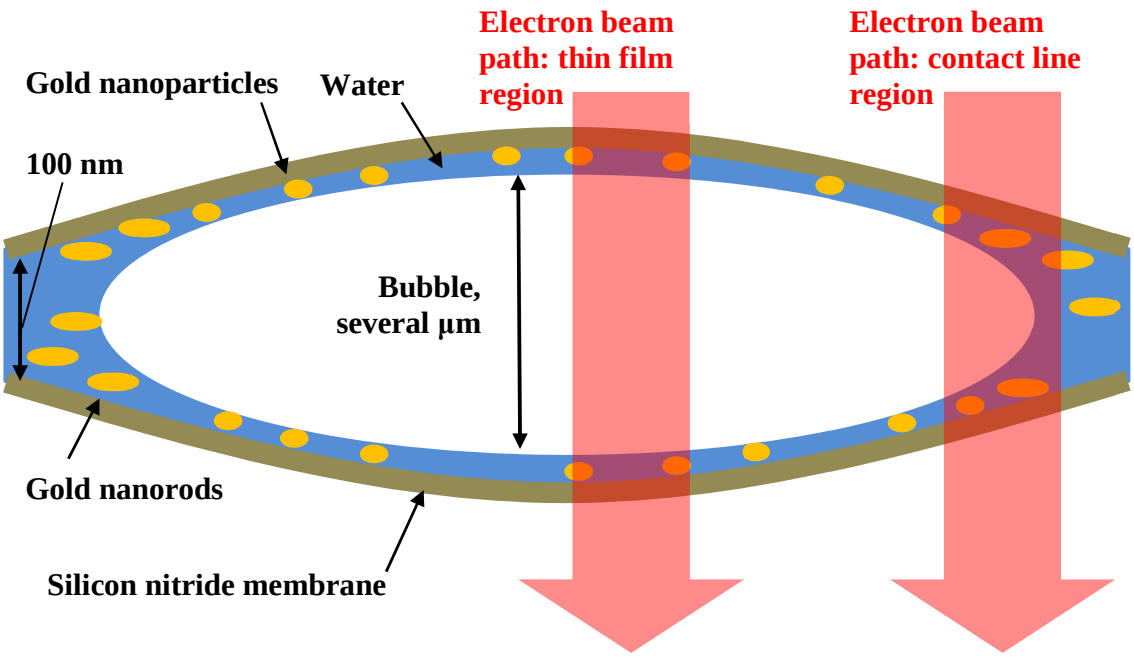

Figure 4-3: Cross sectional illustration of the nanoaquarium with a bubble occupying most of the cross section. Gold nanorods were found in the "bulk" liquid at the perimeter, and electrodeposited nanoparticles were found in the thin liquid film. The electron beam path is indicated with red arrows. Two regions were interrogated: the contact line region and the thin film region.

that coated the silicon nitride membrane in the gas/vapor region. (see Figure 4-2(a) and Figure 4-3). We refer to this as the thin film region and our observations of particles in the thin film are detailed in Section 4.4 and Section 4.5. Later in Chapter 5, we make reference to the heated patch model, which applies to this region.

Section 4.2: Convective-Capillary Assembly Background

Self-assembly of nanoparticles to form crystalline films is a fascinating topic with increased interest in the last decade. Some of the earliest work in this field by Kralchevsky, Nagayama, and collaborators [73–75] indicated that capillary forces between partially exposed particles in a thin film of liquid can drive aggregation of nanoparticles because the interaction energy is greater than $k_B T$ even for particles as small as a few nanometers in diameter. This is in contrast to conventional lateral capillary forces between floating particles, for which the interaction energy for assembly is smaller than $k_B T$ when the radius of the particles is a few micrometers or smaller. The flotation force (associated with particles floating on liquid), as Kralchevsky and Nagayama refer to it, relies on particle weight to deform the fluid interface. Particles below a few microns are too small to sufficiently deform the interface to drive assembly. Kralchevsky and Nagayama show that the immersion force (associated with particles on a surface protruding from a thin liquid film), on the other hand, has a different functional dependence on particle radius and surface tension of the liquid that makes it significant for even nano-size particles [73]. Nagayama reported that with a liquid film whose thickness is comparable to the particle size, colloidal particles self-assemble to form

hexagonally packed crystal arrays [74]. He postulated that two distinct mechanisms were responsible for this phenomenon:

- Particles are assembled by convective liquid flow, driven by evaporation of the liquid at the contact line.
- Particles are packed by long-range attractive forces, driven by surface tension of the thin liquid film. The lateral capillary force results from an imbalance in the curvature of the liquid surface due to the protruding particles.

Together, these two mechanisms produce the phenomenon of convective-capillary assembly as illustrated in Figure 4-4.

When the goal is to produce a thin film of colloids with poly-crystalline order, then convective-capillary assembly is a fast and convenient technique [76]. Application of the convective-capillary assembly technique has taken various forms that include placing a substrate in a tilted beaker full of solution and allowing the solvent to evaporate [77]; placing a droplet of a nanoparticle suspension on a substrate and allowing the drop

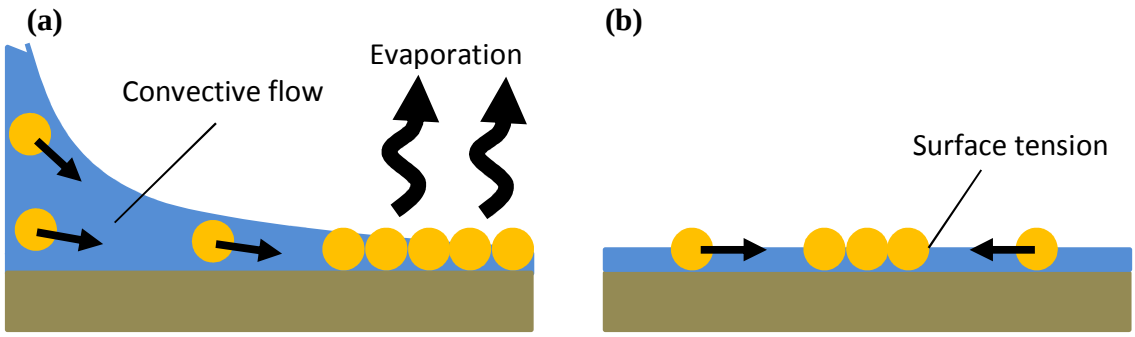

Figure 4-4: Illustration of convective-capillary assembly process. (a) Particles are carried from the meniscus area toward the array boundary by convective flow. Water is removed by evaporation at the array, leaving dried particles. (b) The attractive interaction of the lateral capillary force between protruding particles in a liquid film results in movement. Surface tension in the deformed water surface produces the 2D attractive force.

to dry (the familiar “coffee ring effect”) [78], [79]; placing a droplet of a nanoparticle suspension on a substrate with a retaining ring or other boundary to modify the shape of the drop and allowing the liquid to evaporate [80], [81]; and dip-coating and variations on the Langmuir-Blodgett technique, wherein a substrate is withdrawn from a liquid reservoir or a liquid reservoir is swept over a substrate (e.g. using a straightedge knife to squeegee a large drop of liquid over a stationary sample) [74], [76], [82].

Several in-depth overviews on the subject of convective-capillary assembly, including rigorous theoretical modeling of the various forces at play, have been published [73], [83–85]. Related is fundamental work on wetting of solid surfaces and the shape of the interface at the contact line [1], [72]. A wide assortment of techniques, applications, and demonstrations of convective-capillary assembly has been reported. Briefly, Yamaki, Higo and Nagayama reported on size-dependent separation of nanoparticles based on the fact that larger particles experience the lateral capillary force (immersion force) first [74]. Chen et al. reported on increased deposition/drying rates using a straight-edge to restrict the meniscus of liquid at the drying front and suggested that an increased evaporation rate yields an increased colloidal film growth rate [76]. Malaquin et al. assembled crystalline films using convective flow of nanoparticles and produced sparse arrays of complex 3-D structures using capillary forces [82]. They cited hydrodynamic drag as key to the assembly process and claimed that particle motion is dominated by flows associated with evaporation of the liquid. They also stated that modification of substrate temperature provides a convenient way to control the evaporation rate. Zhao et al. used the “coffee ring effect” to deposit PbS nanocrystals and emphasized the importance of controlling the

solvent evaporation rate as it is responsible for self-assembly [78]. In their experiments, Zhao et al. found that the assembly process resulting from rapid solvent evaporation at elevated temperature (40°C) produced disordered structures, while slow evaporations rates at room temperature produced both ordered and disordered structures. Ye et al. used patterned substrates to break symmetries of the lateral capillary forces and increased the complexity of the resultant structures [86].

Section 4.3: Particles at the Contact Line

As mentioned in Section 4.1, the gold nanorods (20 nm x 40 nm) that were introduced into the nanoaquarium as part of the original solution were mostly displaced to the perimeter of the imaging window when the bubble formed. While examining this

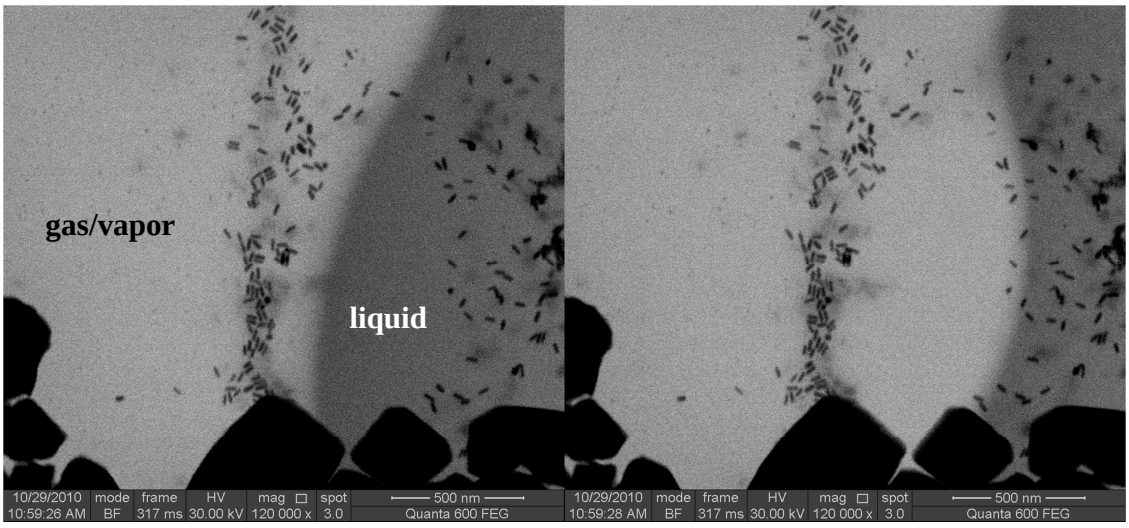

Figure 4-5: Gold nanorods ejected from a receding liquid front are deposited onto the surface of the window that contains the gas/vapor bubble. Two seconds elapse between images. The large dark objects at the bottom of the images are deposits from the potassium hydroxide etch that formed the suspended membranes (Figure 2-2(i)). They are on the outside of the channel and do not interact with the particles, though they do affect the electron beam passing through the sample.

region of the window, the interface between the “bulk” liquid and the gas/vapor region appeared to be unstable under irradiation of the electron beam, sometimes advancing, sometimes receding, and sometimes oscillating. Often when the interface receded, nanorods were ejected from the “bulk” liquid into the liquid thin film of the gas/vapor region (see Figure 4-5, Figure 4-6, and Figure 4-7).

The observations are consistent with the description for convective-capillary assembly given in Section 4.2, namely that particles are convected out from the bulk liquid to the thin liquid film and then pack together as a result of their capillary interaction in the thin film region. The significance of the role that convection plays is illustrated in Figure 4-6. As the contact line recedes, particles pushed out of the “bulk” liquid into the thin liquid film are the ones that experience the most significant motion.

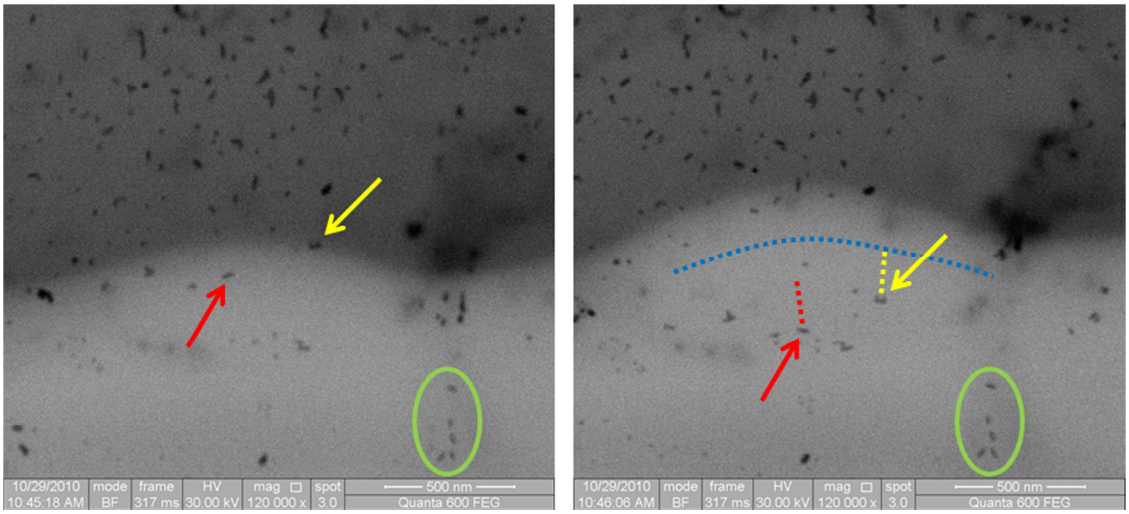

Figure 4-6: Particles ejected from a receding contact line. 48 seconds elapse between frames. The same particle in the left and right images are marked with the same color arrow and the particle’s trajectory is indicated with a dashed line. Note that the particles most recently ejected from the receding contact line experience the most significant motion, while the particles located further from the contact line experience minimal motion (green circle). The former location of the contact line is indicated by blue line on the right image.

And this motion takes place in the thin film region of the system. The particles in Figure 4-6 reached instantaneous velocities on the order of hundreds of nm/s, e.g., approximately 200 nm/s and 525 nm/s for the red and yellow indicators, respectively. The concentration of particles in this image is not very high, and thus we were able to track the "long range" motion of the ejected particles. However, one could imagine that in the highly concentrated regime, an ejected particle would not be able to travel far before coming into contact with already deposited particles, at which point capillary and intermolecular forces would dictate the orientation and packing of the new particle. In this case, the convection of particles would be an effective mechanism for packing the particles together.

An interesting observation was made regarding the motion of particles at the contact line. The moment at which a particle was propelled into the thin film region was generally not concurrent with the moment that the contact line passed over the particle (contact line here refers to the interface between dark and light background in Figure 4-5, Figure 4-6, and Figure 4-7). In most cases, the contact line passed over the particle and it wasn't until the contact line had receded past the particle by some distance (10s of nm) that the particle shot forward. For example, note the red arrow particle in Figure 4-7. The red arrow particle starts out in the "bulk" liquid. The contact line passes over the particle and the particle hardly moves (though it does rotate to be parallel to the contact line). Shortly thereafter, as the contact line continues to recede, the particle is displaced and moves out into the thin film region.

Figure 4-7: Gold nanorods aggregate on a surface as they are ejected from a receding liquid contact line. The dark region moving upward in the three images is the receding liquid. The same particle is indicated by a red arrow in each frame. 50 seconds elapse between frames. Note how the particle of interest does not move from its position on the surface until the contact line has passed over it by some distance.

Another interesting effect was observed regarding particles at the moving contact line. During the experiment, the contact line frequently oscillated while being imaged. The contact line would surge and recede, giving the appearance of ocean waves. During the recede part of the cycle, nanorods were deposited on the membrane surface. In some cases when the nanorod concentration was high enough, the ejected nanorods aggregated (Figure 4-7). When the nanorod concentration was sufficiently low, individual nanorods simply came to rest after being ejected. During the surge part of the cycle, the liquid front moved forward, approaching the location of the previously deposited nanorods. Upon reaching a nanorod on the membrane surface, one might expect the liquid front to engulf the nanorod, resuspending the nanorod in the liquid. But this was not observed. Instead, the surging liquid front consistently pushed the nanorod away, often rotating the nanorod to align it parallel with the contact line. Examples are shown in Figure 4-8 and Figure 4-9. The advancing contact line served to advect the nanorods in the thin film. The particles were pushed forward at a speed equal to the rate at which the contact line

advanced. Explanations for this behavior, as well as the delayed particle motion at the contact line mentioned earlier, are discussed in Section 5.2.

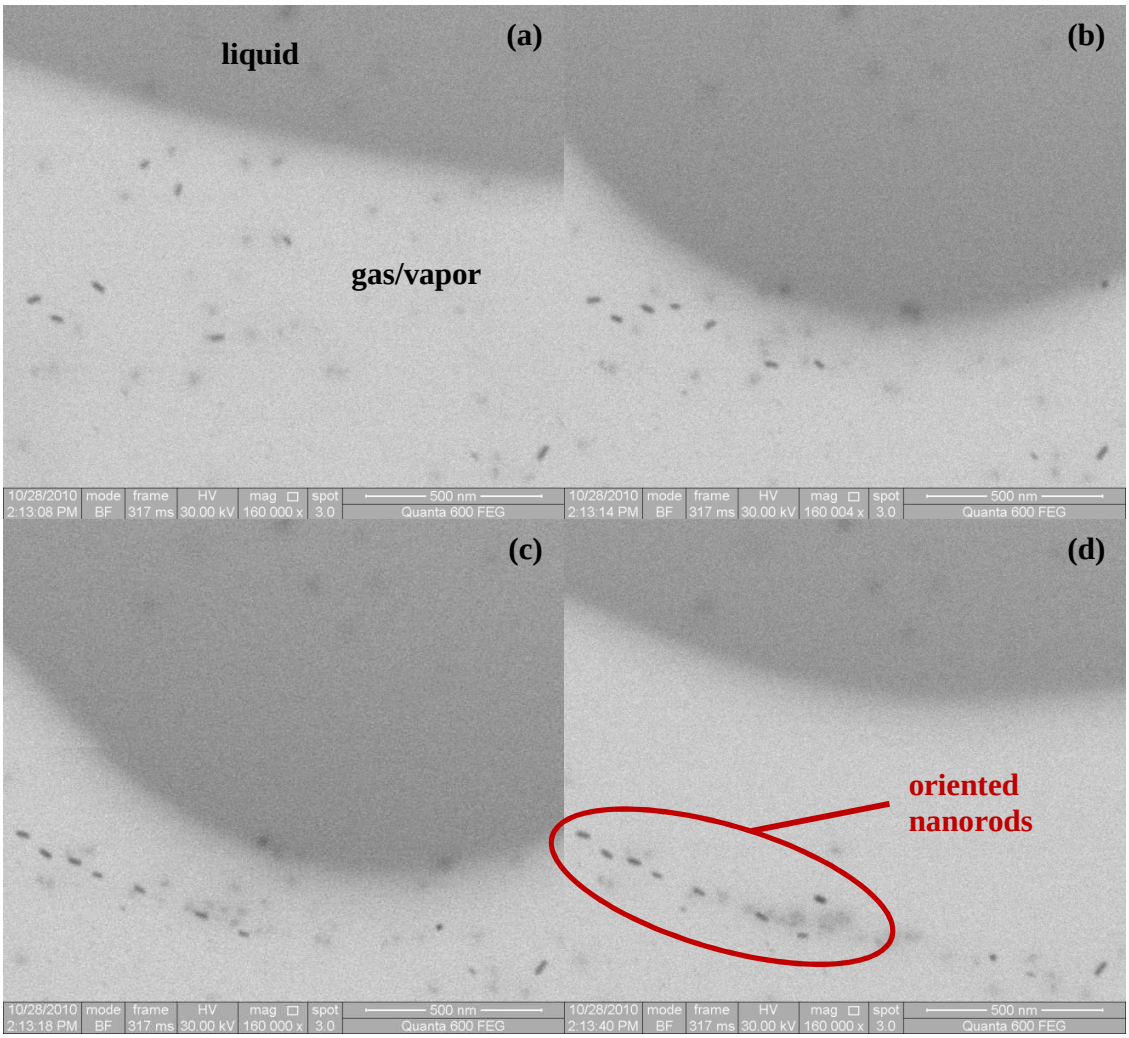

Figure 4-8: Deposition and orientation of gold nanorods under the influence of a cyclic contact line. Note how initially scattered nanorods are pushed into alignment by the advancing contact line.

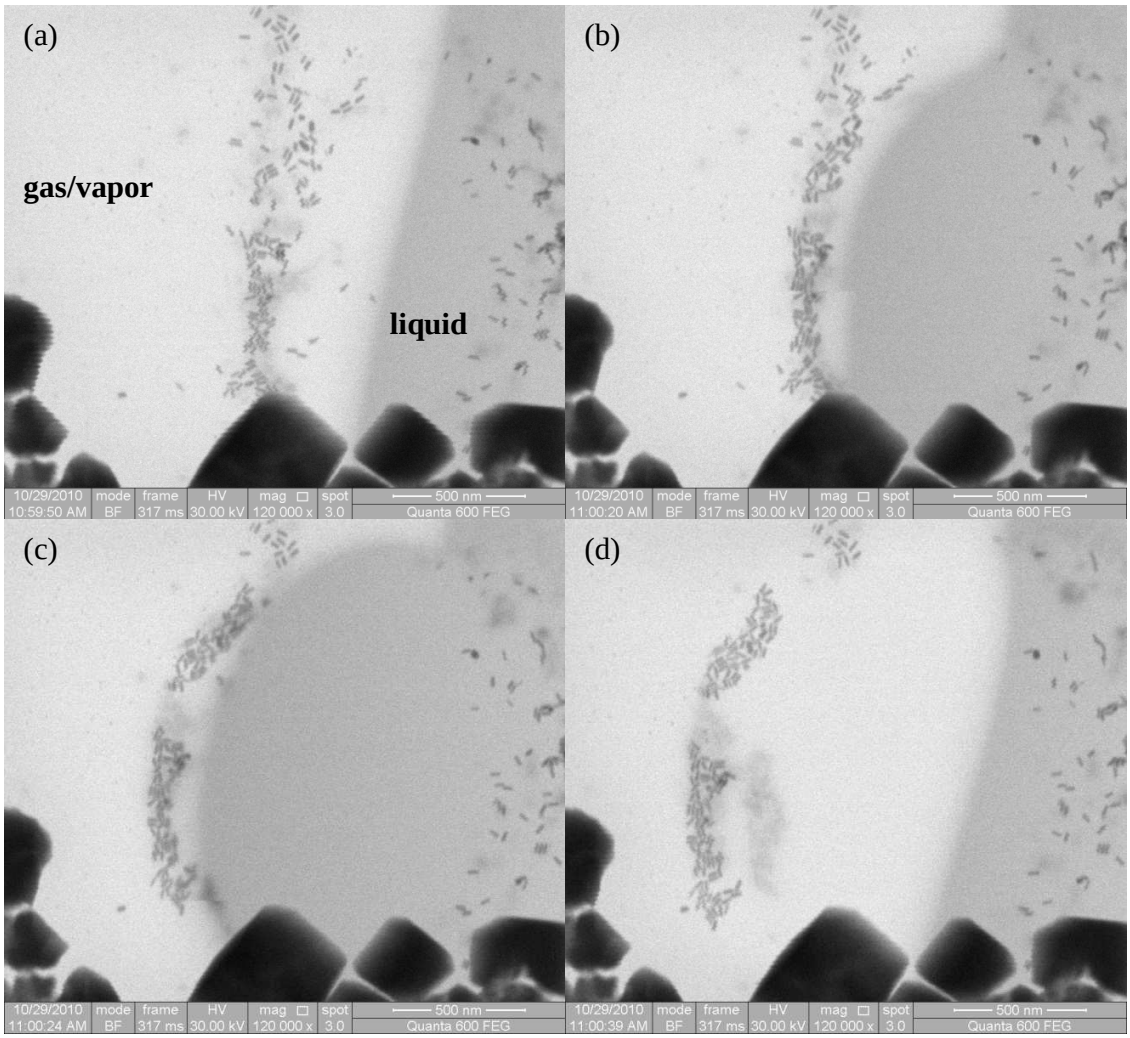

Figure 4-9: Deposition and orientation of gold nanorods under the influence of a cyclic contact line. Note how initially dispersed and loosely packed nanorods are oriented and compacted by the advancing contact line.

Section 4.4: Assembly in an Evaporating Thin Film of Liquid

Particles in the gas/vapor region of the imaging window resided in a thin film of liquid. Particles were driven to aggregate by zooming in on a region of interest and allowing the electron beam to raster across the sample while recording the image. A series of images of aggregating particles is pictured in Figure 4-10. Once the particles in a

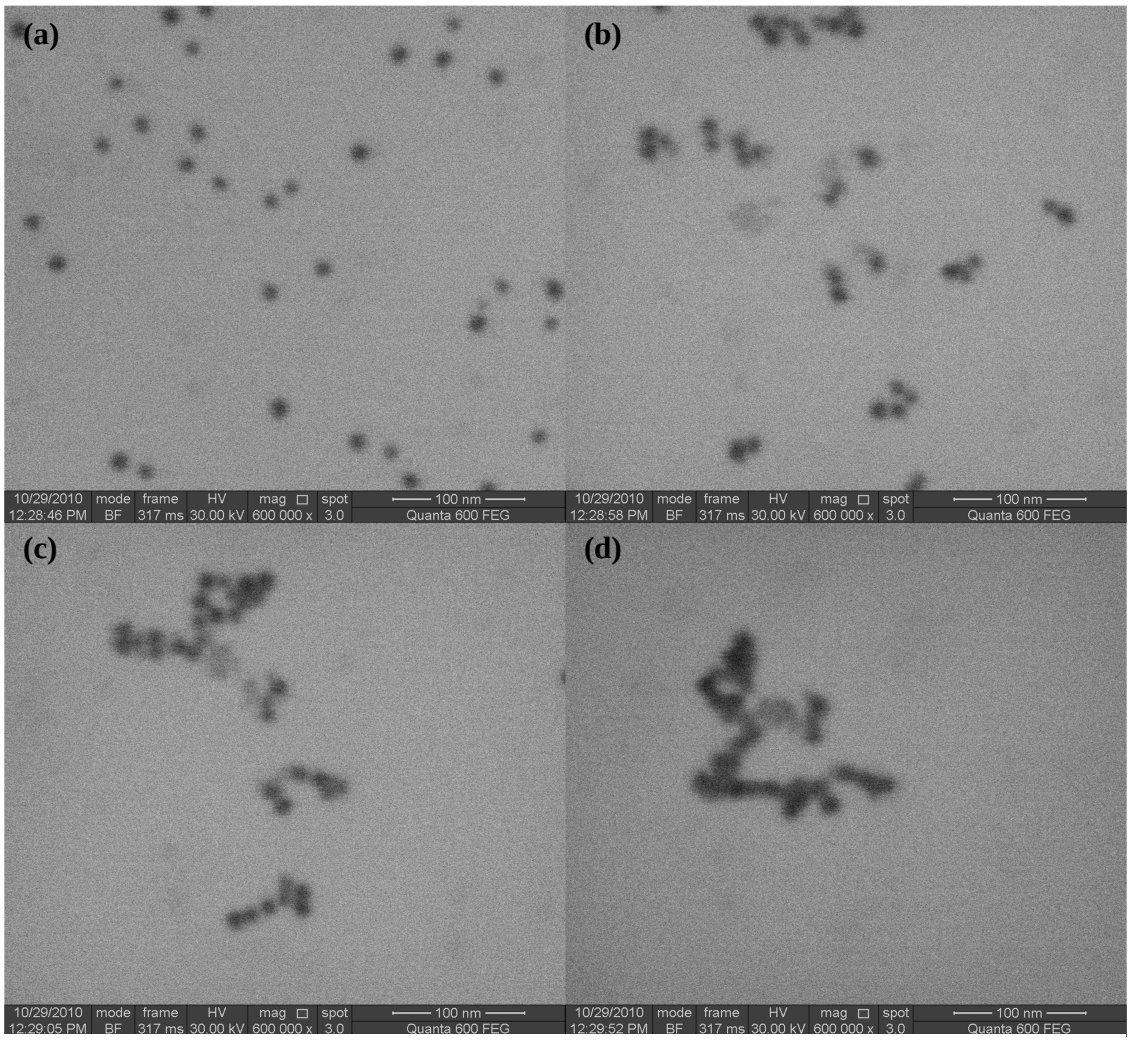

Figure 4-10: (a) – (d) A series of images of nanoparticles aggregating on the silicon nitride membrane surface in an evaporating thin film of liquid. Timestamp in HH:MM:SS reads (a) 12:28:46, (b) 12:28:58, (c) 12:29:05, (d) 12:29:52.

region finished aggregating, or the aggregation stalled, the imaging area was zoomed out, relocated to a different site of the imaging window, and zoomed back in to drive another aggregation process. The level of zoom/magnification remained fixed during any particular aggregation process, but was varied from process to process. Zoom/magnification was the "knob" that controlled this experiment.

The rate and extent of aggregation experienced by the particles depended on the level of zoom/magnification, which affected the rate of heating and evaporation. At low magnification, the aggregation occurred slowly and not all of the particles in the field of view participated equally in the aggregation process (particles close to the perimeter moved further and more rapidly than particles near the center). At high magnification the aggregation occurred quickly and nearly all of the particles in the field of view participated in the aggregation process.

Section 4.5: Results and Analysis

Digital recorded video was processed and particle tracking was performed to analyze the motion of particles and evolution of the system described in Section 4.4. Particle and cluster tracking was performed with ImageJ (1.37) and Matlab, using particle tracking code made freely available by Dr. Maria Kilfoil [87]. Details of the image processing and particle tracking are given in Appendix B. Four levels of zoom/magnification were investigated:

- 160,000X magnification, scale bar of 500 nm, 1.56 nm/pixel (1 dataset)
- 240,000X magnification, scale bar of 300 nm, 1.04 nm/pixel (4 datasets)

- 500,000X magnification, scale bar of 100 nm B, 0.50 nm/pixel (2 datasets)
- 600,000X magnification, scale bar of 100 nm A, 0.41 nm/pixel (3 datasets)

Representative images and the tracked particle trajectories from a single dataset at each magnification are shown in Figure 4-11 – Figure 4-14. The particles' positions and trajectories were digitized and stored in data files. Several quantities, discussed in the following paragraphs, were calculated for a particular dataset at a given magnification and the values were averaged with the values from other datasets at the same magnification to produce Figure 4-15 – Figure 4-22.

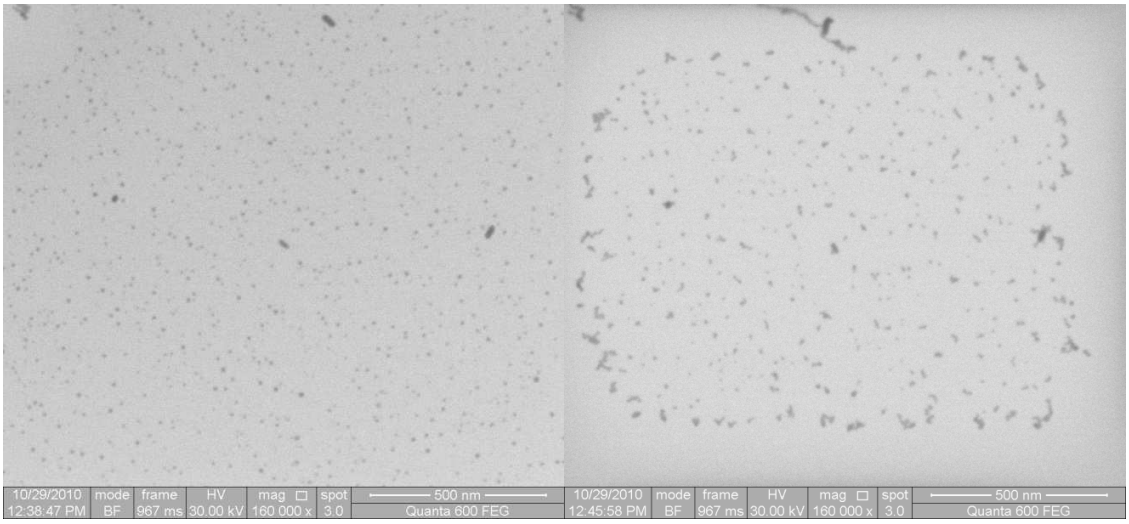

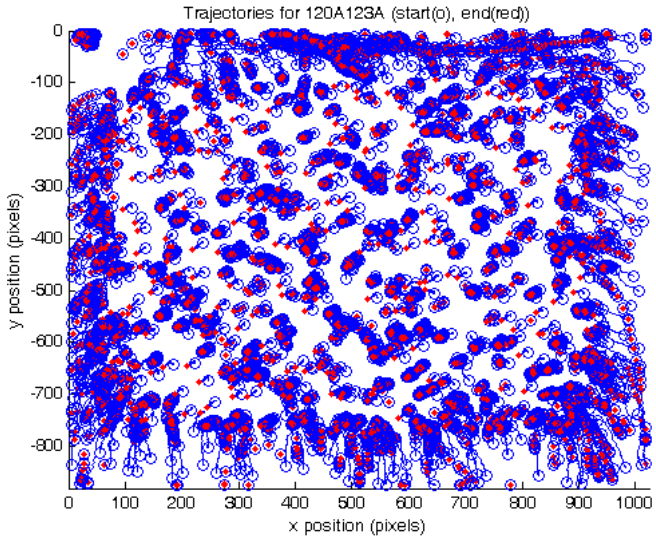

Figure 4-11: First frame (a) and last frame (b) for one dataset at 160,000X magnification. (c) Particle tracking results showing particle trajectories. Initial positions are marked with a hollow circle and final positions are marked with solid red dots.

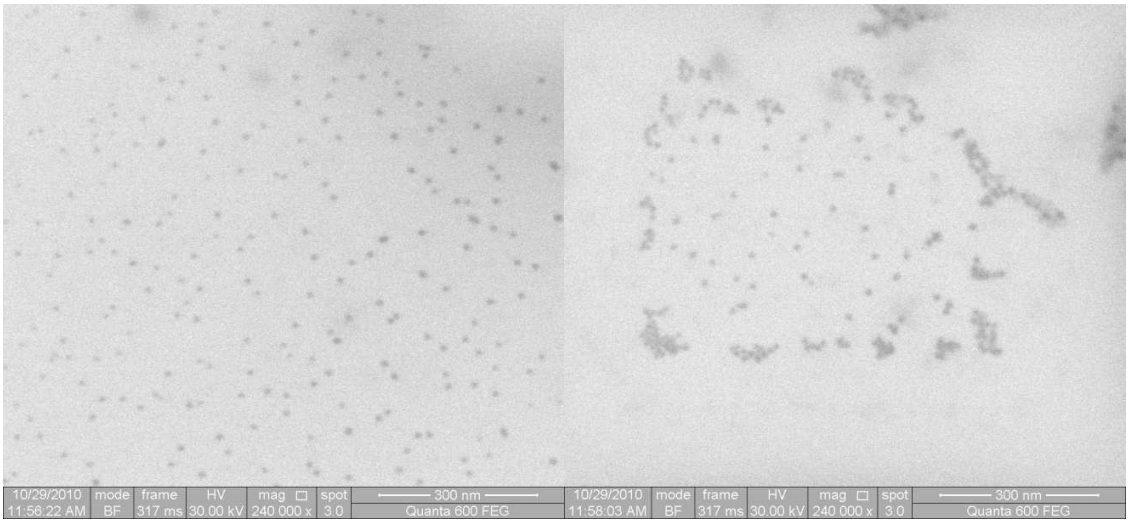

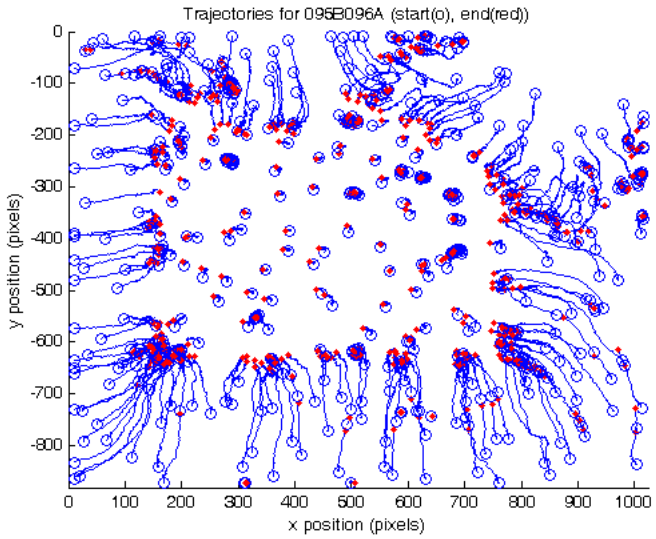

Figure 4-12: First frame (a) and last frame (b) for one dataset at 240,000X magnification. (c) Particle tracking results showing particle trajectories. Initial positions are marked with a hollow circle and final positions are marked with solid red dots.

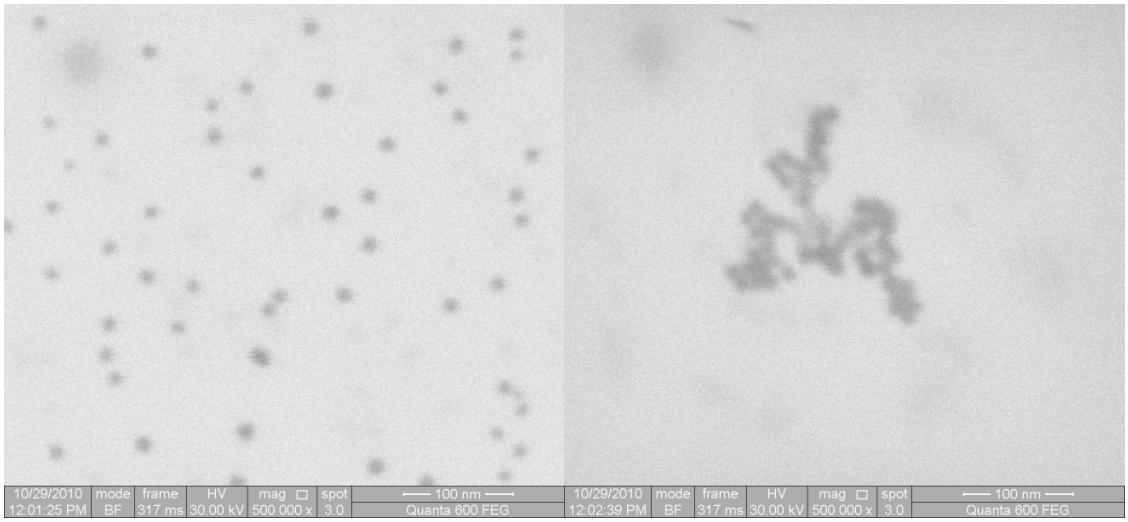

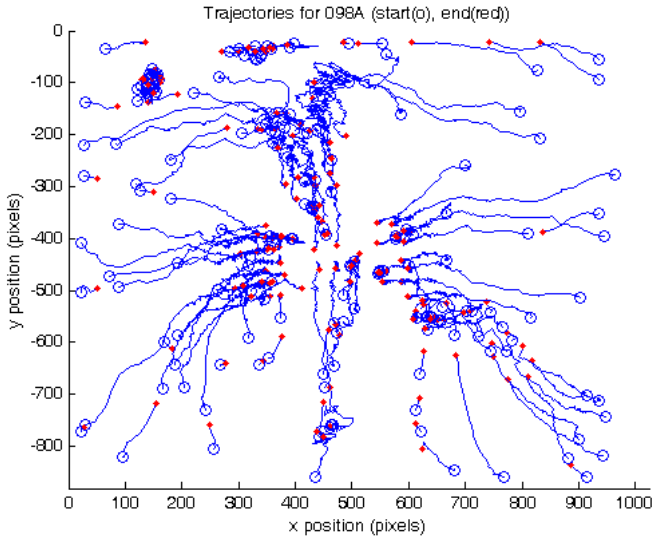

Figure 4-13: First frame (a) and last frame (b) for one dataset at 500,000X magnification. (c) Particle tracking results showing particle trajectories. Initial positions are marked with a hollow circle and final positions are marked with solid red dots.

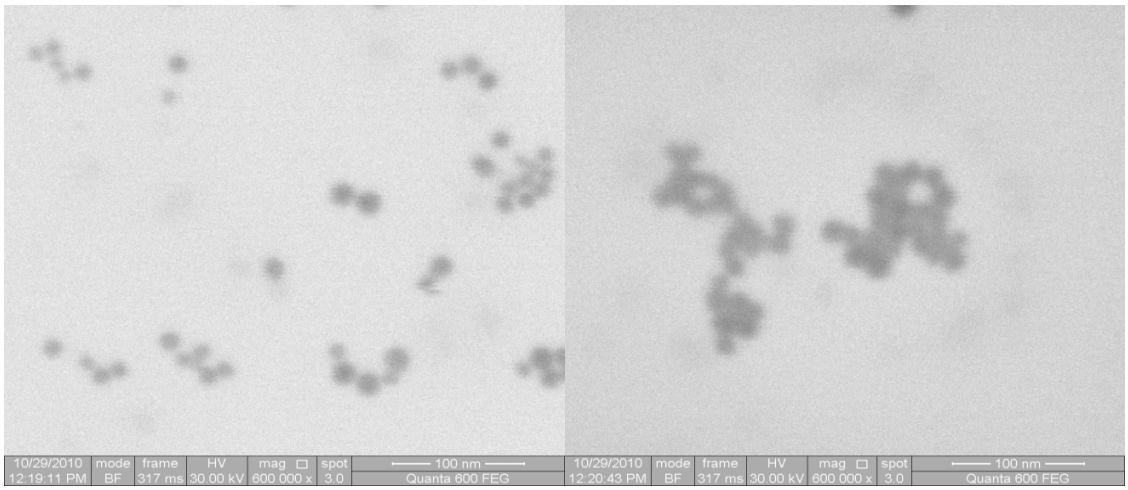

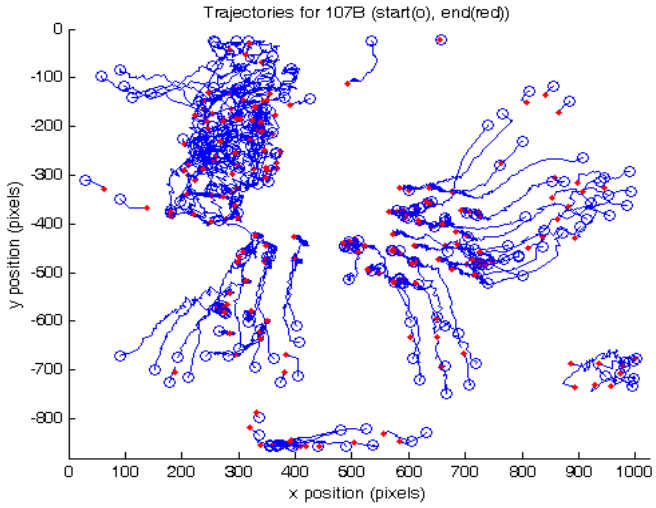

Figure 4-14: First frame (a) and last frame (b) for one dataset at 600,000X magnification. (c) Particle tracking results showing particle trajectories. Initial positions are marked with a hollow circle and final positions are marked with solid red dots.

The normalized mean distance between particles as a function of time for various magnifications is given in Figure 4-15 (the left image depicts data for the time interval 0<t<140s and the right image depicts data for the time interval 0<t<400s). The mean distance was normalized with the diagonal length of the imaged area. This normalization was necessary to enable comparison of data obtained at different magnifications. The mean distance was calculated from the particle position information in each frame. Details of this calculation, including an explanation of the choice of image diagonal as the normalization factor, are given in Appendix C. Briefly, consider N particles in a frame. We select particle i and calculate the distance d_{ij} between it and the other $N-1$ particles, and then determine the average distance between the i^{th} particle and all the other particles, i.e. $\bar{d}_i = \frac{1}{N-1}\sum_{j=1}^{N} d_{ij}$. The same calculation was repeated for all N particles in the frame, and averaged to give the mean distance between all particles for that frame, defined as $\bar{d} = \frac{1}{N}\sum_{i=1}^{N} \bar{d}_i$. The mean distance between particles gives a measure of the aggregation state of the system. As individual particles aggregate and

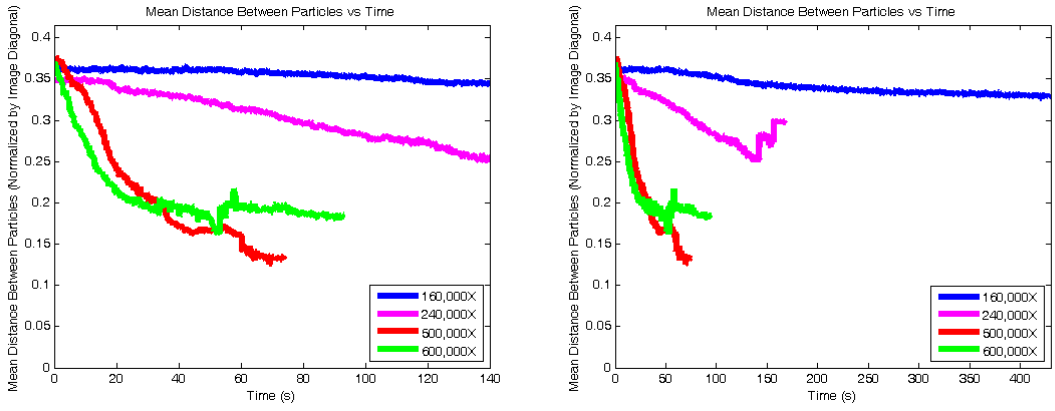

Figure 4-15: Mean distance between particles $\bar{d}$, normalized by the length of the image diagonal, versus time for four different magnifications. L and R image show two different time ranges.

form clusters, the mean distance between particles decreases. Note that the rate of aggregation increases for increased magnification. The plotted values in Figure 4-15 represent the averaged value at a given magnification (1 dataset at 160,000X, 4 datasets at 240,000X, 2 datasets at 500,000X, 3 datasets at 600,000X). For each magnification, the plots become erratic towards the end because datasets of the same magnification lasted for different amounts of time and when a dataset runs out of values it produces a sharp step in the plotted (averaged) value (e.g., two datasets are being averaged until the first dataset runs out of values and the plotted value jumps to the value of the second dataset only).

The normalized mean cluster size, measured by the number of individual particles in a cluster, as a function of time for various magnifications is depicted in Figure 4-16 (the left image depicts data for the time interval 0<t<140s and the right image depicts data for the time interval 0<t<400s). Mean cluster size was calculated by thresholding the image in ImageJ to produce a binary image where aggregates containing multiple

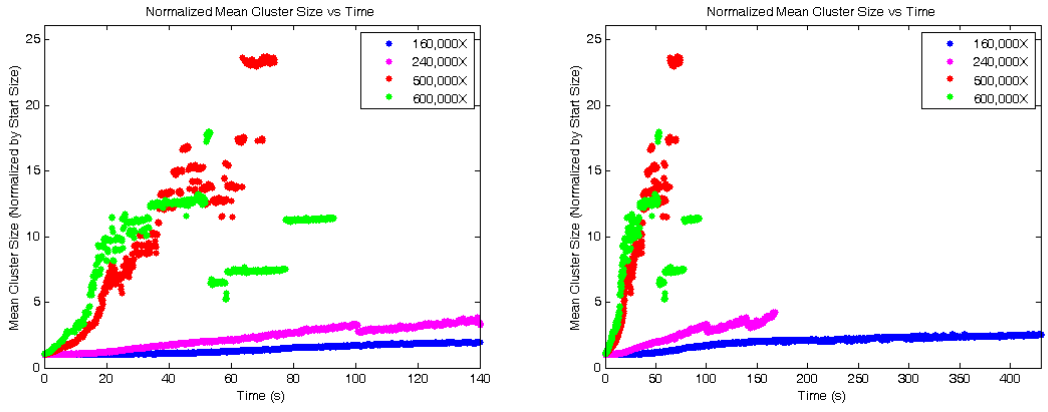

Figure 4-16: Normalized mean cluster size versus time for four different magnifications. L and R image show two different time ranges.

individual particles became a single entity. Details are given in Appendix B. Mean cluster size was normalized with the initial mean cluster size at the start of observation. Erratic behavior at the end of each plot is due to differences in duration for the datasets, as well as variability in thresholding the grayscale images (e.g. sometimes a large cluster would oscillate between recognition as a single cluster and two separate clusters).

The normalized cluster concentration (count/area), measured by the number of clusters in the field of view, as a function of time for various magnifications is given in Figure 4-17 (the left image depicts data for the time interval 0<t<140s and the right image depicts data for the time interval 0<t<400s). Cluster count was calculated by thresholding the image in ImageJ to produce a binary image where aggregates that contained multiple individual particles became a single entity. Details are given in Appendix B. Cluster count was normalized with the initial cluster count at the start of observation. Erratic behavior at the end of each plot is due to differences in duration for the datasets, as well as variability in thresholding the grayscale images.

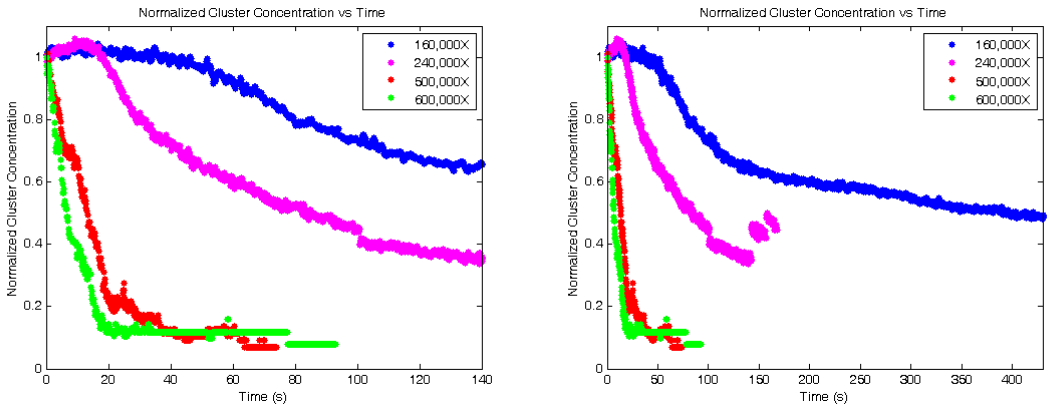

Figure 4-17: Normalized cluster concentration (count/area) versus time for four different magnifications. L and R image show two different time ranges.

Particle speed was calculated by measuring the displacement of a particle from one frame to the next and dividing by the time that elapsed between the frames. Due to an unsynchronized frame rate issue that resulted in oversampled images, the speed calculation was not straightforward. Details of the frame rate and speed calculation are given in Appendix B. The speed for all of the particles in a frame was calculated and averaged to give Figure 4-18 and Figure 4-19. Figure 4-18 depicts the mean particle speed as a function of time for magnifications of 160,000X (a), 240,000X (b), 500,000X

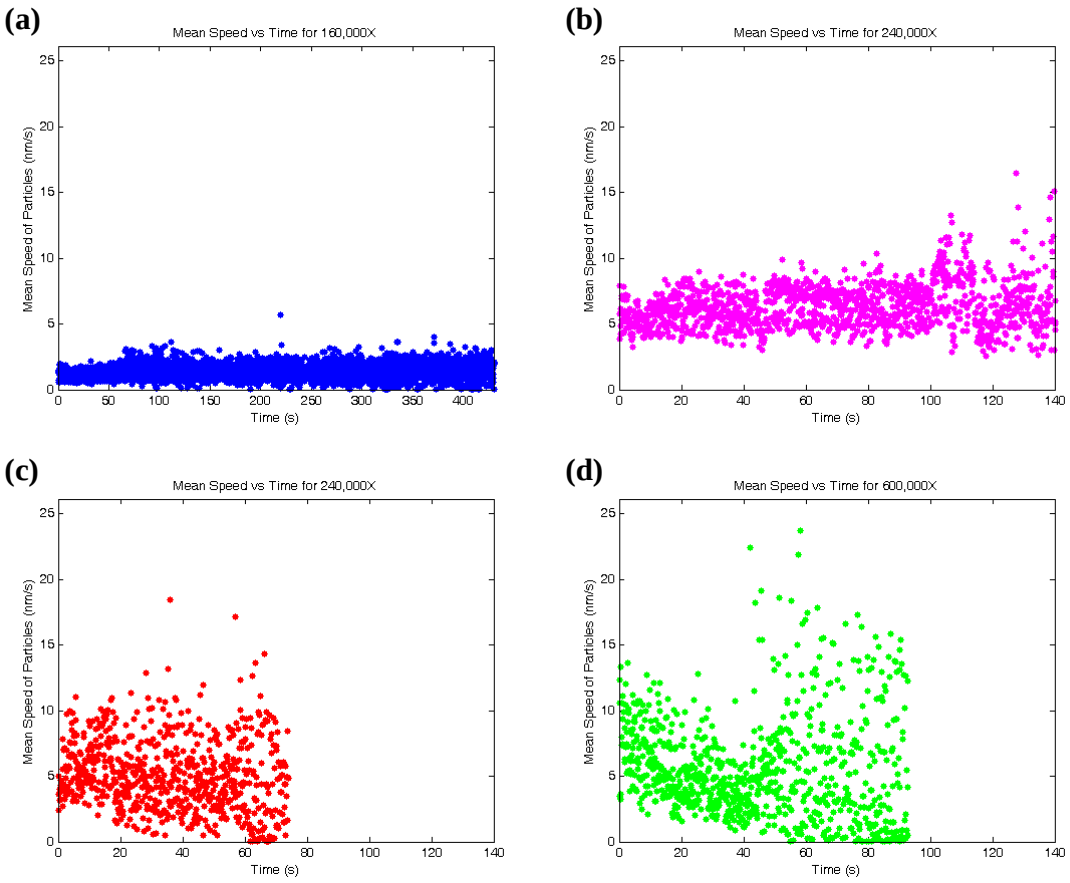

Figure 4-18: Mean speed of all the particles in the field of view versus time for all datasets at four different magnifications. (a) 120,000X. (b) 240,000X. (c) 500,000X. (d) 600,000X.

(c), 600,000X (d). Time starts at the beginning of the aggregation process. Figure 4-19 depicts the mean particle speed as a function of the mean distance between particles for magnifications of 160,000X (a), 240,000X (b), 500,000X (c), 600,000X (d).

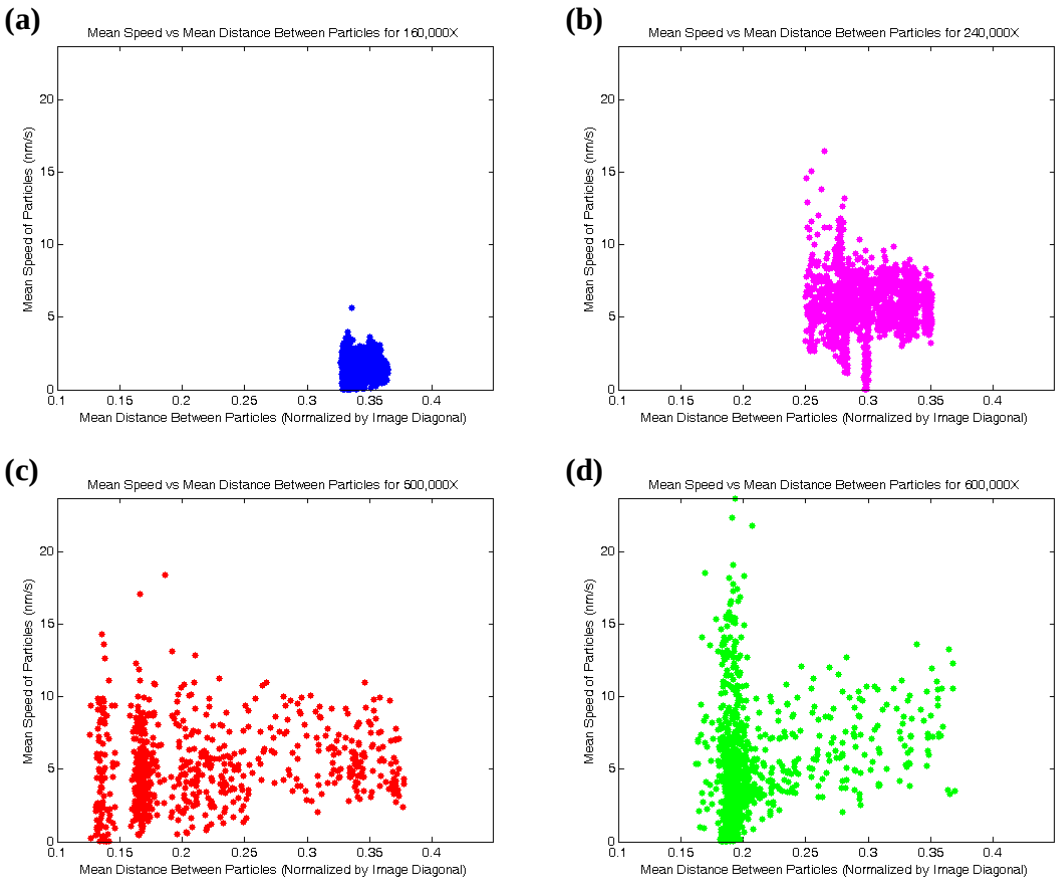

Figure 4-19: Mean speed of all the particles in the field of view as a function of the mean distance between all the particles in the field of view for all datasets at four different magnifications. (a) 120,000X. (b) 240,000X. (c) 500,000X. (d) 600,000X.

Spatial information about speed is important as well. For example, it would be useful to know if particles move faster in one region of the imaging window compared to other regions. A coordinate system was selected to represent the radial position of a particle from the center of the image. The coordinate system was designed to take into

account the fact that the electron beam illuminates a rectangular region. Based on the particles' trajectories in Figure 4-11 – Figure 4-14, it is clear that the rectangular footprint of the imaging region affected the aggregation pattern (also a rectangle) and the relationship between image geometry (heating region geometry) and particle position had to be considered. Details of the radial box coordinate system are given in Appendix D. Figure 4-20 depicts particle speed as a function of radial box position from the center of the image. The plots show speed measurements for the entire duration of all datasets. If a radial position had multiple speed values because multiple particles passed through the

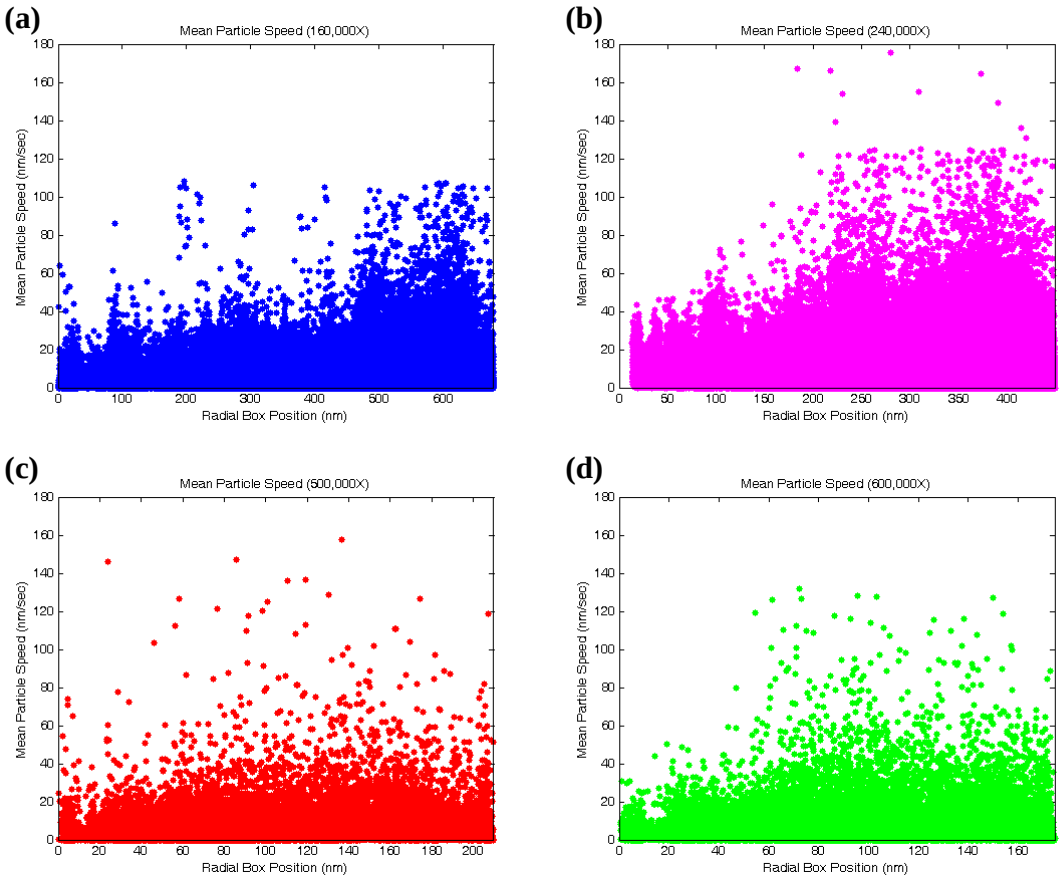

Figure 4-20: Particle speed as a function of radial box position for all datasets at four different magnifications. (a) 120,000X. (b) 240,000X. (c) 500,000X. (d) 600,000X.

same radial position at different times, then the speed values were averaged for that position.

To soften the impact of outliers in Figure 4-20, the radial position was divided into bins of length 5 pixels (i.e. $0px \leq bin_1 < 5px$, $5px \leq bin_2 < 10px$, $10px \leq bin_3 < 15px$, etc) and the speed values in each bin were averaged. Figure 4-21 depicts the binned and averaged particle speed as a function of radial box position from the center of the image. Lastly, the speed data was processed in the same manner of binning and

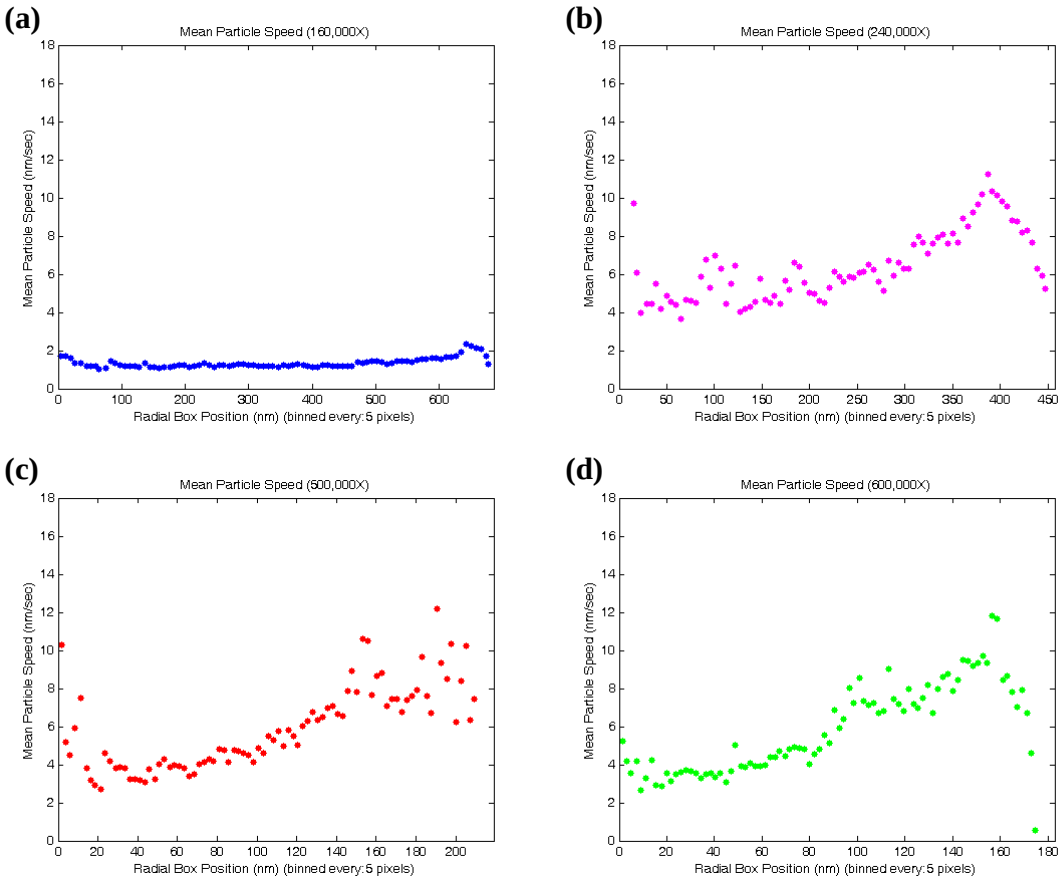

Figure 4-21: Binned and Averaged particle speed as a function of radial box position for all datasets at four different magnifications. (a) 120,000X. (b) 240,000X. (c) 500,000X. (d) 600,000X. Radial box position was partitioned into bins, 5 pixels long, and the speed values in each bin were averaged.

averaging, except particles with zero speed were considered stuck to the membrane and excluded from the calculation. Figure 4-22 depicts the binned, averaged, non-zero speed as a function of radial box position from the center of the image.

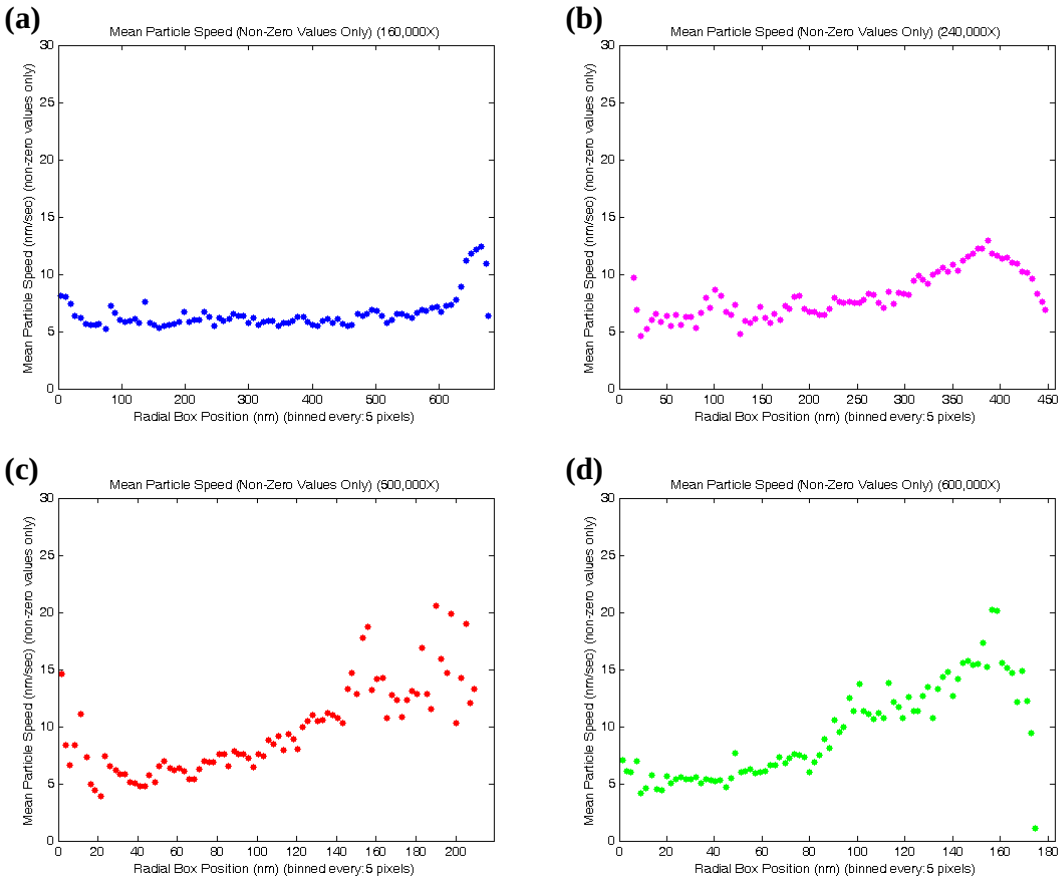

Figure 4-22: Binned and averaged non-zero particle speed as a function of radial box position for all datasets at four different magnifications. (a) 120,000X. (b) 240,000X. (c) 500,000X. (d) 600,000X. Radial box position was partitioned into bins, 5 pixels long, and the speed values in each bin were averaged. Only non-zero speeds were considered in the calculation.

Chapter 5: The Effect of Evaporation on Fluid Flow in a Thin Liquid Film and Consideration of Other Effects.

In Chapter 4, we imaged the motion and aggregation of nanoparticles resulting from motion of the "contact line" and evaporation of a liquid film. As discussed in Section 4.3, nanoparticles interacting with a receding contact line were propelled into the thin film region, although often with a delay between when the contact line passed over the particle and when the particle moved. Additionally, an advancing contact line was seen to push particles away, rather than engulf particles. As discussed in Section 4.4, particles in an evaporating thin film of liquid aggregated. The kinetics and extent of aggregation was dependent on the magnification of the image in the electron microscope. In this chapter, we will estimate the various forces acting on the nanoparticles and characterize how these forces change in response to key parameters in order to obtain a deeper understanding of the process. Insight gained from the investigation can be used to design processes and systems based on convective-capillary assembly with desired outcomes. Suggestions for novel nanoparticle self-assembly techniques are presented at the end.

Section 5.1: Background and Fundamentals of Relevant Phenomena

5.1.1: Pressure in a Liquid Thin Film

Disjoining Pressure

The self-leveling nature of a free-flowing liquid in response to a potential field should be familiar and intuitive to most. On the macro scale, the dominant potential field is gravitational potential energy ($m\ g\ h$). For example, imagine a tank of water with a

partition in the middle that separates two different volumes, one of which is larger, and thus higher, than the other (Figure 5-1). Upon removal of the divider, water will flow from the tall section to the short section in order to minimize the gravitational potential energy of the system. Flow is driven by a spatial variation in the hydrostatic pressure of the water ($\rho\ g\ h$) due to the variation in water height, giving rise to a lateral pressure gradient (dP/dx).

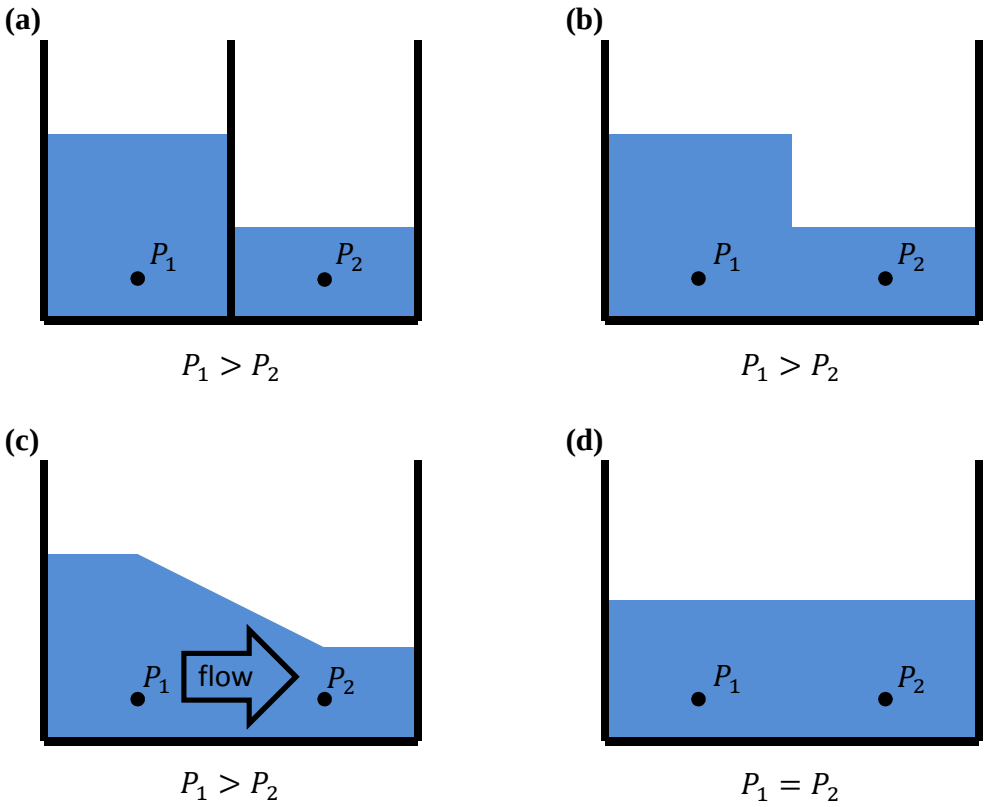

Figure 5-1: Equilibration of liquid height on the macro-scale in order to minimize gravitational potential energy. (a) A tank with a divider separates two volumes of water. The hydrostatic pressure in the taller volume of liquid is greater than in the shorter volume of liquid. (b) The divider is removed. (c) Water flows from the higher pressure region to the lower pressure region. (d) Flow ceases when the liquid height is constant. There is no longer any lateral pressure gradients to drive flow. Gravitational potential energy of the system is minimized.

Similarly, there is an analogous process that takes place on the nanoscale, except that instead of gravitational potential energy, it is intermolecular interaction energy (i.e., Van der Waals force) that drives the process. We define the Van der Waals interaction potential between molecules as

$$w_{mm}(r) = -\frac{C}{r^n}, \tag{5-1}$$

and corresponding force as

$$f_{mm}(r) = -\frac{dw}{dr} = -\frac{n\,C}{r^{n+1}}, \tag{5-2}$$

where r is the center to center separation distance between molecules, $n = 6$ for Van der Waals interaction, and C is the London dispersion force constant ($\sim 10^{-77} J\,m^6$ for many commonly encountered materials) [88]. When $C > 0$, the force is attractive, and when $C < 0$, the force is repulsive. An interaction potential of this form is appropriate for describing the attractive interaction of a water molecule with a wetting surface (e.g. silicon oxide, silicon nitride, etc); however, one could capture more complicated interactions between molecules by writing the interaction potential in a more general form:

$$w_{mm}(r) = -\frac{A}{r^n} + \frac{B}{r^m} + \cdots \tag{5-3}$$

and including additional terms such as Coulombic interactions between charged molecules, dipole interactions between polarizable molecules, the interaction of a water molecule with a hydrophobic surface, or other interactions of interest. As detailed in "Intermolecular and Surface Forces" [88], equations (5-1) and (5-2) are used to calculate

the interaction potential (w_{mp}) and corresponding force (f_{mp}) between a molecule and a plate of thickness T_1 and molecular number density ρ_1, separated by distance, D (see Figure 5-2):

$$w_{mp}(D, T_1) = -\frac{\pi\, C\, \rho_1}{6}\left(\frac{1}{D^3} - \frac{1}{(D+T_1)^3}\right) \tag{5-4}$$

$$f_{mp}(D, T_1) = -\frac{\pi\, C\, \rho_1}{2}\left(\frac{1}{D^4} - \frac{1}{(D+T_1)^4}\right). \tag{5-5}$$

As a reference for the strength of this interaction, we can compare w_{mp} for a single water molecule to thermal energy, $k_B\, T$. A water molecule in direct contact with a silicon nitride surface will have a separation distance of about $D \sim 0.45$ nm (radius of water molecule $= 0.193$ nm, radius of silicon nitride molecule $= 0.253$ nm), the thickness of the silicon nitride membrane (plate 1) is $T_1 = 50$ nm, and the number density of silicon nitride is $\rho_1 = 1.48 \times 10^{28}/\mathrm{m}^3$, which at 30 °C yields $w_{mp}(0.45\ \mathrm{nm}, 50\ \mathrm{nm})/k_B\, T \approx 0.2$ (30 °C was selected as a modest temperature rise due to heating from the beam).

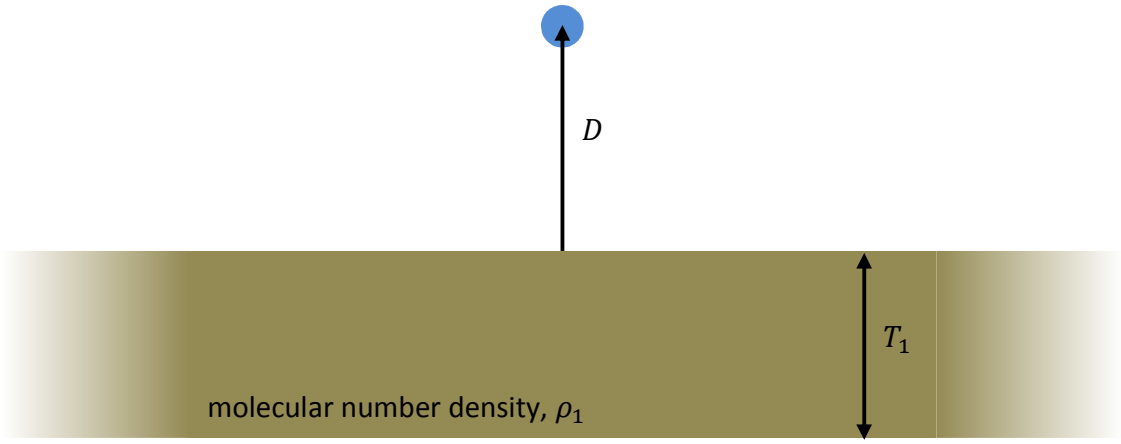

Figure 5-2: Schematic illustration of relevant geometric parameters for a molecule and a plate with Van der Waals interaction. The plate is of thickness T_1, molecular number density ρ_1, and separated by distance D.

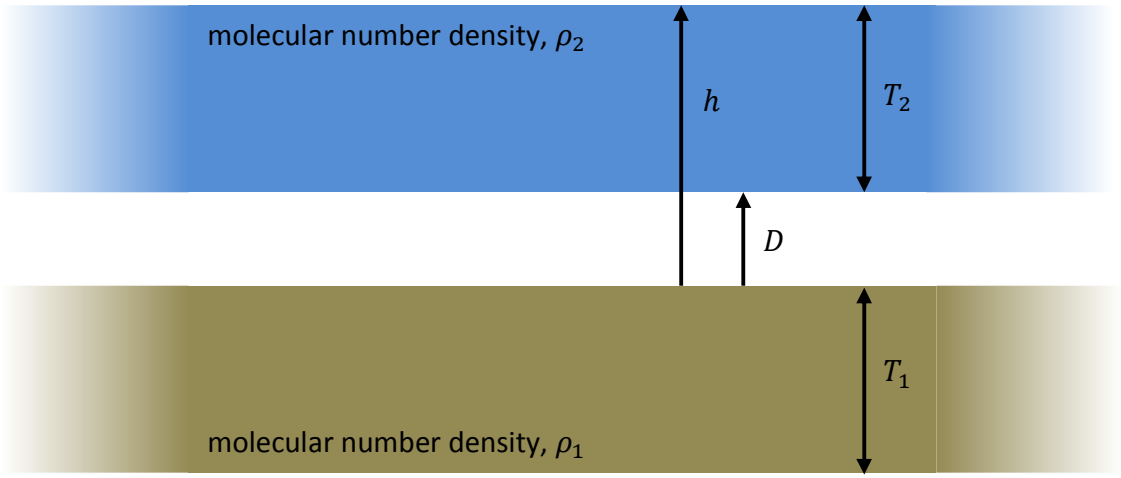

Figure 5-3: Schematic illustration of relevant geometric parameters for two plates with Van der Waals interaction. Each plate is of thickness T_i, molecular number density ρ_i, and separated by distance D. If we consider plate 2 to be a liquid film, then the separation, D, would be given by the sum of one molecular radius from each material. It is helpful to define the film height, $h = D + T_2$.

Moving out by a single water molecule diameter, this values drops to $w_{mp}(0.83\text{ nm}, 50\text{ nm})/k_B\,T \approx 0.03$, and at another molecule diameter away the value drops to $w_{mp}(1.22\text{ nm}, 50\text{ nm})/k_B\,T \approx 0.01$. From this, one might be tempted to conclude that the Van der Waals interaction is orders of magnitude too small and dies off too quickly to be of any consequence. This is incorrect because when summed over the entirety of the liquid body (film height), the interaction becomes quite significant. The expressions in equations (5-4) and (5-5) are used to obtain the interaction potential and corresponding force between two plates of thickness T_1 and T_2 with molecular number density ρ_1 and ρ_2, separate by distance, D (see Figure 5-3) [88]:

$$w_{pp}(D,T_1,T_2) = -\frac{\pi\, C\, \rho_1\, \rho_2}{12}\left(\frac{1}{D^2} - \frac{1}{(D+T_2)^2} + \frac{1}{(D+T_2+T_1)^2} - \frac{1}{(D+T_1)^2}\right) \tag{5-6}$$

$$f_{pp}(D,T_1,T_2) = -\frac{\pi\, C\, \rho_1\, \rho_2}{6}\left(\frac{1}{D^3} - \frac{1}{(D+T_2)^3} + \frac{1}{(D+T_2+T_1)^3} - \frac{1}{(D+T_1)^3}\right). \tag{5-7}$$

Note that w_{pp} and f_{pp} are normalized per unit area, which means that f_{pp} is actually in units of pressure (i.e., $\mathrm{N/m^2}$, Pa). Supposing that plate 2 is a fluid, the compressive force of the Van der Waals interaction is balanced by pressure in the fluid,

$$P_{VdW}(D,T_1,h) = P_d(D,T_1,h) = -f_{pp}(D,T_1,h) = \frac{\pi\, C\, \rho_1\, \rho_2}{6}\left(\frac{1}{D^3} - \frac{1}{h^3} + \frac{1}{(h+T_1)^3} - \frac{1}{(D+T_1)^3}\right), \tag{5-8}$$

where T_2 has been replaced by h, fluid height, using the relation $h = D + T_2$. The expression in equation (5-8) is analogous to gravitational hydrostatic pressure in a fluid, except that on the nanoscale it is Van der Waals hydrostatic pressure. This pressure is well known and referred to as the disjoining pressure P_d (the pressure it takes to separate, or disjoin, the plates), and is considered an important factor in characterizing the wetting properties of a drop on a surface [72], [89], [90]. For a water film height of $h = 50$ nm, the disjoining pressure at the water/nitride interface is $P_d(0.45\text{ nm}, 50\text{ nm}, 50\text{ nm}) \approx 28$ MPa. At a cross section of the water film located at $D = 10$ nm, the disjoining pressure is $P_d(10\text{ nm}, 50\text{ nm}, 50\text{ nm}) \approx 2.5$ kPa. Looking at the pressure difference between two points in cross-sections with film heights h_2 and h_1 yields

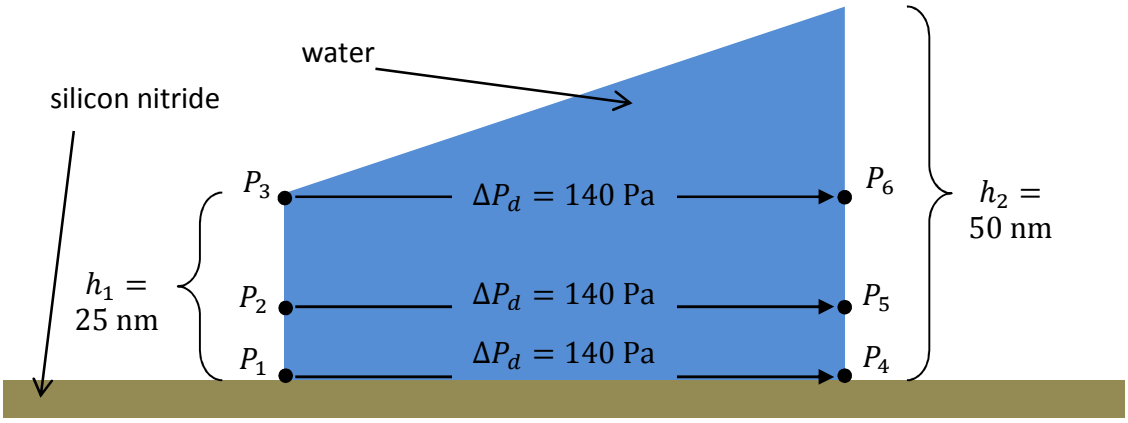

Figure 5-4: Illustration of the pressure difference, ΔP_d, that arises in a thin film of water on a silicon nitride surface due to nanoscale variation in film height and subsequent variation in disjoining pressure. While the magnitude of the pressure varies along the film height ($P_1 > P_2 > P_3$, $P_4 > P_5 > P_6$), the pressure difference between two points located the same distance from the silicon nitride surface is the same, regardless of vertical position ($P_4 - P_1 = P_5 - P_2 = P_6 - P_3$).

$$\Delta P_d(T_1, h_1, h_2) = P_d(D, T_1, h_2) - P_d(D, T_1, h_1)$$
$$= \frac{\pi\, C\, \rho_1\, \rho_2}{6} \left(\frac{1}{{h_1}^3} - \frac{1}{{h_2}^3} + \frac{1}{(h_2 + T_1)^3} - \frac{1}{(h_1 + T_1)^3} \right). \quad (5\text{-}9)$$

Interestingly, the pressure difference in the fluid exists due to the variation in film height, but the vertical position D is not in the expression. Although the magnitude of pressure in the fluid varies with vertical position in the liquid film according to equation (5-8), the lateral pressure difference between two cross-sections is constant throughout the thickness of the film, irrespective of vertical position. For example, the pressure difference between a $h_1 = 25$ nm thick water film and a $h_2 = 50$ nm thick water film is $\Delta P_d(50\text{ nm}, 25\text{ nm}, 50\text{ nm}) \approx 140$ Pa. This value of ΔP_d is the same whether one considers two points located at the water-nitride interface, two points located 10 nm from

the interface, or two points located 25 nm from the interface (see illustration in Figure 5-4). Considering that h is a function of x, we can write

$$\frac{dP_d}{dx} = \frac{\pi\, C\, \rho_1\, \rho_2}{2} \left(\frac{1}{h^4} - \frac{1}{(h+T_1)^4}\right) h_x, \tag{5-10}$$

where subscript x denotes a derivative. For simplicity, the disjoining pressure gradient can be written as

$$\frac{dP_d}{dx} = \frac{\pi\, C\, \rho_1\, \rho_2}{2} \frac{h_x}{h^4}, \tag{5-11}$$

recognizing that the error in in the disjoining pressure gradient scales as

$$\frac{dP_d}{dx} \text{ error} = \frac{1}{(1+T_1/h)^4 - 1}. \tag{5-12}$$

For a water film that is $h = 50$ nm thick on a silicon nitride surface that is $T_1 = 50$ nm, the error is $\sim 7\%$ and decreases with decreasing h.

Laplace Pressure

Surface tension must also be considered for its effect on pressure in the fluid. It is well known that when a surface separating two immiscible fluids (e.g., a bubble or droplet) is curved, there is a pressure jump across the interface, known as the Laplace pressure, given by

$$\Delta P_{Laplace} = P_{inside} - P_{outside} = \gamma \left(\frac{1}{R_1} + \frac{1}{R_2}\right), \tag{5-13}$$

where γ is surface tension and R_1 and R_2 are the principle radii of curvature. Since we are focusing on one-dimensional analysis, we write

$$\Delta P_{Laplace} = P_{inside} - P_{outside} = \gamma \left(\frac{1}{R_1}\right) = \gamma\, k, \tag{5-14}$$

where k is the curvature of the surface.

Total Pressure

In the experiment considered here, there is a gas/vapor bubble that should be considered the "inside" and a surrounding liquid that should be considered the "outside." In the same manner as Pham et al. [72], we use the small angle (slope) approximation for curvature ($k \approx d^2h/dx^2$), and combine equations (5-8) and (5-14) to write the total pressure in the liquid as

$$P_{liquid} = P_{bubble} - \gamma\, h_{xx} + P_d, \tag{5-15}$$

and express the total pressure gradient as

$$\frac{dP}{dx} = -\gamma\, h_{xxx} + \frac{dP_d}{dx} = -\gamma\, h_{xxx} + \frac{\pi\, C\, \rho_1\, \rho_2}{2}\ \frac{h_x}{h^4}. \tag{5-16}$$

or

$$\frac{dP}{dx} = -\frac{\gamma\, h_\infty}{l^3}\ \tilde{h}_{\tilde{x}\tilde{x}\tilde{x}} + \frac{\pi\, C\, \rho_1\, \rho_2}{2\, l\, {h_\infty}^3}\ \frac{\tilde{h}_{\tilde{x}}}{\tilde{h}^4}. \tag{5-17}$$

where h and x have been replaced by the non-dimensional substitutions $h = h_\infty\, \tilde{h}$ and $x = l\, \tilde{x}$ where h_∞ is the farfield fluid height and l is the horizontal length scale.

At this point, it is helpful to introduce a quantity called the capillary length. Capillary length is a characteristic length scale for a fluid subject to a body force as well as surface tension. For length scales below the capillary length, the liquid can be considered to have a low Bond number (ratio of body force to surface tension force) and thus dominated by surface tension. Conversely, for length scales above the capillary length, the liquid can be considered to have a high Bond number and thus dominated by

the body forces. Kralchevsky and Nagayama [73] provide a definition of capillary length that considers gravitational as well as Van der Waals (disjoining pressure) body forces,

$$q^{-1} = \left(\frac{\Delta\rho\, g}{\gamma} + \frac{dP_d/dh}{\gamma} \right)^{-1/2}, \tag{5-18}$$

where $\Delta\rho = \rho_{\text{water}} - \rho_{\text{air}} \approx 999\ \text{kg/m}^3$, and g is gravitational acceleration. The first term on the right side of equation (5-18) is the ratio of the gravitational body force to surface tension and the second term is the ratio of the disjoining pressure effect to surface tension. If we compare the disjoining pressure term to the gravitational term, we see that for a 50 nm tall film of water, the disjoining pressure term is $\sim 120{,}000$ times greater than the gravitational term. As we could have expected, we can thus neglect gravitational effects in our nanoscale system. The capillary length therefore becomes

$$q^{-1} = \left(\frac{\pi\, C\, \rho_1\, \rho_2}{2\, \gamma\, h^4} \right)^{-1/2}. \tag{5-19}$$

We can also compare the disjoining pressure effect to surface tension by taking the ratio of disjoining pressure term (2nd term) to the surface tension term (1st term) in equation (5-17) to get

$$Bo_d = \frac{\pi\, C\, \rho_1\, \rho_2\, l^2}{2\, \gamma\, {h_\infty}^4}, \tag{5-20}$$

which we will call the disjoining pressure Bond number. Bo_d is similar to the traditional Bond number in that it represents the relative importance of a body force to the surface tension force, except the body force in Bo_d is the Van der Waals force, not gravity (as in traditional Bond number). We can also relate equations (5-19) and (5-20) with the substitution

$$l^2 = Bo_d\, q^{-2}. \tag{5-21}$$

Equations (5-19) – (5-21) allow us to identify regimes in which the hydrodynamics within the thin film of water should be dominated by the disjoining pressure effect, i.e., the characteristic lateral length scale is larger than q^{-1} and therefore $Bo_d \gg 1$. Supposing that the P_d dominated regime is defined as $Bo_d \geq 10$, one can calculate the capillary length for a system using equation (5-19) and then use equation (5-21) to find that if $l \geq \sqrt{10}\, q^{-1}$, then the disjoining pressure effect is expected to dominant. To illustrate the magnitude of these quantities, a 50 nm film of water on a silicon nitride surface at room temperature has a capillary length of $q^{-1} \approx 7.7$ μm. If the film extends for a distance of $l \geq 24$ μm, then $Bo_d \geq 10$. A 30 nm film of water on a silicon nitride surface at room temperature has a capillary length of $q^{-1} \approx 2.8$ μm, and if $l \geq 8.9$ μm then $Bo_d \geq 10$. A 20 nm film of water on a silicon nitride surface at room temperature has a capillary length of $q^{-1} \approx 1.2$ μm, and if $l \geq 3.9$ μm then $Bo_d \geq 10$. In this high Bo_d regime, it is expected that the shape of the liquid/vapor interface as well as the associated liquid flow is can be well described by the disjoining pressure effect alone.

5.1.2: Capillary Force Background

Capillary forces between particles become important when the thickness of the liquid layer drops below the particle height. Kralchevsky and Nagayama [73] derived an analytical expression for the immersion capillary force between two particles resting on a surface and protruding from a liquid thin film, given by

$$F = 2\,\pi\,\gamma\,Q_1\,Q_2\,q\,K_1[q\,d], \tag{5-22}$$

$$Q_k = r_k \, \mathrm{Sin}[\varphi_k], \tag{5-23}$$

where γ is surface tension, q is capillary length (defined in equation (5-19)), d is the separation distance between particles, K_1 is modified Bessel function, r_k is contact line radius, and φ_k is meniscus slope angle. See Figure 5-5 for an illustration of the geometric parameters.

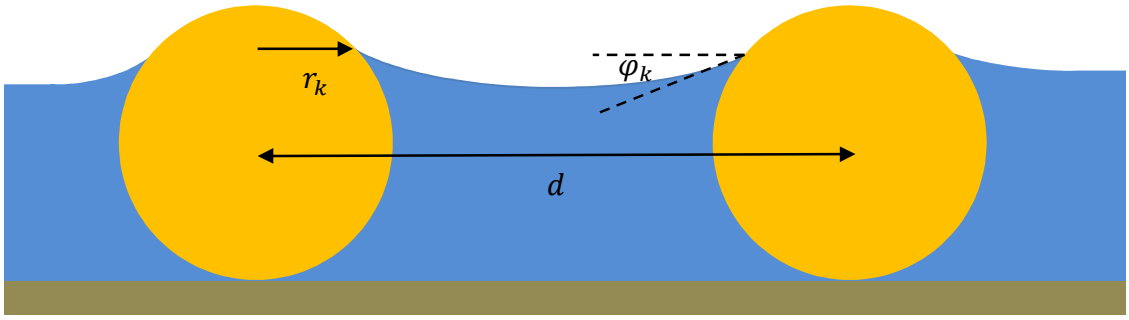

Figure 5-5: Illustration of relevant geometric parameters for lateral capillary force interaction between particles in a liquid thin film.

Section 5.2: Discussion

There are several forces in our system: thermal forces, surface tension forces, convective forces, capillary forces, and adhesion forces between the particles and the silicon nitride surface on which they rest. Our goal is to compare these forces to determine which ones dominate. Particle aggregation occurred at all levels of magnification, though to varying extents and at varying rates. At high magnification (500,000X and 600,000X), aggregation occurred most quickly and typically resulted in very few clusters or even a single cluster containing all of the initially dispersed particles visible in the observation window (see Figure 4-13 and Figure 4-14). It is interesting to

note that with a magnification of 500,000X, which provided slightly slower kinetics compared to a magnification of 600,000X, the particles reached a slightly lower interparticle mean distance. This indicates that the slower process was able to pack particles together more effectively, which is consistent with the results of Zhao et al. [78], who found that the assembly process resulting from rapid solvent evaporation at elevated temperature (40°C) produced disordered structures, while slow evaporation rates at room temperature produced both ordered and disordered structures. At low magnification (160,000X and 240,000X), aggregation occurred more slowly and typically resulted in many disjoint small clusters (at least in the time span of the experiment) (see Figure 4-11 and Figure 4-12). The dependence of the aggregation process on magnification suggests that aggregation was driven by beam effects, i.e., the evaporation of the liquid due to heating from the beam. The spot size of the beam is fixed (recall that the microscope was operated in STEM mode with a focused rastered beam), as is the pixel size of the image (1024 x 881), which means that as the magnification increases, the area through which the electrons pass decreases. This results in an increased flux of electrons through the sample at increased magnification. So at higher magnification, heating should be more significant, evaporation should be more significant, and the aggregation phenomena, if driven by the evaporation of the liquid, should be more pronounced. Figure 4-15 – Figure 4-17 are consistent with this trend.

Close examination of Figure 4-11 and Figure 4-12 reveals that not all of the particles in the field of view move the same distance or at the same rate. There is an outer region near the perimeter of the image where particles experience significant motion, and

an inner region where particles, comparatively, do not move as much. So the forces experienced by the particles are not experienced equally by all of the particles in the field of view. Let us consider some of the possible forces & energies influencing the system through qualitative as well as quantitative comparisons.

5.2.1: Thermal Forces

While always present, thermal fluctuations do not result in directed motion unless there is a gradient in temperature. There is, indeed, a gradient of temperature in our system. The region being irradiated by the beam should be hotter than the surrounding area outside of the beam. Directed motion, resulting from thermal forces, would therefore drive particles *out* of the field of view and *away* from the center of the image due to the increase in diffusivity with temperature (thermophoresis). This is not what we observe. In all our experiments, the particles migrated towards the center of the imaged region. Thus, thermophoresis of particles due to a thermal gradient is likely not important.

Temperature variations also produce gradients in surface tension that can lead to fluid motion, termed the Marangoni Effect. When applied to a shallow body of liquid with a lateral temperature gradient, the effect can produce thermocapillary motion, typically drawing the fluid from regions of high temperature (low surface tension) to regions of low temperature (high surface tension) [91]. As in the case of thermophoresis, thermocapillary motion would be in the opposite direction from the observed motion of the particles. It is possible, however, that thermocapillary motion could play a role in the influencing the height of the thin liquid film, which has important consequences on the pressure (and pressure gradients) in the liquid as described earlier in subsection 5.1.1. We

assume, however, that temperature variations are not likely to be significant at the length scales considered here and ignore Marangoni Effects.

How about thermal energy as the cause of random motion of particles? Let us consider a particle undergoing a random walk due to Brownian motion. The well-known expression for mean square displacement of a particle moving in n-dimensional space ($n = 1, 2,$ or 3), is given by

$$\langle r^2 \rangle_n = 2\, n\, D\, t, \tag{5-24}$$

where D is the diffusion coefficient and t is time (derivation presented in Appendix E). In our case, the expression for 2-D Brownian motion (equation (5-24) with $n = 2$) is appropriate because the particles are confined to a thin layer. We replace D with the Stokes-Einstein relation (for a fully submerged particle), used earlier in equation (3-8), to get

$$\langle r^2 \rangle_{2D} = \frac{2\, k_B\, T\, t}{3\, \pi\, \mu\, R} \tag{5-25}$$

where k_B is the Boltzmann constant, T is temperature, t is time, μ is viscosity of the liquid (water), and R is the particle radius. From this, one typically expresses the displacement of a particle with the root mean square displacement: $\langle r^2 \rangle^{1/2}$. To compute $\langle r^2 \rangle^{1/2}$ we use $R = 8$ nm, the mean particle radius measured in the initial image of all datasets at all magnifications. We will consider a time interval of 10 seconds (the experiments depicted in Figure 4-15 – Figure 4-18 lasted for 70 – 450 seconds). We can get a lower bound for $\langle r^2 \rangle_{2D}$ with values of $T = 30$ °C and $\mu = 0.799 \times 10^{-3}$ N s/m, and an upper bound for $\langle r^2 \rangle_{2D}$ with values of $T = 90$ °C and $\mu = 0.316 \times 10^{-3}$ N s/m

[92] (keeping in mind that the beam heats the sample above room temperature but we've never seen boiling with our imaging conditions). This gives the following values:

$\langle r^2 \rangle^{1/2}{}_{min} = 37$ μm

$\langle r^2 \rangle^{1/2}{}_{max} = 65$ μm.

This means that unrestricted Brownian motion as a result of the thermal energy of the system should produce particle motion on the order of 37 μm – 65 μm over the course of 10 seconds. The thermal motion of suspended particles close to a surface is hindered by viscous drag. Thus, the above estimates of the thermal motion are likely to be overestimates. Nevertheless, one would expect suspended particles to travel significant distances over the course of an experiment. With motions of even a fraction of the above magnitudes, particles would be flying in and out of the field of view throughout the process, likely bumping into each other in a diffusion limited aggregation process similar to what was discussed in Chapter 3, but confined to 2D. This clearly does not happen here. In most of the aggregation footage, the particles did not appear to experience a great deal of random thermal motion. Occasionally in the high magnification images (500,000X and 600,000X) a particle or small cluster jumped across the image and/or rotated 180 degrees, seemingly at random; however, in general there was not much random motion observed. This is a somewhat surprising observation, given that thermal energy is generally considered a prominent factor in nanoscale particle systems.

This indicates that random thermal motion in our system of particles was suppressed. The question is, by what means was it suppressed? It is important to note that

random particle motion was not suppressed solely in the region being imaged by the electron beam; particles throughout the gas/vapor region of the imaging window remained fixed until they were zoomed in on by the electron beam, otherwise there would have been aggregates present throughout the imaging window. This lets us exclude beam effects or charge artifacts as the reason that particle diffusion was suppressed. We conclude that the particles must have been stuck to the silicon nitride membrane surface, probably due to intermolecular forces, i.e., Van der Waals forces, hydrogen bonds, and others. These forces were strong enough to hold the particles in place and resist random Brownian motion due to thermal energy, but not strong enough to resist other forces that drove aggregation.

Thermal forces conclusion: Thermal forces on the particles are not significant. Random Brownian motion is suppressed by particle interaction with the surface, which is then overwhelmed by another force(s) to drive assembly. The interaction energy between a particle and the surface must be greater than the thermal energy of the system, $E_{thermal} = k_B\,T \sim 4 \times 10^{-21}\,J$*, and the interaction energy that drives motion and aggregation must in turn be even greater. Marangoni Effects and associated flows driven by surface tension gradients are ignored in this analysis.*

5.2.2: Surface Tension Force on a Single Particle

A single partially submerged particle at a liquid surface with a height gradient can experience an imbalance of forces based on surface tension that will result in motion. The situation is more complicated when multiple particles are present, as they would produce

mutual deformations of the liquid surface to yield interparticle capillary forces. In our experiment, the imaged region was being heated and presumably the liquid was evaporating. Liquid from outside the image region could flow into the evaporation zone to replenish the evaporating liquid. If the thin liquid film height in the imaging region was not uniform, we must question whether the gradient in film height could be responsible for particle motion.

We expect the center of the image region to have a thinner liquid film than the perimeter since the center is furthest from the supply of fresh liquid. A particle on the surface would see the environment illustrated in Figure 5-6. The case of a floating particle on a curved liquid surface was explored by Katoh et al. [93]. They examined the cases of wetting and non-wetting particles on convex and concave meniscus surfaces. In their analysis, the case of a wetting particle whose density was greater than that of the liquid was trivial because they were looking at bulk liquid, not a thin film, and a heavy wetting particle would simply sink into the liquid. Nevertheless, we can employ similar analysis to that of Katoh et al. and also include the reactive force that the surface exerts on the particle. We assume that our gold nanoparticles are wetted by the liquid, since the contact angle of water with gold is less than 90 degrees [94]. In addition, the nanorods were coated with CTAB to keep them stable in water (increasing wettability). When the contact angle is $< 90°$, a meniscus will rise around the particle, with an associated surface tension force. The surface tension force acts around the wetted perimeter of the particle and the resultant of the force points in a direction that is inward and orthogonal to the liquid surface (Figure 5-6(b) and (c)).

Katoh et al. consider two other forces: gravity and buoyancy. Neither of these forces is relevant to our system because we are dealing with nanoparticles in a thin film for which the (traditional) Bond number is very small. The Bond number is a non-dimensional number that gives the relative importance of gravity forces to surface tension forces:

$$\mathrm{Bo} = \frac{(\Delta\rho) g\, L^2}{\gamma}, \tag{5-26}$$

where $\Delta\rho$ is the difference in density between the particle and the suspending fluid, g is the gravitational acceleration, L is the characteristic length, and γ is surface tension. For gold particles ($\rho_{\mathrm{gold}} = 19{,}300\ \mathrm{kg/m^3}$) in water ($\rho_{\mathrm{water}} = 1{,}000\ \mathrm{kg/m^3}$ and $\gamma_{\mathrm{water}}(25°\mathrm{C}) = 71.97 \times 10^{-3}\ \mathrm{N/m}$) with a film thickness that is assumed to be on the order of the particle diameter ($L = 16$ nm), we have Bo $\sim 6{\times}10^{-10}$. As an upper bound, consider that a 100 nm film of water at 90 °C would have Bo $\sim 3{\times}10^{-8}$. When Bo < 0.01, gravitational forces can be safely neglected in favor of surface tension forces [95]. Katoh et al. draw a vector diagram of forces on a floating wetted particle that includes gravity (acting downward), buoyancy (acting upward), and surface tension (acting down and away at an angle) to show that there is a net force that moves the particle sideways up the meniscus. In our case, we replace the gravity force with an attractive force between the particle and the silicon nitride surface due to intermolecular interactions, and replace the buoyancy force with a complimentary force that represents the energetic penalty paid to displace a volume of liquid (which has its own attractive interaction with silicon nitride surface) by the particle. We can refer to this as the Van der

Waals buoyancy. In addition, we have a reaction force between the particle and the membrane surface. The vector sum of these forces is depicted in Figure 5-6(c). It shows that a particle on a surface that is wetted by a non-uniform film of water will experience a net force that pulls the particle *into* the thicker part of the film. A similar conclusion can be arrived at by energetic considerations. As the wetted surface area of the particle increases, its energy decreases. This is similar to the conclusion reached by Katoh et al., which states that a buoyant wetted particle will move into the thicker part of the liquid (up the meniscus).

Surface tension forces conclusion: Surface tension force experienced by a single partially wetted particle in a liquid film of variable height is directed towards the region of thicker film and cannot explain the aggregation phenomena that was observed in our experiments. If present, such forces would draw the particle into the thicker part of the liquid film, i.e. from the center to the edge. This is not consistent with the observed behavior of the system.

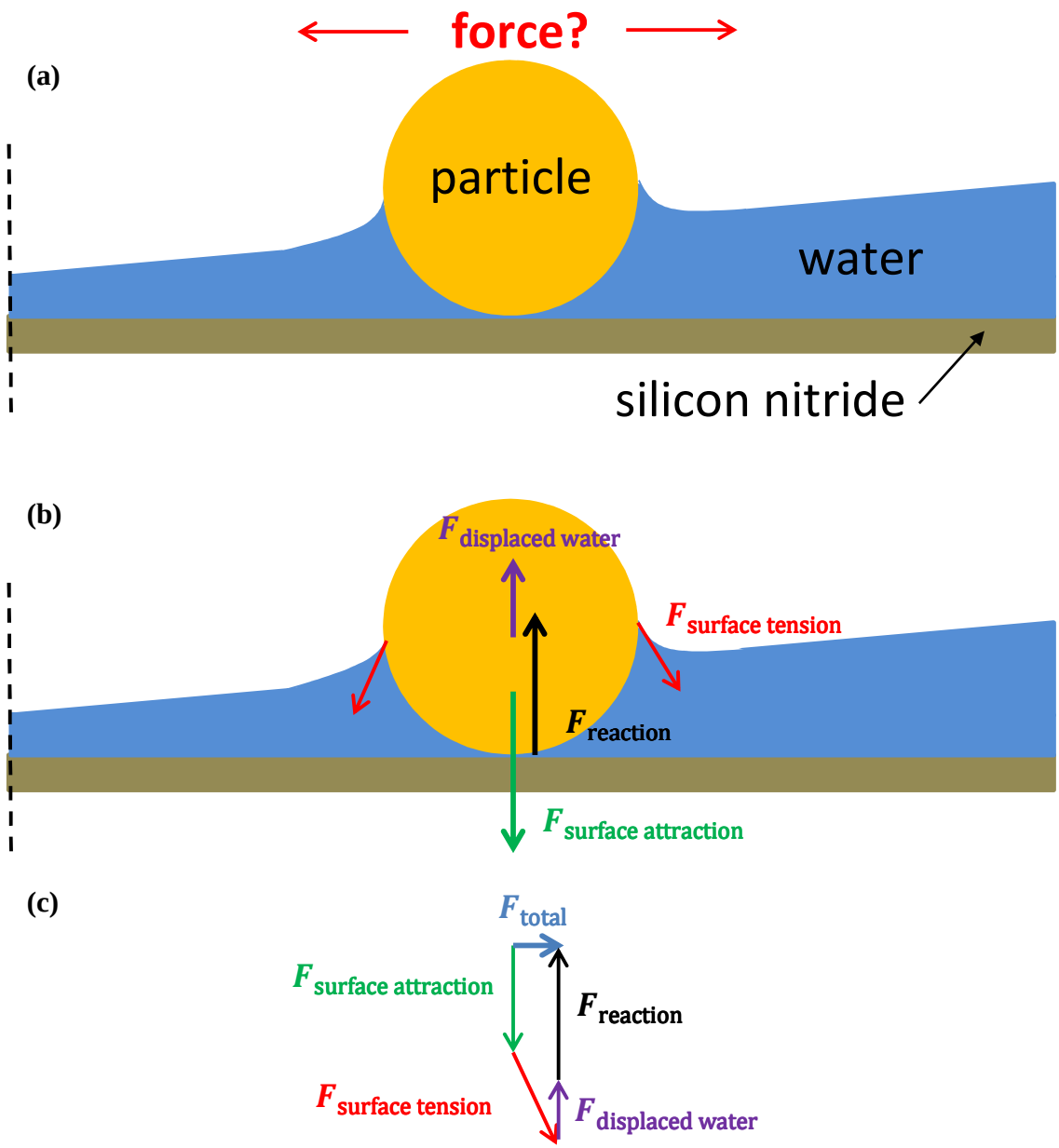

Figure 5-6: Illustration of a gold particle in a liquid thin film of variable thickness. If there was a variation in liquid film thickness in the imaging window, we would expect the perimeter to be thicker than the center. The center of the imaging window is denoted by a dashed line. (a) Would a particle in this situation experience a force imbalance that could lead to motion? If so, which way would it move? (b) Forces acting on the particle include surface attraction to the substrate (green), an opposing force arising from the energetic penalty paid to displace liquid to accommodate the particle (purple), a reaction force at the surface (black) and surface tension (red). (c) A vector force diagram showing the resultant force in blue.

5.2.3: Capillary Forces

As described in Section 5.1, capillary forces have been established as an important factor to consider in the assembly of nanoparticles. However, capillary forces are not likely to be significant in our system. Nanoparticles and nanorods, did not move or assemble deterministically unless they were being imaged with the electron beam. From this, we surmise that the equilibrium thickness of the thin liquid film was thicker than the size of particle or rod (> 20nm). As described in Section 4.5, not all of the particles in the field of view participated in the aggregation process, and in cases of incomplete aggregation it was often the particles in the center that did not aggregate (see Figure 4-11 and Figure 4-12). This is not consistent with what we would expect for capillary force-induced assembly. Particles at the center should be in the thinnest part of the liquid film, which would make them protrude the most and therefore experience the strongest interparticle capillary forces. Capillary forces are a viable explanation for the packing of nanorods in Figure 4-7, however, they do not explain the motion of the nanorods ejected from the bulk liquid in Figure 4-6, which came to rest at seemingly arbitrary locations in the thin film that were not near any other particles. If capillary forces drew a particle into the thin film region, why didn't the particle continue moving to join with the particle(s) responsible for the capillary force? Additionally the nanorods already in the thin film region of Figure 4-6 (green circle) did not move. The nanorods that were pushed by the surging contact line in Figure 4-8 were subject to forces of some kind that produced motion, but they did not aggregate while in the thin liquid film. If capillary forces were present and significant, why did the two large distinct clusters of

nanorods in Figure 4-9 not draw together to form a single cluster? The precise thickness of the thin liquid film is unknown, which makes it difficult to definitively state whether capillary forces can be ruled out completely (they are zero if the particle is not protruding from the film).

Capillary force conclusion: Interparticle capillary forces alone do not appear to be a viable explanation for the variety of interesting particle behaviors observed in our experiments.

5.2.4: Pressure Gradients and Flow in the Liquid

The liquid film in the imaging region is irradiated by the electron beam. As a result, the temperature in the irradiated region increases, with a corresponding increase in evaporation rate. The evaporation provides a means of mass transport out of the thin liquid film that will cause a decrease in film height relative to the surrounding unheated region. As described in Section 5.1, spatial variations in film height give rise to pressure gradients, due to both surface tension and disjoining pressure of the liquid (equation (5-17)). Liquid lost from the heated thin film region can be replaced by liquid flow from the surroundings. Lateral pressure gradients in the thin liquid film provide a mechanism for directed particle motion via non-uniform pressure on a particle's surface, as well as convection of fluid with associated hydrodynamic drag. For the situation described in Section 4.3, hereby referred to as the contact line model, liquid lost from the heated thin film can be replenished by the much thicker "bulk" liquid at the contact line, as well as the thin liquid film outside of the imaging area (see Figure 5-7). We are interested in

what happens right next to the “bulk” liquid region when the “contact line” passes over a particle, so we perform 1-D analysis in Cartesian coordinates (valid for a particle that lies on the $\tilde{x}$-axis for which flow in the $\tilde{y}$-direction would cancel out due to symmetry). Similarly, for the situation described in Section 4.4, hereby referred to as the heated patch model, liquid lost from the heated thin film can be replenished by the surrounding, unheated thin film (see Figure 5-8). We consider the hypothetical case of the imaging region as a circular disk (the image is actually a rectangle) and perform 1-D analysis in axisymmetric cylindrical coordinates.

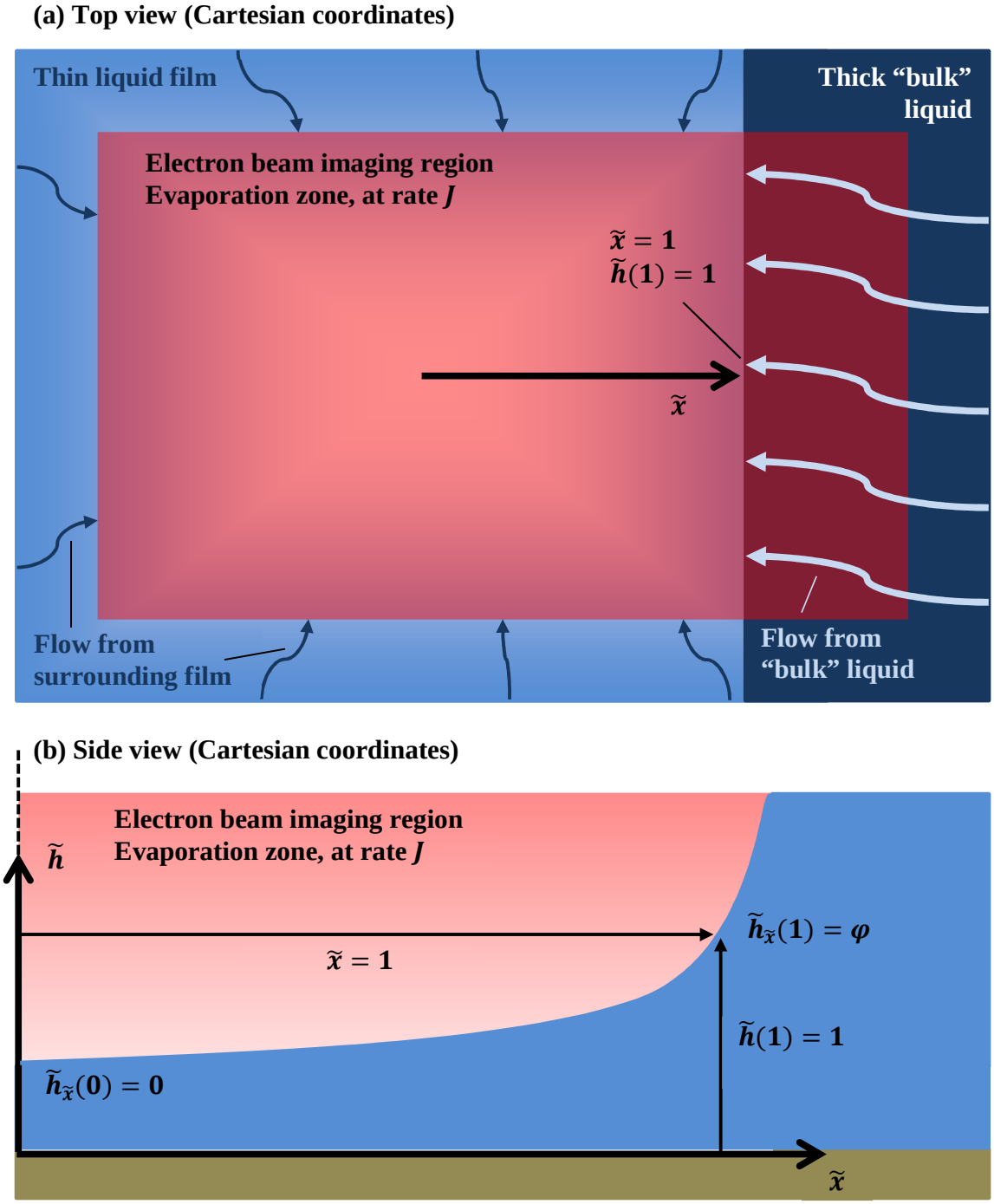

Figure 5-7: Top view (a) and side view (b) illustration of the liquid film (blue) and the electron beam imaging region (evaporation zone) (red) in the contact line model that applies to Section 4.3. Refer also to the illustration in Figure 4-3. Cartesian coordinates are used. See Figure 4-5, Figure 4-6, and Figure 4-7 for comparison to the experiment. All variables are normalized.

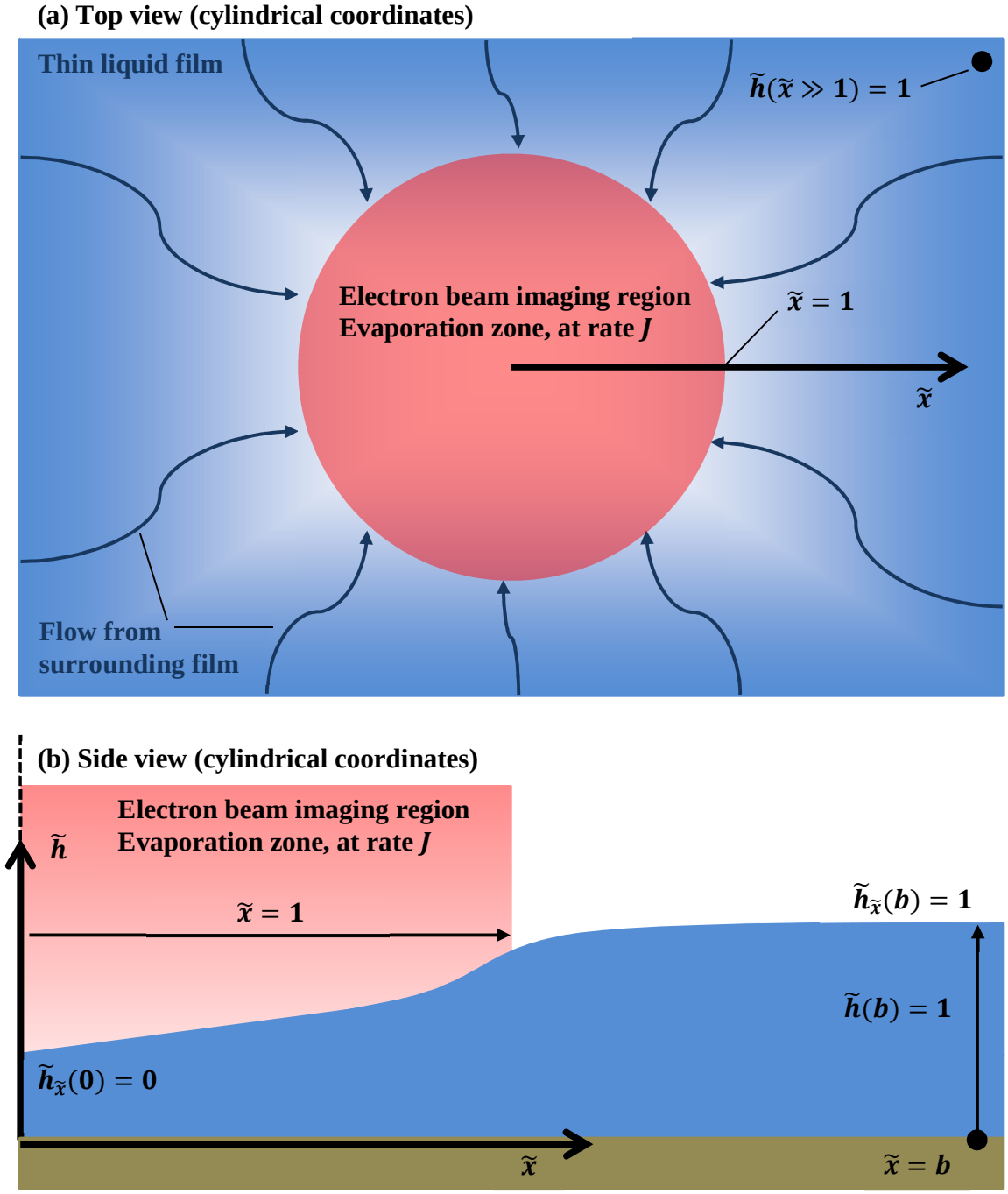

Figure 5-8: Top view (a) and side view (b) illustration of the liquid film (blue) and the electron beam imaging region (evaporation zone) (red) in the heated patch model that applies to Section 4.4. Refer also to the illustration in Figure 4-3. The coordinate system is approximated with axisymmetric cylindrical coordinates. See Figure 4-10 for comparison to the experiment. All variables are normalized.

Conservation of mass dictates that the following continuity equations must hold true:

$$\nabla \cdot (h\,\bar{v}) + J = 0 \quad (0 \le \tilde{x} \le 1) \tag{5-27}$$

$$\nabla \cdot (h\,\bar{v}) = 0 \quad (1 < \tilde{x}). \tag{5-28}$$

In the above, h is the film height, $\bar{v}$ is the mean fluid velocity (averaged over the height of the film), and J is the evaporative flux (per unit length). Recall the non-dimensional substitutions used in equation (5-17), $h = h_\infty\,\tilde{h}$ and $x = l\,\tilde{x}$, where h_∞ is the height scale (edge height in contact line model and far-field height in heated patch model) and l is the horizontal length scale (half the diameter of the evaporation zone). Both h and $\bar{v}$ are functions of the position $\tilde{x}$. For simplicity (and for lack of more detailed information), we will assume that the evaporation rate J is uniform since the electron beam irradiates the imaging window more or less evenly and we assume small temperature variations. We also assume that the re-condensation of evaporated water vapor occurs over a relatively large area compared to the area of evaporation (ratio of surface area of whole bubble region to surface area of imaging region ~ 8000:1) and so the effect of the flux of condensing water vapor on the flow field can be ignored.

The domain of $\tilde{x}$ in the heated patch model is $0 \le \tilde{x} \le b$ where $b \gg 1$, while the domain of $\tilde{x}$ in the contact line model is $0 \le \tilde{x} \le 1$ (see Figure 5-7 and Figure 5-8). However, for completeness, expressions in the contact line model analysis (Cartesian coordinate) that follows are given over the same domain as the heated patch model, i.e., $0 \le \tilde{x} \le b$ with heating on $0 \le \tilde{x} \le 1$. When applying the expressions in the contact line model to our particular experiment we specify $b = 1$.

The Navier-Stokes equation for fluid flow reduces to the Stokes equation at low Reynolds number:

$$\mu \nabla^2 v = \nabla P, \tag{5-29}$$

which is a valid simplification for fluid flow in a thin liquid film that is under 100 nm. The Stokes equation in Cartesian and cylindrical coordinates with scaled distances ($x = l\,\tilde{x}$, $z = h\,\tilde{z}$) becomes, respectively

$$h^2\,\frac{\partial^2 v}{\partial \tilde{x}^2} + l^2\,\frac{\partial^2 v}{\partial \tilde{z}^2} = \frac{h^2\,l^2}{\mu}\,\frac{\partial P}{\partial x}, \tag{5-30}$$

$$h^2\,\frac{\partial}{\partial \tilde{x}}\left(\frac{1}{\tilde{x}}\,\frac{\partial}{\partial \tilde{x}}(\tilde{x}\,v)\right) + l^2\,\frac{\partial^2 v}{\partial \tilde{z}^2} = \frac{h^2\,l^2}{\mu}\,\frac{\partial P}{\partial x}. \tag{5-31}$$

Assuming that $l \gg h$, both equations reduce to

$$\frac{\partial^2 v}{\partial \tilde{z}^2} = \frac{h^2}{\mu}\,\frac{\partial P}{\partial x}, \tag{5-32}$$

for which the mean fluid velocity for Couette flow between a non-slip surface ($\tilde{z} = 0$) and a free surface ($\tilde{z} = \tilde{h}$) gives

$$\bar{v} = \int_0^1 v\,d\tilde{z} = -\frac{h^2}{3\,\mu}\,\frac{dP}{dx} = \frac{\gamma\,{h_\infty}^3}{3\,\mu\,l^3}\,\tilde{h}^2\left(\tilde{h}_{\tilde{x}\tilde{x}\tilde{x}} - Bo_d\,\frac{\tilde{h}_{\tilde{x}}}{\tilde{h}^4}\right), \tag{5-33}$$

where dP/dx has been replaced by the expression in equation (5-17) and the disjoining pressure Bond number Bo_d was defined previously in equation (5-20). The velocity can be normalized by

$$v_0 = \frac{\gamma\,{h_\infty}^3}{3\,\mu\,l^3} \tag{5-34}$$

to get

$$\tilde{v} = \frac{\bar{v}}{v_0} = \tilde{h}^2 \left(\tilde{h}_{\tilde{x}\tilde{x}\tilde{x}} - Bo_d \frac{\tilde{h}_{\tilde{x}}}{\tilde{h}^4} \right). \quad (5\text{-}35)$$

The validity of the $l \gg h$ assumption that allows equations (5-30) and (5-31) to be simplified is tested by computing the velocity of the fluid and then comparing the magnitude of the terms that were neglected to the terms that were retained, i.e.,

$$\frac{h^2 \frac{\partial^2 v}{\partial \tilde{x}^2}}{l^2 \frac{\partial^2 v}{\partial \tilde{z}^2}} \quad \text{(Cartesian coordinates)}, \quad (5\text{-}36)$$

$$\frac{h^2 \frac{\partial}{\partial \tilde{x}} \left(\frac{1}{\tilde{x}} \frac{\partial}{\partial \tilde{x}} (\tilde{x}\, v) \right)}{l^2 \frac{\partial^2 v}{\partial \tilde{z}^2}} \quad \text{(cylindrical coordinates)}. \quad (5\text{-}37)$$

Contact line model - Cartesian coordinate analysis

The mass conservation equations (5-27) and (5-28) become

$$\frac{\mathrm{d}}{l\, d\tilde{x}} \left(h_\infty \tilde{h}\, \bar{v} \right) + J = 0 \quad (0 \le \tilde{x} \le 1) \quad (5\text{-}38)$$

$$\frac{\mathrm{d}}{l\, d\tilde{x}} \left(h_\infty \tilde{h}\, \bar{v} \right) = 0 \quad (1 < \tilde{x}). \quad (5\text{-}39)$$

Integration produces

$$\tilde{h}\, \bar{v} = -\frac{J\, l}{h_\infty} \tilde{x} \quad (0 \le \tilde{x} \le 1) \quad (5\text{-}40)$$

$$\tilde{h}\, \bar{v} = \left(\tilde{h}\, \bar{v} \right)|_{\tilde{x}=1} \quad (1 < \tilde{x}) \quad (5\text{-}41)$$

Substituting equation (5-33) for $\bar{v}$ and rearranging gives

$$\tilde{h}_{\tilde{x}\tilde{x}\tilde{x}} = Bo_d \frac{\tilde{h}_{\tilde{x}}}{\tilde{h}^4} - A \frac{\tilde{x}}{\tilde{h}^3} \quad (0 \le \tilde{x} \le 1), \quad (5\text{-}42)$$

$$\tilde{h}_{\tilde{x}\tilde{x}\tilde{x}} = Bo_d \frac{\tilde{h}_{\tilde{x}}}{\tilde{h}^4} - A \frac{1}{\tilde{h}^3} \qquad (1 < \tilde{x}), \tag{5-43}$$

where

$$\mathrm{A} = \frac{3\,\mu\, l^4\, J}{\gamma\, {h_\infty}^4}. \tag{5-44}$$

Combining equations (5-42) and (5-43), we write

$$\tilde{h}_{\tilde{x}\tilde{x}\tilde{x}} = Bo_d \frac{\tilde{h}_{\tilde{x}}}{\tilde{h}^4} - A \frac{1}{\tilde{h}^3} \left(\tilde{x}\,\mathrm{H}(1-\tilde{x}) + \mathrm{H}(\tilde{x}-1)\right), \tag{5-45}$$

where $\mathrm{H}(\tilde{x})$ is the Heaviside function. Equation (5-45) must be solved numerically and the resulting solution is plugged into equation (5-35) to calculate the fluid velocity $\tilde{v}$. Boundary conditions (see Figure 5-7) for equation (5-45) are

$$\tilde{h}_{\tilde{x}}(0) = 0 \tag{5-46}$$

$$\tilde{h}(b) = 1 \tag{5-47}$$

and

$$\tilde{h}_{\tilde{x}}(b) = \varphi \tag{5-48}$$

where φ is the slope at the boundary. We will explore the effect that different values of φ have on the solution.

We derive an expression for equation (5-36) that tells us whether our velocity solution validates the $l \gg h$ assumption that was employed to simplify the Stokes equation (equation (5-30)). The denominator is given by

$$l^2 \frac{\partial^2 v}{\partial \tilde{z}^2} = \frac{h^2\, l^2}{\mu} \frac{\partial P}{\partial x} = \frac{h^2\, l^2}{\mu} \frac{-3\,\mu\,\bar{v}}{h^2} = -3\, l^2\, v_0\, \tilde{v}, \tag{5-49}$$

where equation (5-32) is used to define $\partial^2 v/\partial \tilde{z}^2$, and (5-33) is used to replace the dP/dx term. The numerator is given by

$$h^2 \frac{\partial^2 v_{max}}{\partial \tilde{x}^2} = h^2 \frac{\partial^2 \left(\frac{3}{2}\,\bar{v}\right)}{\partial \tilde{x}^2} = -\frac{3\,J\,l\,h_\infty}{2}\left(-2\,\tilde{h}_{\tilde{x}} + \tilde{x}\left(\frac{2\,\tilde{h}_{\tilde{x}}{}^2}{\tilde{h}} - \tilde{h}_{\tilde{x}\tilde{x}}\right)\right) \quad (0 \le \tilde{x} \le 1), \tag{5-50}$$

$$h^2 \frac{\partial^2 v_{max}}{\partial \tilde{x}^2} = h^2 \frac{\partial^2 \left(\frac{3}{2}\,\bar{v}\right)}{\partial \tilde{x}^2} = -\frac{3\,J\,l\,h_\infty}{2}\left(\frac{2\,\tilde{h}_{\tilde{x}}{}^2}{\tilde{h}} - \tilde{h}_{\tilde{x}\tilde{x}}\right) \quad (1 < \tilde{x}), \tag{5-51}$$

where the maximum velocity $v_{max} = \frac{3}{2}\,\bar{v}$ for Couette flow is used and $\bar{v}$ is given by equations (5-40) and (5-41). Taking the ratio of equations (5-50) and (5-51) to (5-49) we get

$$\text{ratio}_{dx:dz} = \frac{A}{2}\frac{h_\infty{}^2}{l^2}\frac{1}{\tilde{v}}\left(\left(-2\,\tilde{h}_{\tilde{x}} + \tilde{x}\left(\frac{2\,\tilde{h}_{\tilde{x}}{}^2}{\tilde{h}} - \tilde{h}_{\tilde{x}\tilde{x}}\right)\right)\mathrm{H}(1-\tilde{x}) + \left(\frac{2\,\tilde{h}_{\tilde{x}}{}^2}{\tilde{h}} - \tilde{h}_{\tilde{x}\tilde{x}}\right)\mathrm{H}(\tilde{x}-1)\right), \tag{5-52}$$

where A is defined previously in equation (5-44), and $\tilde{v}$, $\tilde{h}$, $\tilde{h}_{\tilde{x}}$, and $\tilde{h}_{\tilde{x}\tilde{x}}$ are all determined from the solution to equation (5-45).

We can simplify equations (5-42) and (5-43) for the case of large Bo_d and write

$$\frac{\tilde{h}_{\tilde{x}}}{\tilde{h}} = \frac{A}{Bo_d}\,\tilde{x} \quad (0 \le \tilde{x} \le 1) \tag{5-53}$$

$$\frac{\tilde{h}_{\tilde{x}}}{\tilde{h}} = \frac{A}{Bo_d} \quad (1 < \tilde{x}). \tag{5-54}$$

Integration yields

$$\begin{aligned}\tilde{h}_{high\ Bo_d} &= \tilde{h}_0\ Exp\left(\frac{A}{2\ Bo_d}\ \tilde{x}^2\right)\\ &= \tilde{h}_1\ Exp\left(\frac{A}{2\ Bo_d}\ (\tilde{x}^2-1)\right)\quad (0\le\tilde{x}\le 1)\end{aligned} \tag{5-55}$$

$$\begin{aligned}\tilde{h}_{high\ Bo_d} &= \tilde{h}_1\ Exp\left(\frac{A}{Bo_d}\ (\tilde{x}-1)\right)\\ &= Exp\left(\frac{A}{Bo_d}\ (\tilde{x}-b)\right)\quad (1<\tilde{x}\le b),\end{aligned} \tag{5-56}$$

where b is the far-field bound on $\tilde{x}$, $\tilde{h}(0)=\tilde{h}_0$, $\tilde{h}(1)=\tilde{h}_1$, and $\tilde{h}(b)=1$. Here we have chosen to satisfy the $\tilde{h}(b)$ boundary condition and neglected the $\tilde{h}_{\tilde{x}}(b)$ boundary condition (the $\tilde{h}_{\tilde{x}}(0)=0$ boundary condition is automatically satisfied by the equation). With some rearrangement we get

$$\tilde{h}_{high\ Bo_d} = Exp\left(\frac{A}{2\ Bo_d}\ (\tilde{x}^2+1-2\ b)\right)\quad (0\le\tilde{x}\le 1) \tag{5-57}$$

$$\tilde{h}_{high\ Bo_d} = Exp\left(\frac{A}{2\ Bo_d}\ (2\ \tilde{x}-2\ b)\right)\quad (1<\tilde{x}\le b). \tag{5-58}$$

Combining equations (5-57) and (5-58), we write

$$\tilde{h}_{high\ Bo_d} = Exp\left(\frac{A}{2\ Bo_d}\ \left((\tilde{x}^2+1-2\ b)\ \mathrm{H}(1-\tilde{x})\right.\right.$$
$$\left.\left.+\ (2\ \tilde{x}-2\ b)\ \mathrm{H}(\tilde{x}-1)\right)\right). \tag{5-59}$$

The high Bo_d case also has a simplified expression for velocity. Equation (5-35) is simplified to

$$\tilde{v}_{high\ Bo_d} = -Bo_d\ \frac{\tilde{h}_{\tilde{x}}}{\tilde{h}^2}. \tag{5-60}$$

Referring to equations (5-53) and (5-54) we get

$$\tilde{v}_{high\ Bo_d} = -\mathrm{A}\ \frac{\tilde{x}}{\tilde{h}} \quad (0 \le \tilde{x} \le 1) \tag{5-61}$$

$$\tilde{v}_{high\ Bo_d} = -A\ \frac{1}{\tilde{h}} \quad (1 < \tilde{x} \le b). \tag{5-62}$$

Combining equations (5-61) and (5-62), we write

$$\tilde{v}_{high\ Bo_d} = -A\ \frac{1}{\tilde{h}}\ \big(\tilde{x}\ \mathrm{H}(1-\tilde{x}) + \mathrm{H}(\tilde{x}-1)\big). \tag{5-63}$$

<u>Heated patch model - cylindrical coordinate analysis, radial position $\tilde{x}$</u>

The mass conservation equations (5-27) and (5-28) become

$$\frac{1}{l\ \tilde{x}}\ \frac{\mathrm{d}}{l\ d\tilde{x}}\big(l\ h_\infty\ \tilde{x}\ \tilde{h}\ \bar{v}\big) + J = 0 \quad (0 \le \tilde{x} \le 1) \tag{5-64}$$

$$\frac{1}{l\ \tilde{x}}\ \frac{\mathrm{d}}{l\ d\tilde{x}}\big(l\ h_\infty\ \tilde{x}\ \tilde{h}\ \bar{v}\big) = 0 \quad (1 < \tilde{x}) \tag{5-65}$$

Integration produces

$$\tilde{h}\ \bar{v} = -\frac{J\ l}{2\ h_\infty}\ \tilde{x} \quad (0 \le \tilde{x} \le 1) \tag{5-66}$$

$$\tilde{h}\ \bar{v} = \frac{\big(\tilde{x}\ \tilde{h}\ \bar{v}\big)|_{\tilde{x}=1}}{\tilde{x}} \quad (1 < \tilde{x}) \tag{5-67}$$

Substituting equation (5-33) for $\bar{v}$ and rearranging gives

$$\tilde{h}_{\tilde{x}\tilde{x}\tilde{x}} = Bo_d\ \frac{\tilde{h}_{\tilde{x}}}{\tilde{h}^4} - \frac{A}{2}\ \frac{\tilde{x}}{\tilde{h}^3} \quad (0 \le \tilde{x} \le 1) \tag{5-68}$$

$$\tilde{h}_{\tilde{x}\tilde{x}\tilde{x}} = Bo_d \frac{\tilde{h}_{\tilde{x}}}{\tilde{h}^4} - \frac{A}{2} \frac{1}{\tilde{x}\,\tilde{h}^3} \qquad (1 < \tilde{x}) \tag{5-69}$$

where, as in equation (5-44) previously,

$$\mathrm{A} = \frac{3\,\mu\,l^4\,J}{\gamma\,{h_\infty}^4}. \tag{5-70}$$

Combining equations (5-68) and (5-69), we write

$$\boxed{\tilde{h}_{\tilde{x}\tilde{x}\tilde{x}} = Bo_d \frac{\tilde{h}_{\tilde{x}}}{\tilde{h}^4} - \frac{A}{2} \frac{1}{\tilde{h}^3} \left(\tilde{x}\,\mathrm{H}(1-\tilde{x}) + \frac{\mathrm{H}(\tilde{x}-1)}{\tilde{x}} \right),} \tag{5-71}$$

where $\mathrm{H}(\tilde{x})$ is the Heaviside function. Equation (5-71) must be solved numerically and the resulting solution is plugged into equation (5-35) to calculate the fluid velocity. Boundary conditions (see Figure 5-8) for equation (5-71) are

$$\tilde{h}_{\tilde{x}}(0) = 0 \tag{5-72}$$

$$\tilde{h}(b) = 1 \tag{5-73}$$

and

$$\tilde{h}_{\tilde{x}}(b) = 0. \tag{5-74}$$

One could also explore the effect of slope at the boundary b by choosing a nonzero value, as in equation (5-48).

We now derive an expression for equation (5-37) that tells us whether our velocity solution validates the $l \gg h$ assumption that was employed to simplify the Stokes equation (equation (5-31)). The denominator is given by

$$l^2 \frac{\partial^2 v}{\partial \tilde{z}^2} = \frac{h^2\,l^2}{\mu} \frac{\partial P}{\partial x} = \frac{h^2\,l^2}{\mu} \frac{-3\,\mu\,\bar{v}}{h^2} = -3\,l^2\,v_0\,\tilde{v}, \tag{5-75}$$

where equation (5-32) is used to define $\partial^2 v/\partial \tilde{z}^2$ and equation (5-33) is used to replace the dP/dx term. The numerator is given by

$$h^2 \frac{\partial}{\partial \tilde{x}}\left(\frac{1}{\tilde{x}} \frac{\partial}{\partial \tilde{x}}(\tilde{x}\, v)\right) = h^2 \frac{\partial}{\partial \tilde{x}}\left(\frac{1}{\tilde{x}} \frac{\partial}{\partial \tilde{x}}\left(\tilde{x} \frac{3}{2} \bar{v}\right)\right) = -\frac{3 J l h_\infty}{4}\left(-3 \tilde{h}_{\tilde{x}} + \tilde{x}\left(\frac{2 \tilde{h}_{\tilde{x}}^{\,2}}{\tilde{h}} - \tilde{h}_{\tilde{x}\tilde{x}}\right)\right) \quad (0 \le \tilde{x} \le 1), \tag{5-76}$$

$$h^2 \frac{\partial}{\partial \tilde{x}}\left(\frac{1}{\tilde{x}} \frac{\partial}{\partial \tilde{x}}(\tilde{x}\, v)\right) = h^2 \frac{\partial}{\partial \tilde{x}}\left(\frac{1}{\tilde{x}} \frac{\partial}{\partial \tilde{x}}\left(\tilde{x} \frac{3}{2} \bar{v}\right)\right) = -\frac{3 J l h_\infty}{4}\left(\frac{\tilde{h}_{\tilde{x}}}{\tilde{x}^2} + \frac{2 \tilde{h}_{\tilde{x}}^{\,2}}{\tilde{x}\, \tilde{h}} - \frac{\tilde{h}_{\tilde{x}\tilde{x}}}{\tilde{x}}\right) \quad (1 < \tilde{x}), \tag{5-77}$$

where the maximum velocity $v_{max} = \frac{3}{2} \bar{v}$ for Couette flow is used and $\bar{v}$ is given by equations (5-66) and (5-67). Taking the ratio of equations (5-76) and (5-77) to (5-75) we get

$$\text{ratio}_{dx:dz} = \frac{A}{4} \frac{h_\infty^{\,2}}{l^2} \frac{1}{\tilde{v}}\left(\left(-3 \tilde{h}_{\tilde{x}} + \tilde{x}\left(\frac{2 \tilde{h}_{\tilde{x}}^{\,2}}{\tilde{h}} - \tilde{h}_{\tilde{x}\tilde{x}}\right)\right) \mathrm{H}(1 - \tilde{x}) + \left(\frac{\tilde{h}_{\tilde{x}}}{\tilde{x}^2} + \frac{2 \tilde{h}_{\tilde{x}}^{\,2}}{\tilde{x}\, \tilde{h}} - \frac{\tilde{h}_{\tilde{x}\tilde{x}}}{\tilde{x}}\right) \mathrm{H}(\tilde{x} - 1)\right), \tag{5-78}$$

where A is defined previously in equation (5-70), and $\tilde{v}$, $\tilde{h}$, $\tilde{h}_{\tilde{x}}$, and $\tilde{h}_{\tilde{x}\tilde{x}}$ are all determined from the solution to equation (5-71).

We can simplify equations (5-68) and (5-69) for the case of large Bo_d and write

$$\frac{\tilde{h}_{\tilde{x}}}{\tilde{h}} = \frac{A}{2\, Bo_d} \tilde{x} \quad (0 \le \tilde{x} \le 1) \tag{5-79}$$

$$\frac{\tilde{h}_{\tilde{x}}}{\tilde{h}} = \frac{A}{2\,Bo_d}\,\frac{1}{\tilde{x}} \qquad (1 < \tilde{x}) \tag{5-80}$$

Integration yields

$$\begin{aligned}\tilde{h}_{high\ Bo_d} &= \tilde{h}_0\, Exp\left(\frac{A}{4\,Bo_d}\,\tilde{x}^2\right) \\ &= \tilde{h}_1\, Exp\left(\frac{A}{4\,Bo_d}\,(\tilde{x}^2 - 1)\right) \quad (\,0 \le \tilde{x} \le 1)\end{aligned} \tag{5-81}$$

$$\tilde{h}_{high\ Bo_d} = \tilde{h}_1\,\tilde{x}^{A/2\,Bo_d} = \left(\frac{\tilde{x}}{b}\right)^{A/2\,Bo_d} \qquad (1 < \tilde{x} \le b), \tag{5-82}$$

where b is the far-field bound on $\tilde{x}$, $\tilde{h}(0) = \tilde{h}_0$, $\tilde{h}(1) = \tilde{h}_1$, and $\tilde{h}(b) = 1$. Here we have chosen to satisfy the $\tilde{h}(b)$ boundary condition and neglected the $\tilde{h}_{\tilde{x}}(b)$ boundary condition (the $\tilde{h}_{\tilde{x}}(0) = 0$ boundary condition is automatically satisfied by the equation). With some rearrangement we get

$$\tilde{h}_{high\ Bo_d} = \left(\frac{1}{b}\right)^{A/2\,Bo_d} Exp\left(\frac{A}{4\,Bo_d}\,(\tilde{x}^2 - 1)\right) \quad (\,0 \le \tilde{x} \le 1) \tag{5-83}$$

$$\tilde{h}_{high\ Bo_d} = \left(\frac{\tilde{x}}{b}\right)^{A/2\,Bo_d} \qquad (1 < \tilde{x} \le b). \tag{5-84}$$

Combining equations (5-83) and (5-84), we write

$$\begin{aligned}\tilde{h}_{high\ Bo_d} &= \left(\frac{1}{b}\right)^{A/2\,Bo_d} Exp\left(\frac{A}{4\,Bo_d}\,(\tilde{x}^2 - 1)\right) \mathrm{H}(1 - \tilde{x}) \\ &\quad + \left(\frac{\tilde{x}}{b}\right)^{A/2\,Bo_d} \mathrm{H}(\tilde{x} - 1).\end{aligned} \tag{5-85}$$

The high Bo_d case also has a simplified expression for velocity. Equation (5-35) is simplified to

$$\tilde{v}_{high\ Bo_d} = -Bo_d\ \frac{\tilde{h}_{\tilde{x}}}{\tilde{h}^2}. \tag{5-86}$$

Referring to equations (5-79) and (5-80) we get

$$\tilde{v}_{high\ Bo_d} = -A\ \frac{\tilde{x}}{2\ \tilde{h}} \quad (0 \le \tilde{x} \le 1) \tag{5-87}$$

$$\tilde{v}_{high\ Bo_d} = -A\ \frac{1}{2\ \tilde{h}\ \tilde{x}} \qquad (1 < \tilde{x} \le b). \tag{5-88}$$

Combining equations (5-87)and (5-88), we write

$$\tilde{v}_{high\ Bo_d} = -A\ \frac{1}{2\ \tilde{h}} \left(\tilde{x}\ \mathrm{H}(1-\tilde{x}) + \frac{\mathrm{H}(\tilde{x}-1)}{\tilde{x}} \right). \tag{5-89}$$

Exact solutions, approximate solutions, and discussion

The differential equations (5-45) and (5-71) were solved numerically in Matlab using the boundary value problem solver "bvp4c." The initial guess given to the solver for $\tilde{h}$ was a fourth order polynomial that satisfied $\tilde{h}_{\tilde{x}\tilde{x}\tilde{x}} = A\ \tilde{x}$ (a gross simplification of equation (5-42)) and the three boundary conditions in equations (5-72) – (5-74). There are two key variables that we plot and examine; they are

- Film height: $\tilde{h}$, that comes from solving equations (5-45) and (5-71).
- Fluid velocity: $\tilde{v}$, that comes from plugging values into equation (5-35).

Additionally, we will consider two quantities of interest:

- The surface tension term ($\tilde{h}_{\tilde{x}\tilde{x}\tilde{x}}$) and the disjoining pressure term ($Bo_d \frac{\tilde{h}_{\tilde{x}}}{\tilde{h}^4}$) from the velocity expression $\tilde{v}$ in equation (5-35). From these we will see the role and relative importance of each term in the fluid velocity.
- The ratio: $\text{ratio}_{dx:dz}$ in the Stokes equation, that comes from equation (5-52) and equation (5-78). Small values of $\text{ratio}_{dx:dz}$ mean that our solution is consistent with the $\text{l} \gg \text{h}$ assumption in our fluid dynamics equations.

We will examine how these quantities behave as functions of the evaporation rate A (equation (5-44) or (5-70)), the disjoining pressure Bond number Bo_d (equation (5-20)), and the slope at $\tilde{x} = 1$ in the contact line model φ (equation (5-48)). As mentioned previously, the expressions in the contact line model analysis (Cartesian coordinates) are valid over $0 \leq \tilde{x} \leq b$ with heating in $0 \leq \tilde{x} \leq 1$. However, for comparison to our experiment we consider only $b = 1$ in the contact line model (Cartesian coordinates). The heated patch model (cylindrical coordinates) will be examined over $0 \leq \tilde{x} \leq b$ with heating in $0 \leq \tilde{x} \leq 1$ and $b = 10$. $b = 10$ was selected as an approximation for an infinite domain. It is anticipated that when $b > 10$, the solution is independent of b. Solutions for non-zero values of φ in the contact line model are especially relevant to the traditional concept and application of convective-capillary assembly described in Section 4.2, where the thin film must eventually connect to the bulk liquid drop. The bulk liquid drop typically has a non-zero contact angle with the substrate, either due to surface

tension in the drop (as in drop-casting [78], [79]) or due to the experimental apparatus (as in dip-coating and variations on the Langmuir-Blodgett technique [74], [76], [82]).

To facilitate numerical integration, we must assign values to the evaporation rate A (equation (5-44) or (5-70)), the disjoining pressure Bond number Bo_d (equation (5-20)), and the velocity scale v_0 (equation (5-34)). Exact values are hard to nail down for some variables so we will examine ranges of values and look at the trends. The number density of a material is determined by $\rho = \rho_{\mathrm{mass}} N_A/M$ where ρ_{mass} is the mass density, N_A is Avogadro's constant, and M is the molar mass. From this we have $\rho_1 = \rho_{\mathrm{Si_3N_4}} \sim 1.48 \times 10^{28}/\mathrm{m}^3$ and $\rho_2 = \rho_{\mathrm{H_2}O} \sim 3.3 \times 10^{28}/\mathrm{m}^3$. We consider $l = 100\ \mathrm{nm} \rightarrow 1000\ \mathrm{nm}$ and $h_\infty = 20\ \mathrm{nm} \rightarrow 30\ \mathrm{nm}$ (keeping in mind that the film is not likely to be under $20\ \mathrm{nm}$ because that would cause the nanorods to spontaneously assemble by capillary force interactions). We consider the temperature in the heated imaging region to be between 60°C and 30°C (with the unheated region at room temperature) and thus $\gamma = 66.2 \times 10^{-3}\ \mathrm{N/m} \rightarrow 71.2 \times 10^{-3}\ \mathrm{N/m}$ and $\mu = 0.467 \times 10^{-3}\ \mathrm{Ns/m^2} \rightarrow 0.798 \times 10^{-3}\ \mathrm{Ns/m^2}$ [92]. The evaporation rate is estimated to be $J \approx 1\ \mathrm{nm/s} \rightarrow 100\ \mathrm{nm/s}$ (speculated as a physically reasonable range). From these values we obtain $A \approx 3 \times 10^{-9} \rightarrow 2 \times 10^{-2}$, $\mathrm{Bo_d} \approx 1 \times 10^{-3} \rightarrow 1$, and $v_0 \approx 2 \times 10^{-4}\ \mathrm{m/s} \rightarrow 1\ \mathrm{m/s}$. The contact line model (Cartesian coordinates) solution is plotted with $A = 1 \times 10^{-3} \rightarrow 1 \times 10^{-2}$, $\mathrm{Bo_d} = 1 \times 10^{-2} \rightarrow 1 \times 10^{-1}$ and $\tilde{h}_{\tilde{x}}(1) = 0$ in Figure 5-9, $\tilde{h}_{\tilde{x}}(1) = 0.58$ (30° slope) in Figure 5-10, and $\tilde{h}_{\tilde{x}}(1) = 1.73$ (60° slope) in Figure 5-11. We compare the contact line model high $\mathrm{Bo_d}$ solution to the full solution with

$A = 1 \times 10^{-3} \rightarrow 1 \times 10^{-2}$, $\mathrm{Bo_d} = 1$, and $\tilde{h}_{\tilde{x}}(1) = 0$ and also $A = 0.1 \rightarrow 1$, $\mathrm{Bo_d} = 1$, and $\tilde{h}_{\tilde{x}}(1) = 0$ in Figure 5-12. We look at the heated patch model (cylindrical coordinates) solution with $A = 1 \times 10^{-3} \rightarrow 1 \times 10^{-2}$, $\mathrm{Bo_d} = 1 \times 10^{-2} \rightarrow 1 \times 10^{-1}$ and $\tilde{h}_{\tilde{x}}(10) = 0$ in Figure 5-13. We compare the heated patch model high $\mathrm{Bo_d}$ solution to the full solution with $A = 1 \times 10^{-3} \rightarrow 1 \times 10^{-2}$, $\mathrm{Bo_d} = 1$, and $\tilde{h}_{\tilde{x}}(10) = 0$ in Figure 5-14.

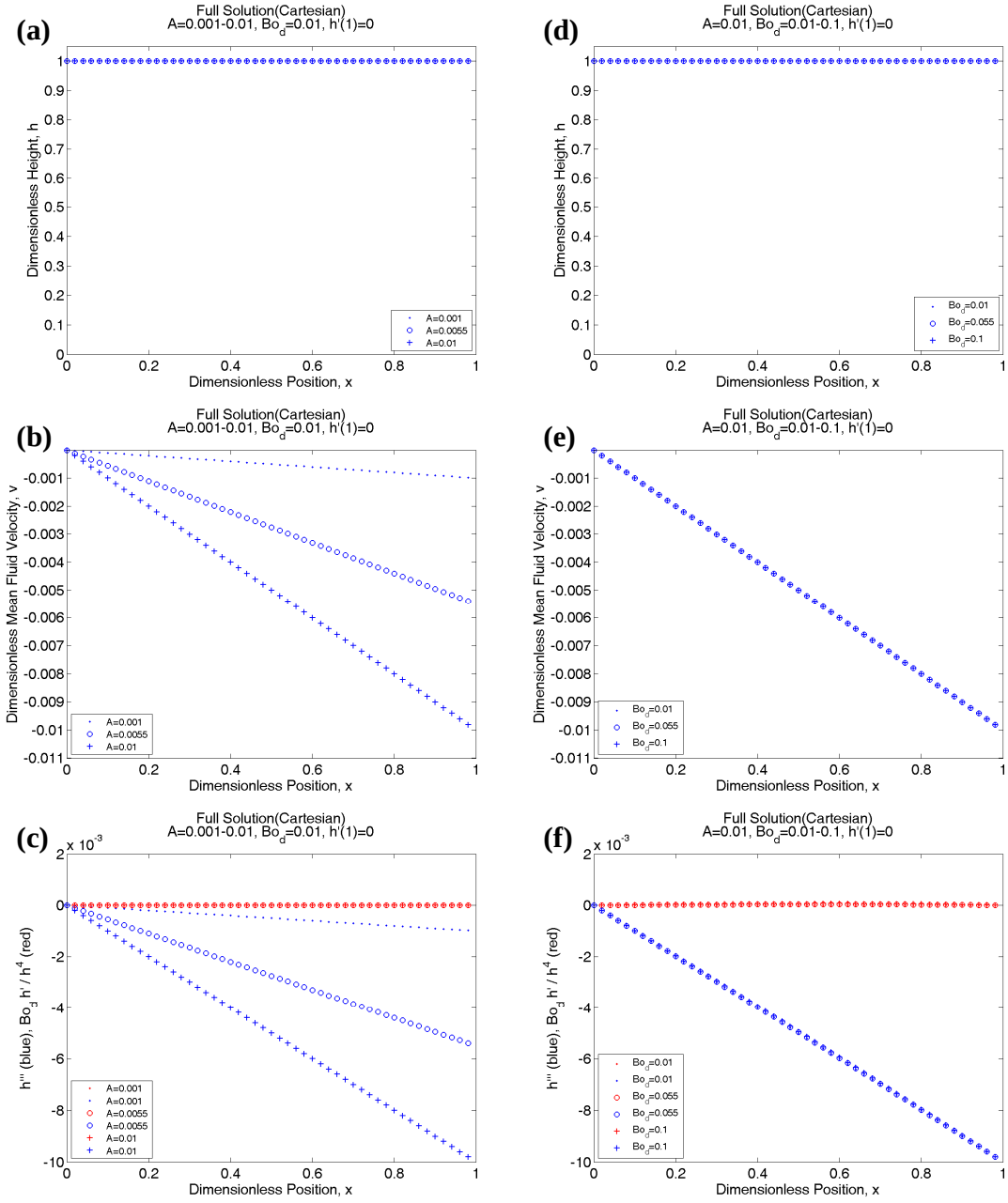

Figure 5-9: Solutions to contact line model (Cartesian coordinates) with $\widetilde{h}_{\widetilde{x}}(1) = 0$ (0° slope). (a) & (d) $\widetilde{h}$: film height. (b) & (e) $\widetilde{v}$: fluid velocity. (c) & (f) The surface tension term ($\widetilde{h}_{\widetilde{x}\widetilde{x}\widetilde{x}}$) (blue) and the disjoining pressure term ($Bo_d \frac{\widetilde{h}_{\widetilde{x}}}{\widetilde{h}^4}$) (red) from $\widetilde{v}$. Plots (a), (b), and (c) fix $\mathbf{Bo_d}$ (1×10^{-2}) and vary A $(1 \times 10^{-3} \rightarrow 1 \times 10^{-2})$, while plots (d), (e), and (f) fix A (1×10^{-2}) and vary $\mathbf{Bo_d}$ $(1 \times 10^{-2} \rightarrow 1 \times 10^{-1})$. ratio$_{dx:dz} < 2.5 \times 10^{-4}$ for all solutions.

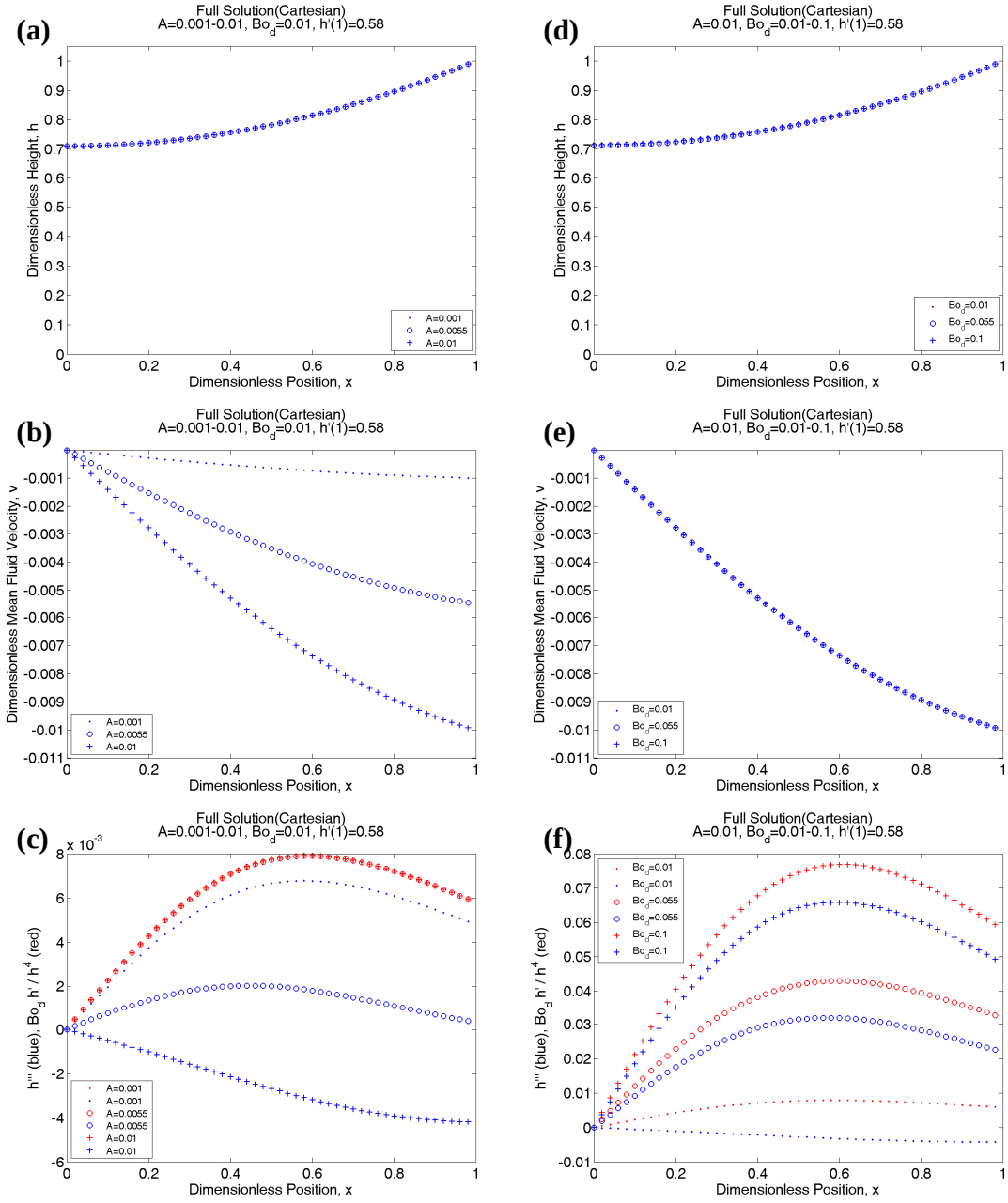

Figure 5-10: Solutions to contact line model (Cartesian coordinates) with $\widetilde{h}_{\tilde{x}}(1) = 0.58$ (30° slope). (a) & (d) $\widetilde{h}$: film height. (b) & (e) $\widetilde{v}$: fluid velocity. (c) & (f) The surface tension term ($\widetilde{h}_{\tilde{x}\tilde{x}\tilde{x}}$) (blue) and the disjoining pressure term ($Bo_d \frac{\widetilde{h}_{\tilde{x}}}{\widetilde{h}^4}$) (red) from $\widetilde{v}$. Plots (a), (b), and (c) fix $\mathbf{Bo_d}$ (1×10^{-2}) and vary A $(1 \times 10^{-3} \rightarrow 1 \times 10^{-2})$, while plots (d), (e), and (f) fix A (1×10^{-2}) and vary $\mathbf{Bo_d}$ $(1 \times 10^{-2} \rightarrow 1 \times 10^{-1})$. $\mathbf{ratio}_{dx:dz} < 6 \times 10^{-2}$ for all solutions. Note how some of the surface tension terms ($\widetilde{h}_{\tilde{x}\tilde{x}\tilde{x}}$, blue) in (c) and (f) are opposite in sign (some became positive) or are shifting towards the x-axis compared to the corresponding plots in Figure 5-9.

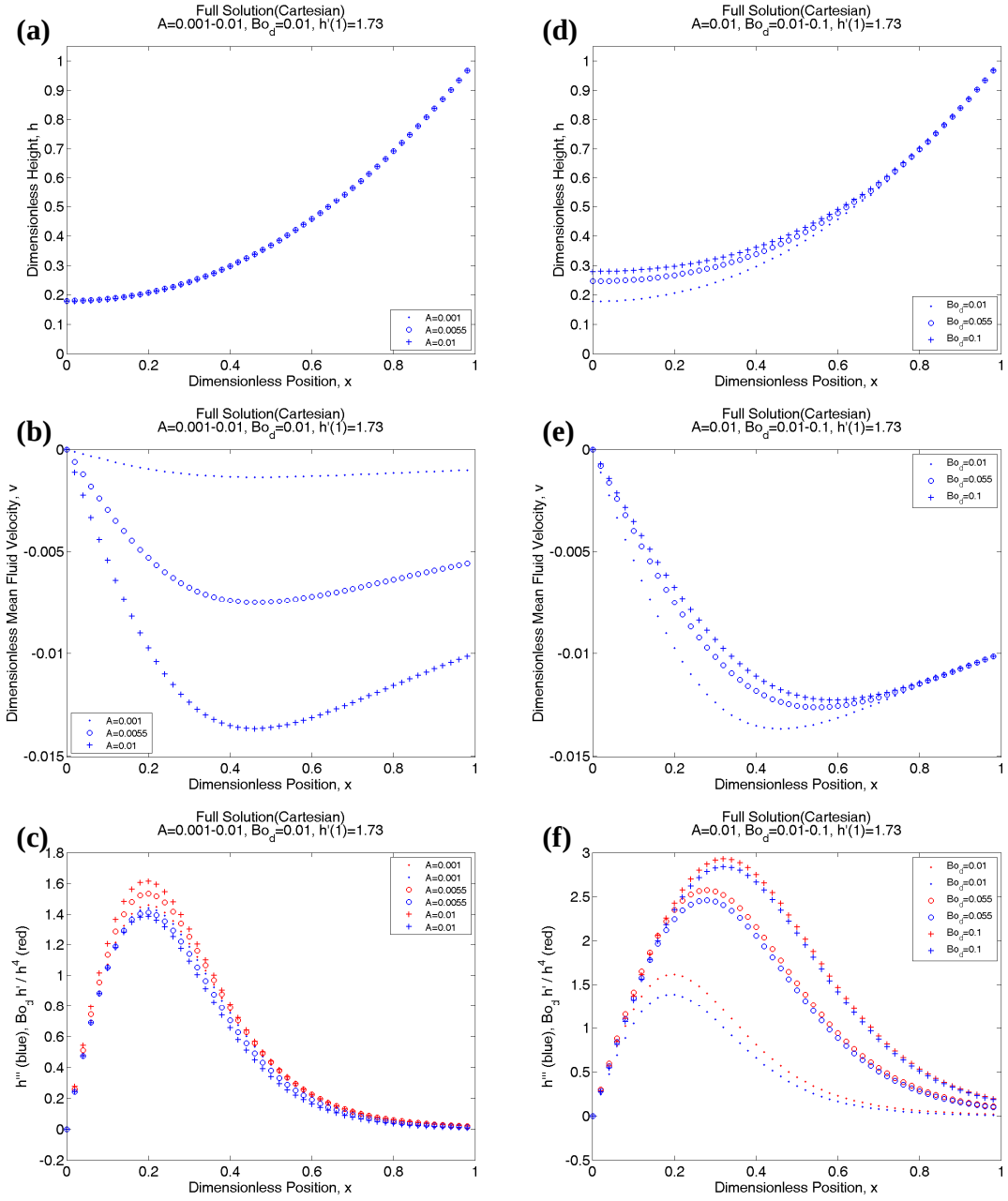

Figure 5-11: Solutions to contact line model (Cartesian coordinates) with $\widetilde{h}_{\tilde{x}}(1) = 1.73$ (60° slope). (a) & (d) $\widetilde{h}$: film height. (b) & (e) $\widetilde{v}$: fluid velocity. (c) & (f) The surface tension term ($\widetilde{h}_{\tilde{x}\tilde{x}\tilde{x}}$) (blue) and the disjoining pressure term ($Bo_d \frac{\widetilde{h}_{\tilde{x}}}{\widetilde{h}^4}$) (red) from $\widetilde{v}$. Plots (a), (b), and (c) fix $\mathbf{Bo_d}$ (1×10^{-2}) and vary A $(1 \times 10^{-3} \rightarrow 1 \times 10^{-2})$, while plots (d), (e), and (f) fix A (1×10^{-2}) and vary $\mathbf{Bo_d}$ $(1 \times 10^{-2} \rightarrow 1 \times 10^{-1})$. ratio$_{dx:dz} < 5 \times 10^{-2}$ for all solutions. Note how all of the surface tension terms ($\widetilde{h}_{\tilde{x}\tilde{x}\tilde{x}}$, blue) in (c) and (f) are opposite in sign (now positive) from the corresponding plots in Figure 5-9. Also note how the disjoining pressure term (red) overpowers the surface tension term (blue) in (c) and (f) even though Bo_d is low and we expect to be in the surface tension dominated regime.

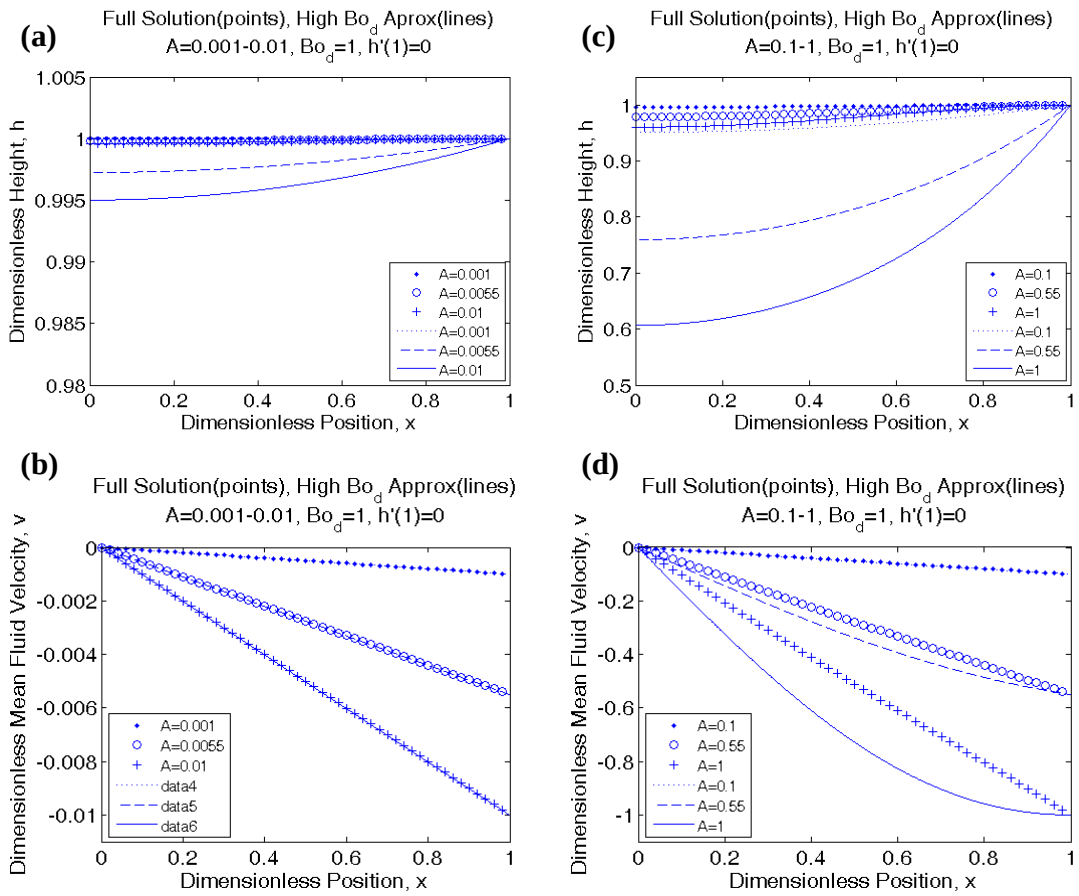

Figure 5-12: Comparison between contact line model (Cartesian coordinates) high Bo_d solution and the full solution with $\widetilde{h}_{\tilde{x}}(1) = 0$ (0° slope). (a) & (c) $\widetilde{h}$: film height. (b) & (d) $\tilde{v}$: fluid velocity. In all plots $Bo_d = 1$. In (a) and (b), A is varied from 1×10^{-3} to 1×10^{-2} with good agreement, even though Bo_d is not that high. In (c) and (d), A is varied from 1×10^{-2} to 1 with poorer agreement. The $\widetilde{h}_{\tilde{x}}(1)$ boundary condition in the high Bo_d solution is not fixed and so the shape of the interface shifts in response to increased A. The shape of the velocity profile in (d) does not agree precisely, but the order of magnitude is correct, as is the trend.

There are many interesting features and trends in Figure 5-9 – Figure 5-12 to discuss. In the full solution to the contact line model (Cartesian coordinates) presented in Figure 5-9(a) – Figure 5-11(a), we see that when $\mathrm{Bo_d}$ is fixed, the shape of the interface remains relatively unchanged over the range of A values (evaporation rate) examined. In Figure 5-9(b) – Figure 5-11(b) we see that the velocity, $\tilde{v}$, is negative and, not surprisingly, increases in magnitude with increasing A. Recall that based on our coordinate system, negative $\tilde{v}$ signifies motion from the "bulk" liquid into the thin evaporating film. Figure 5-9 presents the full solution to the contact line model (Cartesian coordinates) with the boundary condition $\tilde{h}_{\tilde{x}}(1) = 0$ (0° slope). The velocity profile in Figure 5-9(b) appears to be nearly linear. In this plot, converting $\tilde{v}$ back into dimensional units using v_0 yields a maximum velocity ranging from about 2×10^{-6} m/s to 1×10^{-2} m/s. In Figure 5-9(c) we see that the surface tension component of the velocity, $\tilde{h}_{\tilde{x}\tilde{x}\tilde{x}}$ (in blue), is negative, which produces negative $\tilde{v}$ according to equation (5-35). The disjoining pressure component of the velocity, $Bo_d \frac{\tilde{h}_{\tilde{x}}}{\tilde{h}^4}$ (in red), is nearly zero, likely due to the $\tilde{h}_{\tilde{x}}(1) = 0$ boundary condition, moderate A values that don't deform the interface greatly, and small value of Bo_d. In Figure 5-9(d), (e) and (f) we see that for this range of A values and this boundary condition, changing the value of Bo_d does little to influence the shape of the interface or the velocity of the fluid.

Figure 5-10 presents the full solution to the contact line model (Cartesian coordinates) with the boundary condition changed to $\tilde{h}_{\tilde{x}}(1) = 0.58$ (30° slope). Some very interesting behavior emerges here. For fixed Bo_d in Figure 5-10(a), the shape of the

interface does not appear to change much as A is varied between 1×10^{-3} and 1×10^{-2}. In Figure 5-10(b), we see that the velocity, $\tilde{v}$, is negative and increases in magnitude with increasing A. We can also see that the shape of the velocity profile is not quite linear. In this plot, converting $\tilde{v}$ back into dimensional units using v_0 yields a maximum velocity ranging from about 2×10^{-6} m/s to 1×10^{-2} m/s. In Figure 5-10(c), we see that the disjoining pressure component of the velocity, $Bo_d \frac{\tilde{h}_{\tilde{x}}}{\tilde{h}^4}$ (in red), is non-zero and positive (due to boundary condition on $\tilde{h}_{\tilde{x}}$). This results in negative $\tilde{v}$ according to equation (5-35), which is to be expected. However, in Figure 5-10(c), we also see that the sign of the surface tension component of the velocity, $\tilde{h}_{\tilde{x}\tilde{x}\tilde{x}}$ (in blue), is positive for some values of A. According to equation (5-35), positive values of $\tilde{h}_{\tilde{x}\tilde{x}\tilde{x}}$ contribute to motion in the positive $\tilde{x}$ direction, which is back into the "bulk" liquid. Looking at fixed A and varied Bo_d in Figure 5-10(d) and (e) we see that the interface shape and fluid velocity do not appear to change much in response to variations in Bo_d. But in Figure 5-10(f) we see that by varying Bo_d, the values of the surface tension component (blue) and disjoining pressure component (red) of $\tilde{v}$ do in fact change. Yet in every case the disjoining pressure term beats out the surface tension term by what must be the same difference to produce nearly the same $\tilde{v}$ in Figure 5-10(e). This is quite surprising because at these low values of Bo_d we expect to be in the surface tension-dominated regime, where the properties of the liquid interface should be dictated by surface tension effects alone, with little influence from the disjoining pressure body force. Looking again at Figure 5-10(d) and (e) one might be tempted to conclude that this is still a valid generalization because even

though the disjoining pressure component of $\tilde{v}$ beats out the surface tension component of $\tilde{v}$ in Figure 5-10(f), it is of no consequence to the interface shape and the fluid velocity, and therefore the value of Bo_d is indeed unimportant. This notion is disproved by Figure 5-11.

Figure 5-11 presents the full solution to the contact line model (Cartesian coordinates) with the boundary condition changed to $\tilde{h}_{\tilde{x}}(1) = 1.73$ (60° slope). Here we see more interesting behavior emerging. For fixed Bo_d in Figure 5-11(a), the shape of the interface does not appear to change much as A varies. In Figure 5-11(b), we see that the velocity, $\tilde{v}$, is negative and increases in magnitude with increasing A. Interestingly, the velocity profile has developed a hump, such that the maximum velocity is no longer at the boundary. In this plot, converting $\tilde{v}$ back into dimensional units using v_0 yields a maximum velocity ranging from about 2.8×10^{-6} m/s to 1.4×10^{-2} m/s. In Figure 5-11(c), as seen previously in Figure 5-10(c), the disjoining pressure component of the velocity, $Bo_d \frac{\tilde{h}_{\tilde{x}}}{\tilde{h}^4}$ (in red), is non-zero and positive (due to boundary condition on $\tilde{h}_{\tilde{x}}$), which results in negative $\tilde{v}$, as expected. The surface tension component of the velocity, $\tilde{h}_{\tilde{x}\tilde{x}\tilde{x}}$ (in blue), is positive for all values of A examined. According to equation (5-35), again, positive values of $\tilde{h}_{\tilde{x}\tilde{x}\tilde{x}}$ mean that surface tension is working to drive fluid in the positive $\tilde{x}$ direction, back into the "bulk" liquid. Another interesting effect appears in Figure 5-11(c), which is that even though Bo_d is fixed, the disjoining pressure component of $\tilde{v}$ changes with changing value of A. This is due to the disjoining pressure component's functional dependence on $\tilde{h}$ and $\tilde{h}_{\tilde{x}}$ (i.e., $Bo_d \frac{\tilde{h}_{\tilde{x}}}{\tilde{h}^4}$). Even slight changes in $\tilde{h}$

can have magnified consequences for the disjoining pressure component of $\tilde{v}$ due to the $1/\tilde{h}^4$ dependence. Looking at fixed A and varied Bo_d in Figure 5-11(d) and (e) we see that the interface shape and fluid velocity now change in response to Bo_d. In response to increased Bo_d, the film height, $\tilde{h}$, rises at the boundary $\tilde{x} = 0$. This makes sense since increased Bo_d means increased disjoining pressure body force, which seeks to make the liquid film level. Lower values of Bo_d result in lower $\tilde{h}$ at the boundary, which has the effect of amplifying $\tilde{v}$ in Figure 5-11(e) by driving the fluid through what is essentially a smaller nozzle. In Figure 5-11(f) we see that by varying Bo_d, the surface tension component (blue) and disjoining pressure component (red) of the disjoining pressure component of $\tilde{v}$ change, and in every case the disjoining pressure beats out surface tension. Again, this surprising because Bo_d is small (< 1) and we should expect to be in the surface tension-dominated regime. Yet Figure 5-11 shows us that even at small Bo_d, film height and fluid velocity are both sensitive to the value of Bo_d and it is the effect of disjoining pressure, not the surface tension, that drives flow from the "bulk" liquid into the thin film.

In order to explore the unexpected behavior observed in Figure 5-9 – Figure 5-11, we determine when the surface tension component of $\tilde{v}$ (i.e., $\tilde{h}_{\tilde{x}\tilde{x}\tilde{x}}$ in equation (5-35)) changes sign. Let us consider only the domain $0 \leq \tilde{x} \leq 1$. The direction in which surface tension-driven flow acts is determined by the sign of $\tilde{h}_{\tilde{x}\tilde{x}\tilde{x}}$, given by equation (5-45) for the contact line model (Cartesian coordinates). Factoring and rearranging this expression allows us to write

$$\tilde{h}_{\tilde{x}\tilde{x}\tilde{x}} = Bo_d \, \frac{\tilde{h}_{\tilde{x}}}{\tilde{h}^4}\left(1 - \frac{A\,\tilde{x}\,\tilde{h}}{Bo_d\,\tilde{h}_{\tilde{x}}}\right) \overset{?\ ?\ ?}{<=>} 0\,, \tag{5-90}$$

the sign of which is determined by the term in parenthesis. We can also determine criteria for whether the disjoining pressure component of $\tilde{v}$ (i.e., $-Bo_d \, \frac{\tilde{h}_{\tilde{x}}}{\tilde{h}^4}$ in equation (5-35)) or the surface tension component of $\tilde{v}$ (i.e., $\tilde{h}_{\tilde{x}\tilde{x}\tilde{x}}$ in equation (5-35)) dominates the flow. It should be noted that any non-zero value of the disjoining pressure component of $\tilde{v}$ will always be negative and therefore always act in the direction from the "bulk" into the thin film. Taking the ratio of the disjoining pressure component to the surface tension component and taking the absolute value we find that the dominant component is determined by the magnitude of the following expression

$$\left|\frac{1}{1 - \frac{A\,\tilde{x}\,\tilde{h}}{Bo_d\,\tilde{h}_{\tilde{x}}}}\right| \overset{?\ ?\ ?}{<=>} 1\,. \tag{5-91}$$

Examining equation (5-90) and equation (5-91) we see that the same group of terms, $\frac{A\,\tilde{x}\,\tilde{h}}{Bo_d\,\tilde{h}_{\tilde{x}}}$, appears in both expressions. The same analysis can be performed for the heated patch model (cylindrical coordinates) to find that the group of terms, $\frac{A\,\tilde{x}\,\tilde{h}}{2\,Bo_d\,\tilde{h}_{\tilde{x}}}$, appears.

We evaluate this group of terms with $\tilde{x} = 1$, $\tilde{h} = 1$, which in a typical convective capillary assembly (drop casting) process, would be the location where the precursor film meets the bulk drop (with an associated traditional contact angle providing a known value for $\tilde{h}_{\tilde{x}}$). $\tilde{x} = 1$, $\tilde{h} = 1$ is exactly correct for the contact line model (Cartesian coordinates) and a reasonable approximation ($\tilde{h} \sim 1$) for the heated patch model (cylindrical

coordinates) with moderate evaporation rate, A (discussed later in regards to Figure 5-13). We define a critical dimensionless number

$$CD = \frac{A}{\lambda\, Bo_d\, \tilde{h}_{\tilde{x}}(1)} = \frac{6\,\mu\, l^2\, J}{\lambda\, \pi\, C\, \rho_1\, \rho_2\, \tilde{h}_{\tilde{x}}(1)}, \tag{5-92}$$

where $\lambda = 1$ for Cartesian coordinates and $\lambda = 2$ for cylindrical coordinates. The value of CD determines the dominant component of fluid velocity (disjoining pressure or surface tension) as well as the direction in which the surface tension component of flow acts. The behavior of the system for various values of CD is presented in Table III. Whereas traditionally it is simply the Bond number that determines whether the body force (disjoining pressure) or surface tension dominates, we see that at the vapor-solid-liquid interface at the edge of a drop, the dominant hydrodynamic force is determined by a combination of Bond number, evaporation rate, and slope of the interface.

Figure 5-12 provides a comparison of the high Bo_d analytical solution in equation (5-59) to the full solution that comes from solving equation (5-45) numerically. In Figure

TABLE III

INFLUENCE OF THE CRITICAL DIMENSIONLESS NUMBER ON FLOW

$\boldsymbol{CD = \frac{A}{\lambda\, Bo_d\, \tilde{h}_{\tilde{x}}(1)}}$	**Disjoining pressure vs. surface tension**	**Direction of disjoining pressure flow**	**Direction of surface tension flow**
$CD = 0$	Tie	Into thin film	Into bulk
$0 < CD < 1$	Disjoining pressure dominates	Into thin film	Into bulk
$CD = 1$	Disjoining pressure dominates	Into thin film	No flow
$1 < CD < 2$	Disjoining pressure dominates	Into thin film	Into thin film
$CD = 2$	Tie	Into thin film	Into thin film
$2 < CD$	Surface tension dominates	Into thin film	Into thin film

5-12(a) and (b), we see that for $Bo_d = 1$, there is good agreement between the high Bo_d solution and the full solution with $\tilde{h}_{\tilde{x}}(1) = 0$ over the range of A considered ($A = 1 \times 10^{-3} \rightarrow 1 \times 10^{-2}$). In Figure 5-12(c) and (d), the range for A is shifted two orders of magnitude to $A = 0.1 \rightarrow 1$, while maintaining $Bo_d = 1$ for both solutions and $\tilde{h}_{\tilde{x}}(1) = 0$ for the full solution. We see here that agreement between the high Bo_d solution and the full solution degrades in response to the increased evaporation rate, A. In Figure 5-12(c) we see that the profile of the film height in the full solution decreases slightly as a result of the increased evaporation rate, though the $\tilde{h}_{\tilde{x}}(1) = 0$ boundary condition is maintained. The high Bo_d solution lacks any constraint on $\tilde{h}_{\tilde{x}}(1)$, and so in Figure 5-12 (c) we see the film height in the high Bo_d solution shifting more dramatically than in its full solution counterpart. The high Bo_d solution is unable to maintain the $\tilde{h}_{\tilde{x}}(1) = 0$ boundary condition specified in the full solution because we threw out the $\tilde{h}_{\tilde{x}\tilde{x}\tilde{x}}$ term and in doing so we lost the ability to specify three boundary conditions. As a consequence, the velocity profiles in Figure 5-12(d) disagree as well because of the nozzle effect that the decreased film height has on the high Bo_d solution for $\tilde{v}$. While the agreement between velocity predictions is not exact, the order of magnitude does agree well, along with the general trend. If one wanted to simply calculate the maximum velocity for this set of parameters then the high Bo_d solution would be acceptable. Looking again at the high Bo_d solution in Figure 5-12(a), if the boundary condition $\tilde{h}_{\tilde{x}}(1)$ on the full solution had been something other than zero (perhaps $\tilde{h}_{\tilde{x}}(1) = 0.58$ as in Figure 5-10), then it is clear that the high Bo_d solution would fail to capture this feature. So the high Bo_d

solution is capable of representing the full solution, but only if the value of $\tilde{h}_{\tilde{x}}(1)$ in the high Bo_d solution, which is free to change in response to system parameters A and Bo_d, happens to be close to the specified $\tilde{h}_{\tilde{x}}(1)$ boundary condition in the full solution.

Let us examine these results for the contact line model (Cartesian coordinates) in light of the observations of particles at the contact line reported on in Section 4.3. We see from Figure 5-9 – Figure 5-11 that evaporation from the thin liquid film produces pressure gradients and subsequent fluid motion directed in the minus $\tilde{x}$ direction from the "bulk" liquid ($\tilde{x} = 1$) into the thin film ($\tilde{x} = 0$). We also see that the boundary condition $\tilde{h}_{\tilde{x}}(1)$ has a significant impact on the velocity profile in the liquid film. As the slope $\tilde{h}_{\tilde{x}}(1)$ increases, the velocity profile develops a hump such that the maximum lies somewhere in the domain, not at the boundary. In subsection 5.2.1 we established that the intermolecular forces between nanoparticles and the surface must be greater than thermal energy, as evidenced by the muted diffusivity of particles. Particles were therefore stuck to the surface. If we consider that in a situation such as this there is likely a threshold force for motion, above which a particle that is stuck to the surface will move, then we have a good explanation for the delayed particle motion that was described in Section 4.3 and pictured in Figure 4-7. The conditions were likely such that the velocity profile in the thin film looked something like that in Figure 5-11(b) and (e). As the contact line passed over a particle, the particle remained stuck to the surface because the force experienced by the particle did not meet the threshold force needed to dislodge it. As the contact line continued to move past the fixed particle, the velocity profile in the fluid also moved in the positive $\tilde{x}$ direction relative to the fixed particle. The particle experienced an increase

in force (as depicted by the velocity profile in Figure 5-11(b) and (e)) until the force on the particle exceeded the threshold force necessary to dislodge it and the particle shot out in the negative $\tilde{x}$ direction. The particle eventually came to rest again after moving out in the negative $\tilde{x}$ direction to the point where the force from the fluid was insufficient to move the particle.

These results also provide a good explanation for the interesting observation that particles in the path of an advancing contact line were not engulfed by the "bulk" liquid, but were instead swept forward (see Figure 4-8 and Figure 4-9). Let's consider again that the conditions were likely such that the velocity profile in the thin film looked something like that in Figure 5-11(b) and (e). These conditions produced a high pressure front located some distance ahead of the contact line that met the threshold force for dislodging a particle. A particle that was fixed to the membrane at a position far from the contact line (e.g., near $\tilde{x} = 0$) experienced relatively little force and remained at its location. As the contact line advanced, the velocity profile in the fluid moved in the minus $\tilde{x}$ direction relative to the fixed particle. The particle experienced a subsequent increase in force until the threshold force was met and the particle was pushed by the advancing contact line. It is likely that as the contact line continued to move, the particle remained at the distance from the contact line that corresponded to the threshold force for dislodging the particle.

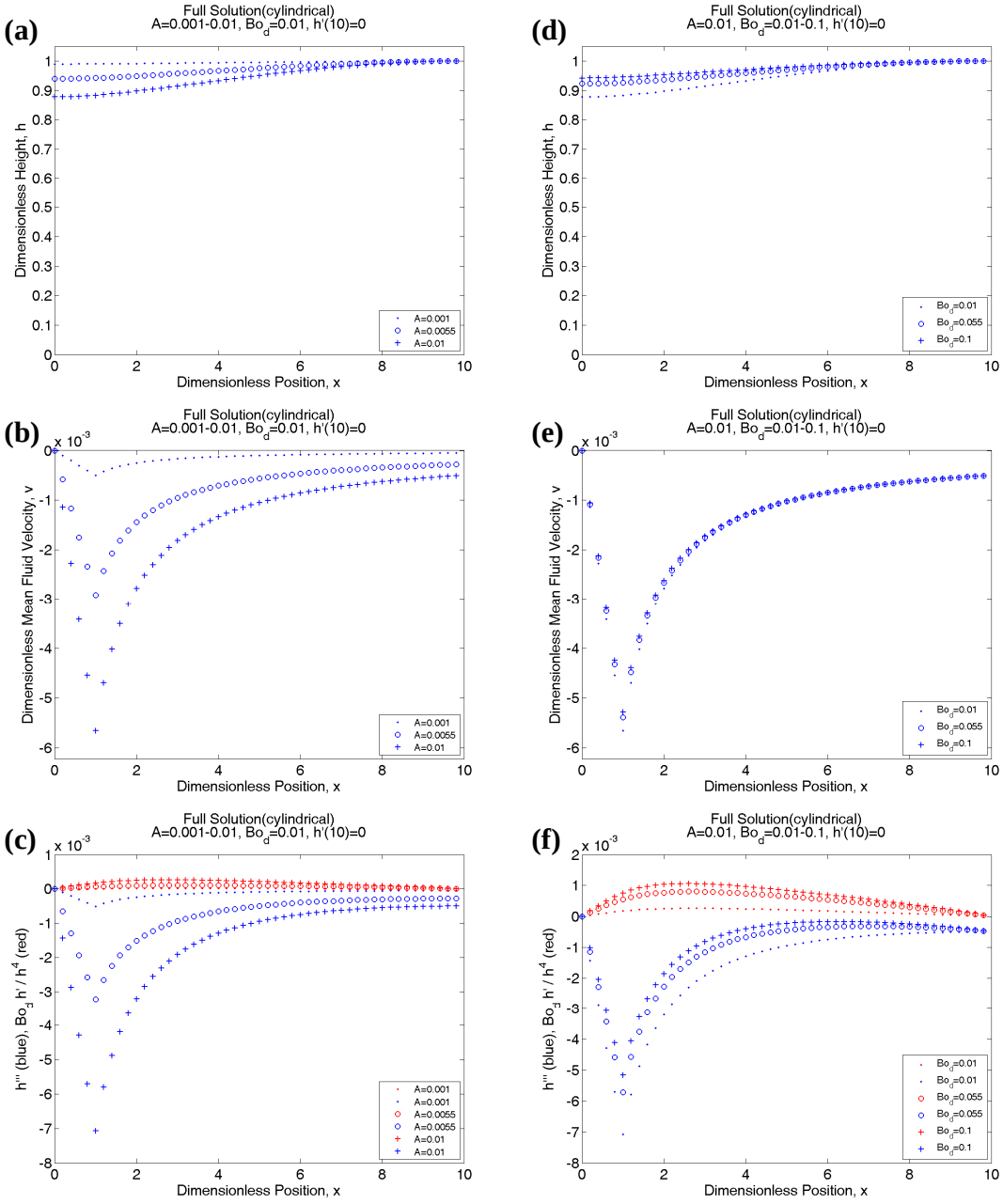

Figure 5-13: Solutions to heated patch model (cylindrical coordinates) with $\widetilde{h}_{\widetilde{x}}(10) = 0$ (0° slope). (a) & (d) $\widetilde{h}$: film height. (b) & (e) $\widetilde{v}$: fluid velocity. (c) & (f) The surface tension term ($\widetilde{h}_{\widetilde{x}\widetilde{x}\widetilde{x}}$) (blue) and the disjoining pressure term ($Bo_d \frac{\widetilde{h}_{\widetilde{x}}}{\widetilde{h}^4}$) (red) from $\widetilde{v}$. Plots (a), (b), and (c) fix $\mathbf{Bo_d}$ (1×10^{-2}) and vary A $(1 \times 10^{-3} \rightarrow 1 \times 10^{-2})$, while plots (d), (e), and (f) fix A (1×10^{-2}) and vary $\mathbf{Bo_d}$ $(1 \times 10^{-2} \rightarrow 1 \times 10^{-1})$. $\mathbf{ratio}_{dx:dz} < 2 \times 10^{-3}$. Note how velocity is highest at the edge of the heated imaging region ($\widetilde{x} = 1$), and decreases when moving away in either direction.

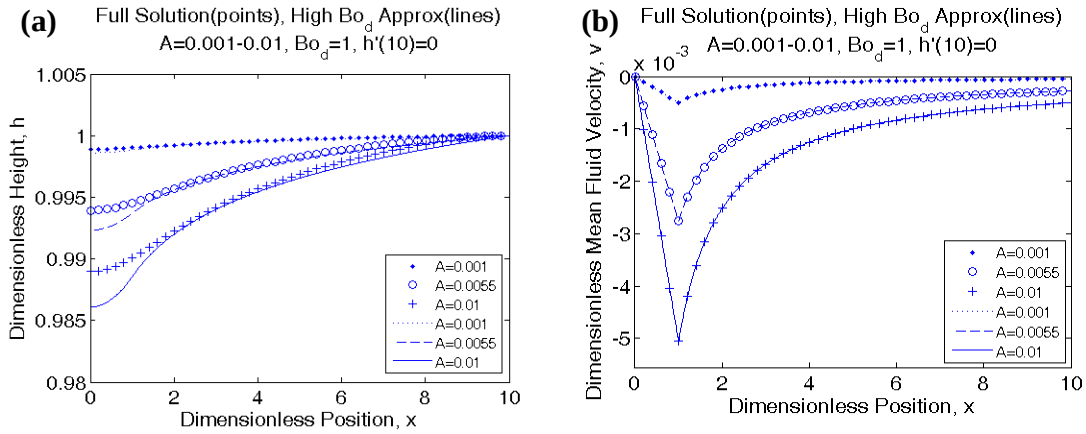

Figure 5-14: Comparison between heated patch model (cylindrical coordinates) high Bo_d solution and the full solution with $\widetilde{h}_{\tilde{x}}(10) = 0$ (0° slope). (a) & (c) $\widetilde{h}$: film height. (b) & (d) $\tilde{v}$: fluid velocity. In all plots $Bo_d = 1$ and A is varied ($1 \times 10^{-3} \rightarrow 1 \times 10^{-2}$). Agreement is good, even though Bo_d is not that high.

In Figure 5-13 we see the full solution to the heated patch model. Figure 5-13(a) shows that the film height decreases from $\tilde{h} = 1$ at the far-field to $\tilde{h} < 1$ at the origin. For fixed Bo_d, the film height decrease is more pronounced with increased evaporation rate, A. Figure 5-13(b) shows that the velocity $\tilde{v}$ is negative and increases in magnitude with increasing A. The fluid velocity reaches a maximum at the edge of the heated region, $\tilde{x} = 1$. The velocity decreases nearly linearly towards $\tilde{x} = 0$ and with nearly $1/\tilde{x}$ dependence moving towards the far-field. In this plot, converting $\tilde{v}$ back into dimensional units using v_0 yields a maximum velocity ranging from about 1.2×10^{-6} m/s to 6×10^{-3} m/s. In Figure 5-13(c) we see that the surface tension component of the velocity, $\tilde{h}_{\tilde{x}\tilde{x}\tilde{x}}$ (in blue), is negative and the disjoining pressure component of the velocity, $Bo_d \frac{\tilde{h}_{\tilde{x}}}{\tilde{h}^4}$ (in red), is positive, which means that both components work to produce negative $\tilde{v}$ according to equation (5-35). In addition, we see that the surface tension

component of $\tilde{v}$ is greater than disjoining pressure component of $\tilde{v}$ for all values of A examined. Unlike the contact line solution results discussed earlier, this is the behavior that we would expect when Bo_d is small. From Figure 5-13(a) we see that for moderate evaporation rate, A, the dimensionless film height is approximately $\tilde{h} \sim 1$ at $\tilde{x} = 1$ and our definition for the critical dimensionless number, CD (equation (5-92)), is valid. For the values of A, Bo_d, and $\tilde{h}_{\tilde{x}}(b)$ specified here, the conditions are such that $\tilde{h}_{\tilde{x}} \ll 1$ over the entire domain and CD is therefore very large (bottom row of Table III). In Figure 5-13(d) and (e), we see that for fixed A, the interface shape and fluid velocity change slightly in response to Bo_d. In response to increased Bo_d, the film height, $\tilde{h}$, rises at the boundary $\tilde{x} = 0$. As mentioned previously, this makes sense since increased Bo_d means increased disjoining pressure body force, which seeks to make the liquid film level. Decreased film height with decreased Bo_d has the effect of increasing $\tilde{v}$ because the fluid is essentially flowing through a smaller nozzle. Though present, the effect is not as dramatic here as it was in Figure 5-11(e). In Figure 5-13(f) we see that the surface tension component of the velocity, $\tilde{h}_{\tilde{x}\tilde{x}\tilde{x}}$ (in blue), is negative, and the disjoining pressure component of the velocity, $Bo_d \frac{\tilde{h}_{\tilde{x}}}{\tilde{h}^4}$ (in red), is positive for all values of Bo_d and it is the surface tension component that dominates.

Figure 5-14 provides a comparison of the high Bo_d analytical solution in equation (5-89) to the full solution that comes from solving equation (5-71) numerically. We see that even for a value of $Bo_d = 1$, there is good agreement between the high Bo_d solution

and the full solution with $\tilde{h}_{\tilde{x}}(1) = 0$ over the range of A considered ($A = 1 \times 10^{-3} \rightarrow 1 \times 10^{-2}$). The agreement improves with increased Bo_d.

Let us examine these results for the heated patch model in light of the observations of particle motion in a thin film reported on in Section 4.4 and Section 4.5. We see from Figure 5-13 that evaporation from the imaging region of the liquid film produces pressure gradients and subsequent fluid motion directed in the minus $\tilde{x}$ direction from the far-field ($\tilde{x} = b \gg 1$) into the thin film ($\tilde{x} = 0$). Fluid velocity decreases nearly linearly from its maximum at the edge of the imaging region to the origin. We see from Figure 5-13(b) that fluid velocity increases with increased evaporation rate A. Recall that Figure 4-11 – Figure 4-14 revealed an interesting relationship between the level of magnification and which particles in the field of view moved. At relatively high magnification (Figure 4-13 and Figure 4-14), nearly all of the particles in the field of view aggregated by moving towards the center of the image (minus $\tilde{x}$ direction). At relatively low magnification (Figure 4-11 and Figure 4-12) only the particle near the perimeter moved toward the center of the image, while the particles in the center of the image experienced little to no movement. At the beginning of Section 5.2 we discussed how the flux of electrons through the image, and subsequent heating and evaporation, should change with the level of magnification. Relatively speaking, low magnification translates to low flux and low evaporation rate, while high magnification translates to high flux and high evaporation rate.

With this in mind, let's imagine that the threshold force to dislodge a fixed particle corresponds to a fluid velocity of $\tilde{v} = 2 \times 10^{-3}$. Then according to Figure

5-13(b), the three plotted values for A would have three different signatures of particle motion. For $A = 0.001$, none of the particles in the domain of $0 \leq \tilde{x} \leq 1$ would experience the threshold force for motion. For $A = 0.0055$, the particles located approximately between $2/3 \leq \tilde{x} \leq 1$ would experience enough force to move. The particles would move in the minus $\tilde{x}$ direction and come to rest near $\tilde{x} \approx 2/3$, producing a result that possibly resembles Figure 4-12. For $A = 0.01$, the particles located approximately between $1/3 \leq \tilde{x} \leq 1$ would experience enough force to move. The particles would move in the minus $\tilde{x}$ direction and come to rest near $\tilde{x} \approx 1/3$, producing a result that possibly resembles Figure 4-13. This hypothetical description is meant simply to illustrate the point that the results of our model, namely a linear fluid velocity profile that decays towards the center of the image and a maximum fluid velocity that increases with increased evaporation rate, provide a convincing explanation for the observations of Section 4.4 and is in excellent agreement with the results plotted throughout Section 4.5.

Pressure Gradients and Flow Conclusion: Variations in thickness of a thin liquid film produce lateral pressure gradients in the film that are driven by gradients in the disjoining pressure and the surface tension (Laplace pressure) in the fluid. Subsequent fluid velocities can be quite significant (on the order of $1.2 \times 10^{-6}\ m/s \rightarrow 1.4 \times 10^{-2}\ m/s$*). Surprisingly, solutions to the differential equations in the contact line model (Cartesian coordinates) reveal that even for low disjoining pressure bond number* Bo_d*, it is possible to have fluid motion into the thin film region driven predominantly by the disjoining pressure effect with surface tension acting in opposition. A critical*

dimensionless number, CD, was defined that determines the direction in which surface tension drives flow and whether disjoining pressure or surface tension dominates. CD depends on evaporation rate, A, disjoining pressure Bond number, Bo_d, and slope of the interface, $\tilde{h}_{\tilde{x}}$, which when evaluated at the contact line refers to the traditional contact angle. Interesting velocity profiles were revealed that possessed a maximum located within the domain of the thin film (rather than at the boundary). If we consider that there is likely a threshold force necessary to move a particle that is resting on the membrane surface then the behavior of fluid flow arising from this phenomenon provides convincing explanations for the interesting particle motion reported in Chapter 4.

Section 5.3: Suggestions for novel nanoparticle assembly techniques

Researchers have reported on convective-capillary assembly of nanoparticles using patterned substrates [82], [86], [96], [97], along with other perturbations such as a needle dipped into the drop [98] or external electric field [99], in order to direct the shape and properties of the deposited nanocrystal. In the experiments discussed in Section 4.4, we selectively heated sections of the sample with the electron beam, which enhanced evaporation and drove aggregation through the mechanism detailed in Section 5.2. This suggests that if one could controllably enhance or suppress the evaporation rate at different locations on a sample then aggregation could be directed and patterns could be produced. Indeed, this approach to patterned self-assembly is an active field of research and is termed evaporative lithography. Harris et al. have several publications on the subject [100–102]. Typically, a mask with holes or vias with other geometries is placed

over a substrate with a liquid film containing particles. The mask suppresses evaporation in the regions without holes to produce a variation in evaporation rate across the sample. As an alternative to this approach, we suggest an apparatus illustrated in Figure 5-15. Using the modified Langmuir-Blodgett technique for assembling nanoparticles on a surface, one could adapt the apparatus to include a light pattern projected at the contact line that modifies the drying pattern through selective heating. Particles would be convected toward the regions of highest evaporation. The light pattern could be shown from either the top, or, if the substrate was transparent, the bottom. In the case of bottom-side illumination, one would want to be aware of the potential for Rayleigh–Bénard convection.

As an approach to patterning nanoparticles without the need for masks or substrate modification, recall the interesting interaction of particles with an advancing contact line described in Section 4.3. Particles that were deposited on the surface with random placement and orientation were brought into alignment by the advancing contact line. This effect could be exploited to achieve ordered deposition of nanoparticles. In the modified Langmuir-Blodgett technique used by others [74], [76], [82], a sample is withdrawn from a stationary solution or a straight edge is used to sweep a drop across a stationary sample. In either case, the process could be modified to include forward and backward steps. For example, in order to achieve orientation of anisotropic particles such as nanorods, one could move the stage in a cycle of two steps forward followed by one step backward. During the forward steps, particles would be ejected from the bulk liquid and deposited on the substrate surface. During the backward step, the advancing contact

line would serve to orient the rods parallel to the contact line (as pictured in Figure 4-8). Additionally, one could work with dilute nanoparticle solutions to produce striped depositions of nanoparticles. An illustration of the dilute nanoparticle patterning process is pictured in Figure 5-16.

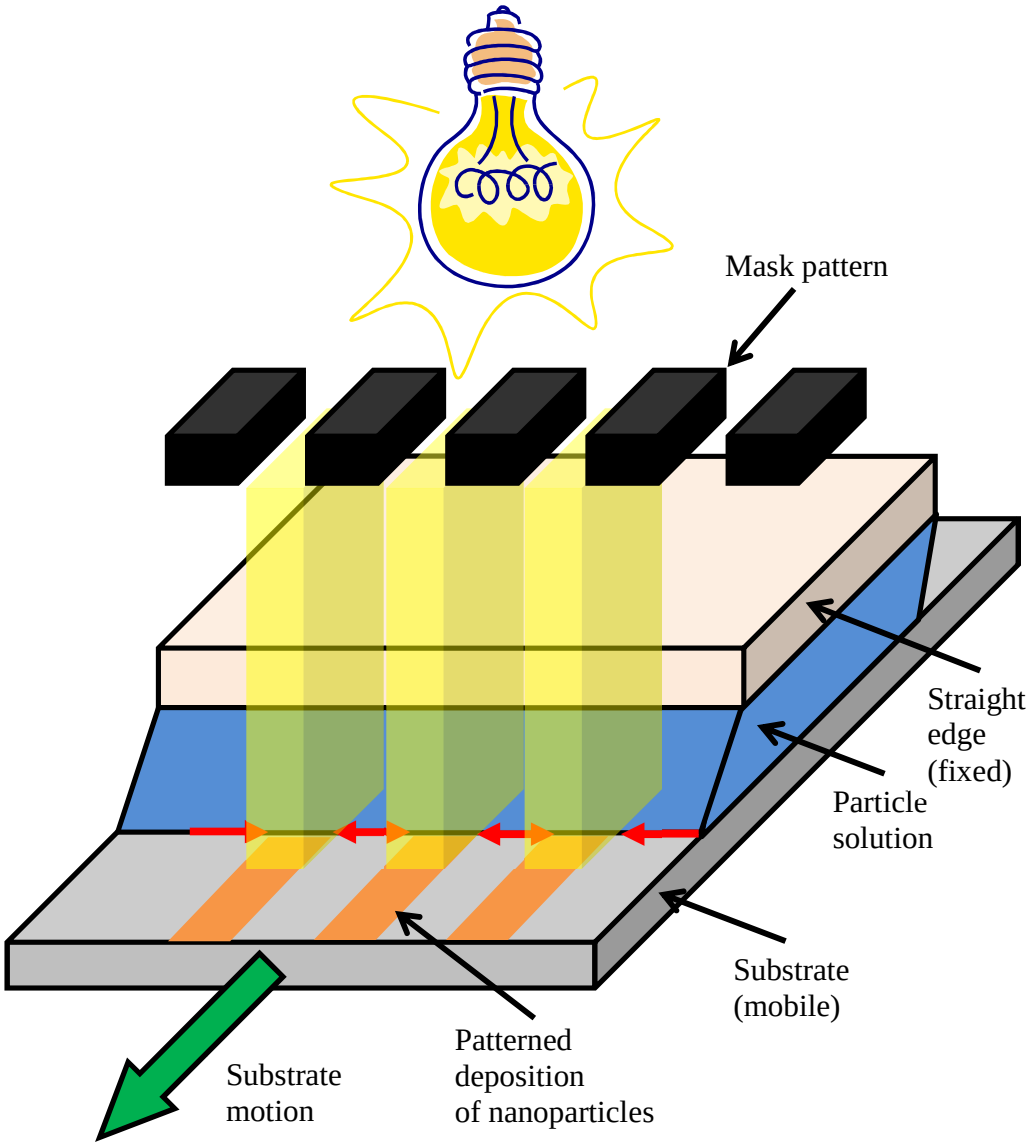

Figure 5-15: Illustration of proposed technique for patterned deposition of nanoparticles on a blank substrate. Light shined onto the sample through a photomask, or with an interference technique, would selectively heat the thin film of liquid at the contact line and drive preferential evaporation and thus convection of particles towards the heated region (indicated with red arrows).

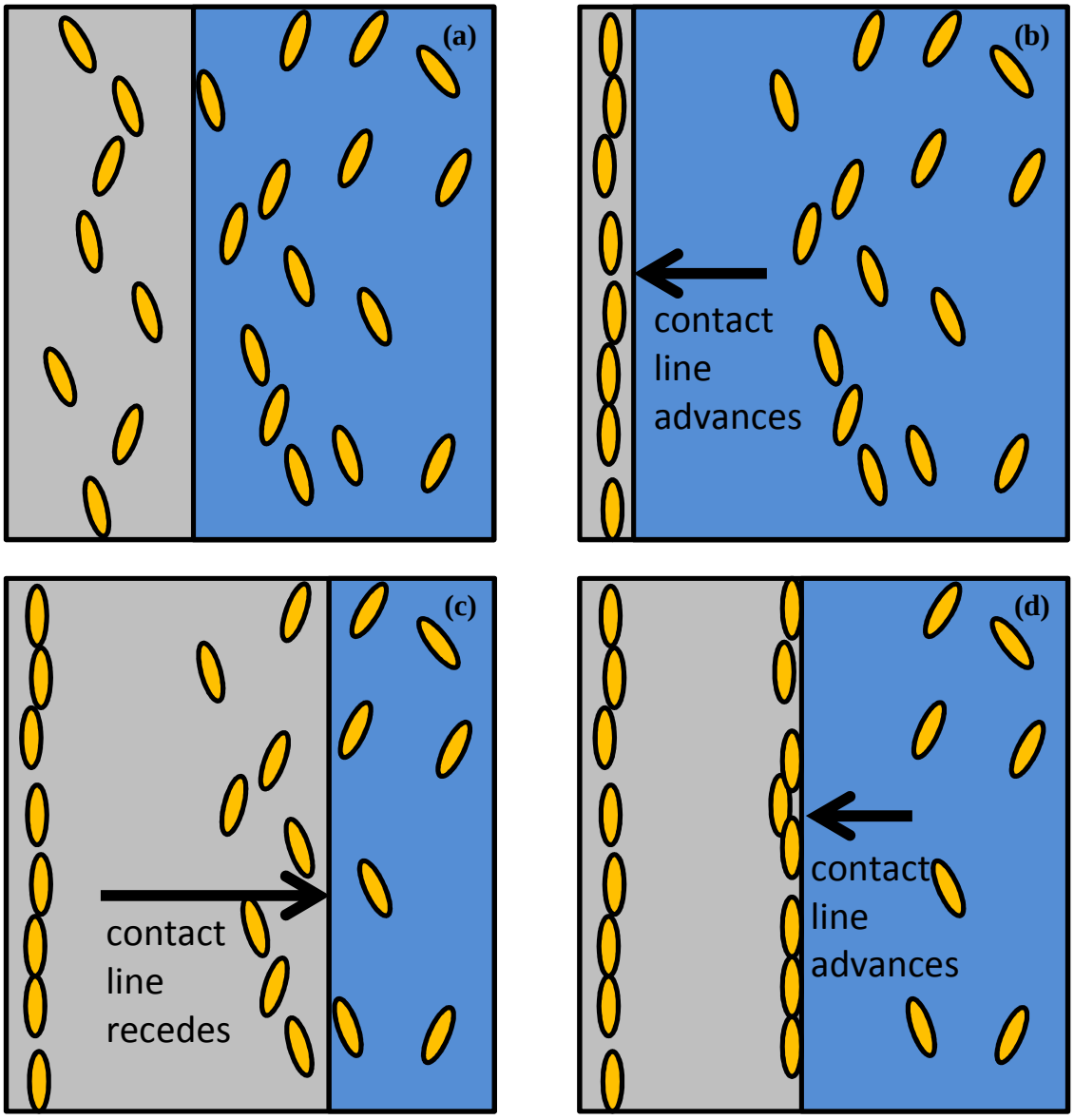

Figure 5-16: Illustration of a proposed cyclic particle deposition and alignment process for dilute nanoparticle solutions. Color coded as follows: gray (substrate), blue (solution), yellow (nanorods). (a) The substrate is withdrawn from the solution and nanoparticles are deposited. (b) The substrate is moved back into the solution, which serves to push the deposited nanorods into alignment with the contact line, all at the same location on the substrate. (c) The substrate is again withdrawn from the solution in order to deposit more particles. (d) The substrate is again moved back into the solution in order to orient and place the particles at the position of the contact line. The ratio of forward steps to backward steps could be tuned in order to control the spacing between rows of deposited nanoparticles.

Chapter 6: Conclusions and Outlook

Section 6.1: Conclusions

A nanofluidic platform, dubbed the nanoaquarium, for *in situ* TEM and STEM real-time imaging of processes in liquid media has been presented [13]. The device consists of two suspended silicon nitride membranes (50 nm thick) sandwiching a thin fluid chamber (100 nm – 400 nm) whose height is defined by the thickness of a silicon oxide spacing layer. The fabrication details, including a thorough treatment of the plasma activated wafer bonding process, were presented. The fabrication approach for the nanoaquarium offers several important advantages over other liquid-cell (S)TEM devices such as an exceptionally thin liquid height, integrated electrodes for sensing and actuation, compatibility with lab-on-chip technology, and wafer level processing to enable mass production of identical, inexpensive devices. Also, the selection of materials used in construction of the nanoaquarium makes it possible to use the device to study systems with harsh chemistries (acids, bases, strong solvents), which isn't possible in many of the similar device that use materials such as glue, epoxy, or indium for sealing.

Device utility was verified using aqueous suspensions of gold and polystyrene nanoparticles. Motion of gold particles in solution was observed using a FEI Quanta 600 FEG Mark II scanning electron microscope with STEM detector (20 kV – 30 kV acceleration voltage). The device provided high contrast images of nanoparticles suspended in liquid and allowed monitoring of particle motion and aggregation. It should be noted that the volume of solution needed in the experiment was very small (< 3 μL), making this an appealing technique when samples are scarce. The hermeticity of the

device was excellent; the device was effectively leak-proof, both in the vacuum chamber of the microscope for periods of hours, and at room conditions for periods of days. The membranes of the viewing window of the nanoaquarium were found to deform and bow outward due to pressurization of the internal fluid when the device was clamped in its holder. The interaction of light with the stack of materials in the viewing window of the device was modeled, providing a means to estimate membrane deformation. By counting the interference rings visible with a light microscope, the shape of the bowed membrane was approximated and used as a means to estimate the internal pressure of the fluid.

Kinetics of colloid aggregation was studied [50]. We observed the motion and interactions of particles in liquid media in real time with nanoscale resolution, allowing us to gather information which cannot be obtained with any other technique. Our experiments provide a level of detail that previously could be afforded only by numerical simulations. To obtain similar information with frozen samples would be at best extremely tedious and at worst impossible. Process kinetics and fractal dimension of the aggregates are consistent with three-dimensional cluster-cluster diffusion-limited aggregation. The data collected with the nanoaquarium is consistent with prior observations obtained by other means [51–54], [69]. This is an important finding for establishing *in situ* liquid-cell (S)TEM as an experimental technique that can produce meaningful results free from artifacts associated with the measurement technique/apparatus. We also observed and explained an interesting growth regime in which large aggregates grown in a shallow nanochannel were found to possess fractal characteristics consistent with three-dimensional growth, despite the expectation of

confinement effects. This apparent paradox was resolved through *in situ* observations of the interactions between individual particles and clusters at various stages of the aggregation process that yielded the large aggregates. It was found that individual particles and small clusters initially aggregated in a nearly three-dimensional environment until the clusters grew large enough that movement was confined by the nanochannel and only lateral movement was permitted. These clusters aggregating in a two-dimensional environment already possessed characteristics of three-dimensional growth and the characteristics were preserved in the resulting large clusters.

For the first time, using electron microscopy, the behavior of nanoparticles at the contact line and in an evaporating thin film of liquid was investigated. In both cases, particles were stuck to the silicon nitride surface. With a receding contact line, particles were propelled from the "bulk" liquid into the thin liquid film, though often not until the contact line had receded past the particle by some distance. With an advancing contact line, particles were not engulfed by the "bulk" liquid, but were instead pushed forward, maintaining a separation distance from the contact line. Away from the contact line, particles in the thin liquid film remained stably dispersed on the silicon nitride surface until they were imaged by the electron beam, at which point the particles in the field of view aggregated towards the center of the image. As the magnification of the image increased, so did the rate of aggregation and the proportion of particles that participated in the aggregation process. The underlying physics that drove these processes was modeled by considering the effect of disjoining pressure and surface tension on the pressure field in the fluid. An explanation for the phenomena was provided based on an

elevated evaporation rate due to heating from the electron beam in the imaging region. This caused variations in the thickness of the thin liquid film, which created lateral pressure gradients due to gradients in the surface tension and the disjoining pressure of the liquid film, both of which depend on the shape of the liquid-vapor interface. An unexpected result of the model showed that even for low disjoining pressure Bond number, a regime in which the surface tension force is expected to dominate the disjoining pressure body force, the disjoining pressure can overpower the surface tension when certain conditions are met. Criterion was identified, in the form of a critical non-dimensional number, which determines whether the surface tension or the disjoining pressure dominates fluid flow, and whether the surface tension effect drives flow into or out of the thin film. The critical non-dimensional number depends on the evaporation rate of the liquid, the disjoining pressure Bond number, and slope of the interface (which for a droplet is governed by the traditional contact angle). Insight into the behavior of particles at the edge of a drop and in thin films was gained through this analysis. Additionally, novel nanoparticle assembly techniques inspired by the results of the investigation were discussed.

Section 6.2: Outlook

As mentioned in the introduction, there are numerous applications for a liquid-cell such as the nanoaquarium for *in situ* electron microscopy of nanoscale phenomena in liquid media. Examples include aggregation, colloidal crystal formation, liquid phase growth of structures such as nanowires, electrochemical deposition and etching of

materials for fabrication processes as well as battery applications, interfacial phenomena, boiling and cavitation, and biological interactions. Let us briefly discuss some of these future applications.

6.2.1: Aggregation and colloidal crystal formation

This is a vast field of research that includes a variety of phenomena and techniques in addition to the two topics explored in this dissertation (diffusion limited aggregation and convective-capillary assembly at the contact line). Additional topics include assembly of nanoparticles under the influence of external fields, such as electric field, thermal gradient, or concentration gradient. Assembly under various processing conditions such as elevated temperature (via resistive heaters) or elevated pressure can be explored. It was determined in Section 2.10 and Section 4.1 that the membrane windows can sustain significant internal fluid pressure without rupture.

The gold particles used in the diffusion limited aggregation study herein (Chapter 3) were amorphous in structure, but by using particles with crystallographic structure one can perform an interesting solution-based self-assembly process called oriented attachment (OA). In OA, the assembly process does not simply depend on the probability of particles colliding, but also includes the relative crystallographic orientation of particles as a factor in determining the probability and strength of binding. Penn and Banfield first suggested that OA was a dominant growth mechanism in the early stages of certain crystal growth processes, providing a pathway for direct combination of nanoparticles to form fascinating aggregate structures [66], [67]. Experimental evidence for OA has been reported by many researchers in the form of irregular, anisotropic

nanocrystal structures such as chains, butterflies, horseshoes, and other odd shapes clearly comprised of individual nanoparticle building blocks that stuck together with preferred orientation [64], [65], [103–108]. Additionally, crystal defects such as dislocations, twins, stacking faults, and misorientation in these structures imply direct coalescence of seed nanoparticles [56], [63]. The OA process, however, has not been observed *in situ*, and the ability to observe single binding events between nanoparticles would be a powerful capability for exploring and understanding this phenomenon. The nanoaquarium has been used to observe single binding events between anisotropic 50 nm gold particles in water as pictured in Figure 6-1. In this experiment, gold particles were confined in the ~100 nm tall liquid chamber and were often stuck to the top or bottom membrane. Occasionally, however, a particle would break free from the membrane surface and diffuse randomly, sometimes exiting the field of view, sometimes entering the field of view, and sometimes colliding with another particle to form a cluster as

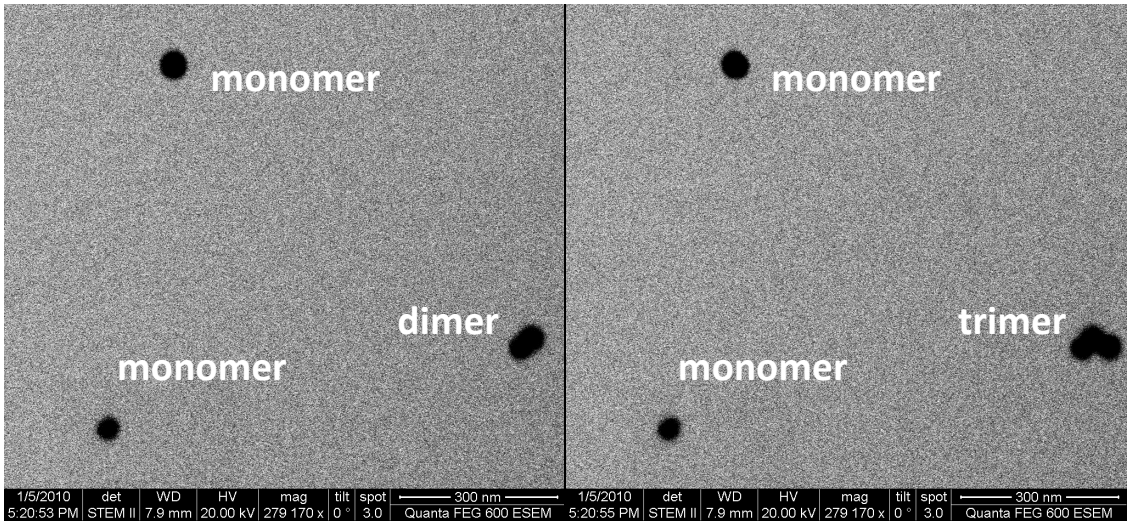

Figure 6-1: A single binding event in a system of 50 nm amorphous gold particles in water. In the first frame, two monomers and a dimer are present. In the following frame, the dimer has become a trimer by addition of a single particle.

illustrated in Figure 6-1. The nanoaquarium would thus be useful for investigating the oriented attachment self-assembly process as well.

6.2.2: Nanoscale boiling and bubble formation

The nanoaquarium provides a platform for studying boiling and bubble formation on the nanoscale. Future versions of the device can be modified to include resistive heaters to precisely control the temperature in the imaging chamber. However, even with the current design the device can readily be used to study electron beam-induced boiling

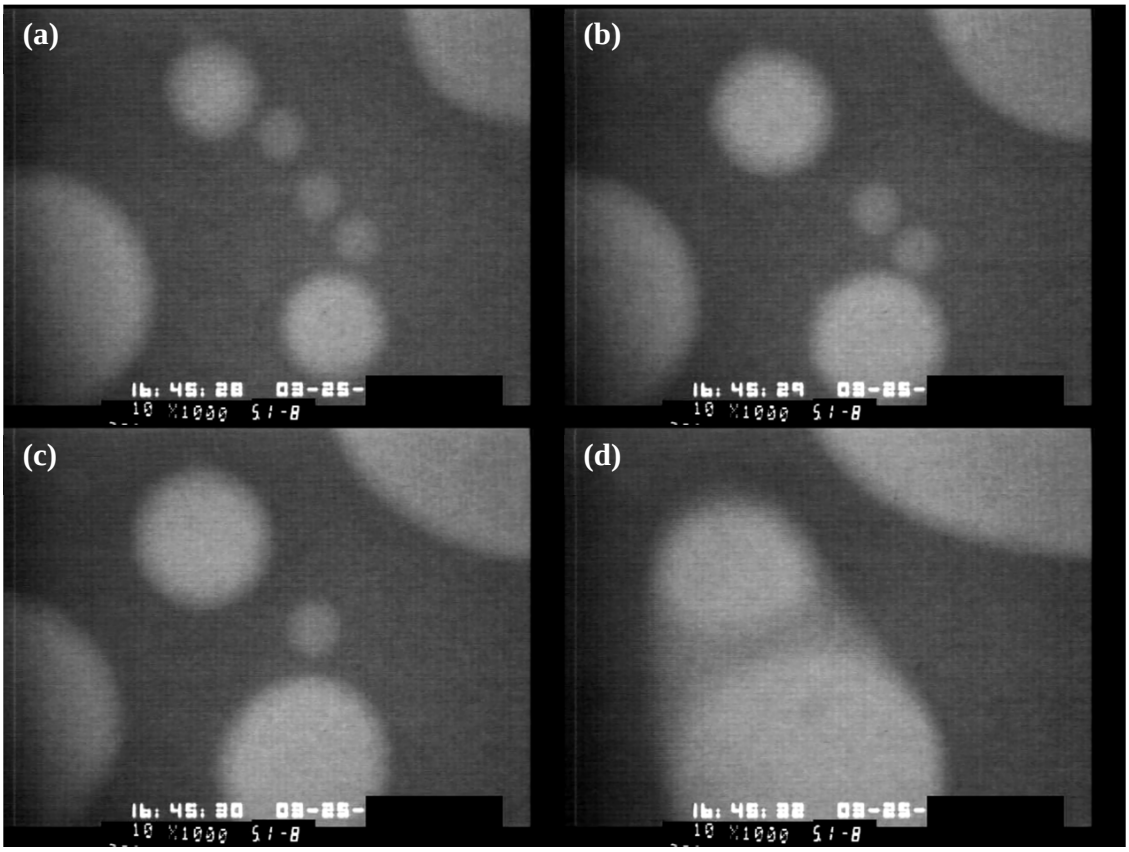

Figure 6-2: Series of bright field TEM images (Hitachi H9000) of beam-induced bubble formation in the nanoaquarium with a solution of ZnO-KOH electrolyte. Horizontal field of view in each image is 985 nm. 1 second elapses between frames (a), (b) and (c), and 2 seconds elapse between frames (c) and (d). Images courtesy of Dr. Frances M. Ross (IBM).

and bubble formation. Using our nanoaquarium in a TEM (Hitachi H9000) with high acceleration voltage (up to 300 kV), Dr. Frances M. Ross at the IBM T. J. Watson research center was able to controllably generate bubbles under certain circumstances. An example of bubble generation in a ZnO-KOH electrolyte solution is shown in Figure 6-2. Further investigation is needed to understand the source of the bubbles in Figure 6-2, but possible explanations include boiling, radiolysis, or a change in gas solubility in the liquid with temperature that caused dissolved gas to come out of solution. The nanoaquarium can also be used to study heterogeneous nucleation and boiling from surfaces patterned to enhance boiling and reduce the superheat that is needed to sustain the boiling process.

6.2.3: Electrochemical processes

As demonstrated in Section 2.11, the integrated electrodes of the nanoaquarium can be used to apply electric potential *in situ* in order to sense and actuate electrochemical processes (see Figure 2-19 – Figure 2-21 for examples of *in situ* electrochemical deposition of copper). The nanoaquarium can thus be used to characterize the morphology and kinetics of various electrochemical deposition processes. The results of which can be used to design deposition processes with desired outcomes (perhaps a continuous film is desirable for one application but a distributed array of individual islands is desirable for another application). Conditions for dendritic growth of a material system can be ascertained. Electrochemical etching processes can be studied as well, along with systems that cycle between periods of deposition and etching (e.g. batteries). Interesting problems in cycling systems include issues of dendritic growth

during deposition (often undesirable) and how to modify the stripping cycle in order to remove the dendritic features (simple uniform stripping often leaves islands of material from the dendrite when the feature becomes detached from the electric potential source, i.e., the electrode).

6.2.4: Biological systems

Another field of research where the nanoaquarium will be useful is in the study of nanoscale biological interactions. Subcellular biological studies involving systems such as DNA, motor proteins, cytoskeletal filaments, or organelles such as ribosomes are currently performed dynamically through fluorescent labeling (fluorophores or quantum dots) and observation with an optical microscope, or statically through high atomic number staining and complicated sample preparation (e.g., freeze drying and thin sectioning) and observation with an electron microscope. Despite the diffraction limited resolution of light, optical microscope studies of single molecules can be localized with nanometer resolution by understanding the point spread function of a fluorescing point source and backing out the source's position. However, this approach fails to distinguish closely spaced neighbors and does not provide detailed information on conformational and structural changes. With the nanoaquarium, we hope to perform dynamical experiments on biological systems (e.g., myosin motor proteins walking on actin filaments) in the (S)TEM with nanoscale resolution of all features. Several issues must be addressed to facility *in situ* (S)TEM studies of biological samples. Staining techniques for the electron microscope must be developed that produce reasonable contrast while retaining biological function of the stained feature. Staining could be in the form of a

molecular stain that coats the entire surface of a sample and is able to penetrate into small features, or in the form of high contrast particle labels (e.g., gold) at select points on a sample. The interaction of the electron beam with biological samples must be explored. Will the beam cause radiation damage to the sample? If so, with what consequence and can this harmful effect be mitigated by modifying the electron beam imaging conditions?

Appendix

Appendix A: Image processing, image analysis, and data fitting for diffusion limited aggregation in Section 3.3.

ImageJ (version 1.37) was used to perform the image processing and analysis of the grayscale STEM images. The raw footage was processed by smoothing the data with a median filter, subtracting the background, adjusting brightness and contrast, and thresholding to produce a binary image. Analysis was performed on the binary images using the fractal analysis plugin "FracLac for ImageJ," along with ImageJ's built in "Analyze Particles" function. FracLac's subscan function was used with the particle analyzer option enabled to isolate individual clusters and then calculate the fractal dimension using a box counting algorithm. To investigate the effect of thresholding level on the results, image analysis was carried out with the "auto" ("default") threshold setting T_0 (based on the modified IsoData method as explained on the ImageJ website) as well as threshold values of $T_0 \pm 0.1*T_0$ and $T_0 \pm 0.2*T_0$, which resulted in five image sets. The five sets of data obtained from the same footage were used to generate the mean values and the standard deviations for the fitted values. The data presented in Figure 3-3 is for the image set processed with a threshold setting of T_0.

Fitting of the data was performed in Matlab using the Curve Fitting Toolbox. The measured number of clusters was correlated with an expression of the form:

$$N(t) = (N_0 - 1)(t + t_0 + 1)^b + 1. \quad \text{(A-1)}$$

Both t_0 and the exponent b were fitted using least squares. Assuming $b < 0$, equation (A-1) satisfies the requirement that after a long time all of the particles/clusters aggregate

into a single cluster $N(\infty) = 1$, and that at the beginning of the aggregation process $N(-t_0) = N_0 >> 1$ is the number of individual primary particles within the observation volume. The total number of particles, whether they are in a cluster or not yet aggregated, is constant due to conservation of mass. This assumes that particles/clusters that move out of the field of view are balanced by particles/clusters that move into the field of view, which is supported by Figure 3-3(a). N_0 was determined by counting the total foreground pixels in an image frame and then dividing by the number of pixels for a single primary particle. This value was computed for each frame of the video and then averaged to give an overall value for N_0.

Similarly, the mean cluster size was correlated with

$$S(t) = a \cdot (t + t_0 + 1)^b + 1 - a \,, \tag{A-2}$$

where a and b are fitted. The same t_0 value was used as in equation (A-1). The form of equation (A-2) was selected so that the average cluster at the beginning of the aggregation process is comprised of a single particle, i.e., $S(-t_0) = 1$.

Finally, the average cluster radius, normalized with the primary particle radius ($R_0 = 2.5$ nm), was correlated with

$$R(t)/R_0 = a \cdot (t + t_0 + 1)^b + 1 - a \,, \tag{A-3}$$

where a and b are obtained by least square fitting. The form of expression (A-3) was selected so that the radius of an average cluster at the beginning of the aggregation process is equivalent to the radius of a single particle, i.e. $R(-t_0)/R_0 = 1$.

Appendix B: Image processing and image analysis for capillary-convective assembly in Section 5.1

Video from the microscope was recorded and used for analysis. The video capture rate was fixed by the software (100 fps, 10 ms/frame) and was not synchronized to the frame rate for the microscope image (117 ms/frame, 317 ms/frame, or 967 ms/frame). The lack of synchronization, while undesirable, was at least in favor of oversampling the data. The video was in a compressed format and had to be uncompressed so that the images could be read by Matlab and ImageJ. VirtualDub 1.9.11 was used to generate individual PNG files, sampled at a rate of 10 fps.

ImageJ 1.37 was used with a macro script to automate the processing of over 100,000 images. Images were smoothed with a 2 pixel median filter, background was subtracted with a "rolling ball" algorithm, and then they were inverted and saved as 8-bit TIFF's for further analysis.

Particle and cluster tacking was performed by two methods. In the first method, ImageJ was used to threshold the images and the built-in particle analyzer was used to track the number of distinct objects (particles or clusters) and their size in each frame. By thresholding the image, aggregates that contained multiple individual particles became a single entity, and so this approach was good for tracking clusters, but not individual particles. See Figure B-1 for an example.

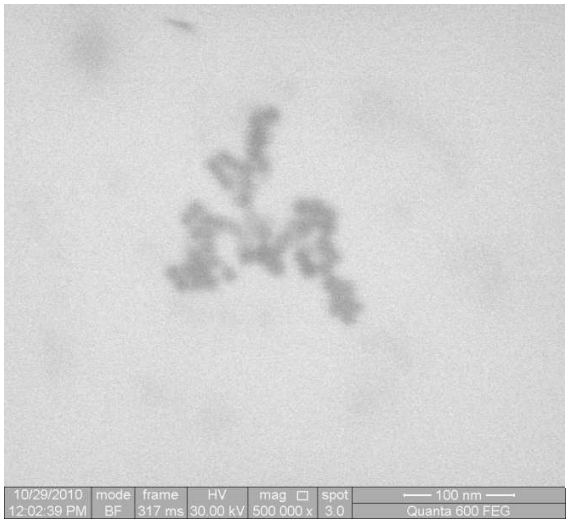

Figure B-1: Example of an unprocessed image (L) and the same image after processing and thresholding in ImageJ (R).

In the second method, Matlab was used for particle tracking on the processed TIFF's using code developed by the Maria Kilfoil research group [87]. The Kilfoil code was adapted from particle tracking code using IDL, developed by David Grier, John Crocker, and Eric Weeks [109]. Details of the code and tutorials on how to use it can be found on the respective websites for each group. Briefly, the methodology is as follows. First, a single frame from a batch of interest is read into the program and the user adjusts various settings (particle size and shape, pixel intensity, etc) until the program successfully finds the particles of interest. The code looks for particles as light pixels on a dark background, as would be generated from fluorescent microscopy (hence the need to invert the STEM images). The batch of images is then processed using the settings decided on in the first frame. The coordinates for the particles in each frame are linked to coordinates in other frames based on user input (e.g., max displacement between frames) so as to form trajectories. The final output from the Kilfoil code is a matrix called "res"

that contains the following information: columns 1 and 2 are the x and y positions (in pixels); column 3 is the integrated intensity; column 4 is the radius of gyration squared (pixel squared); column 5 is the eccentricity; column 6 is the frame number in which the feature was found; column 7 is the time at which the image was recorded; and column 8 is the trajectory ID number. The user must then manipulate this "res" matrix as he/she sees fit to extract the information of interest (e.g., position of particles, distance between particles, velocities, etc). In contrast to the first method with ImageJ, this method preserves individual particle identification even when the particle becomes part of a cluster (so long as the particle doesn't deform or coalesce as bubbles would).

As mentioned at the beginning of this section, there was an issue with unsynchronized frame rates for the video and oversampling of the images. As a result of the oversampling, there were frequent frame repeats. For example, if the microscope was rastering at a frame rate of about 3 fps (a common setting for these experiments) then the uncompressed frames that were used for image analysis, which were sampled at 10 fps, contained 7 repeat frames for every 3 unique frames. The repeat frames were not a problem for measuring quantities such as cluster size, cluster count or mean distance between particles. However, the repeat frames did present a problem for calculating particle velocity. Velocity was calculated by measuring the displacement of a particle from one frame to the next and dividing it by the time step determined by the frame rate (0.1 seconds for 10 fps). But with many repeat frames present due to oversampling, the velocity calculations contained frequent zero velocity frames where it appeared as if

nothing moved. This erroneous artifact was a consequence of oversampling the images. The Matlab code was modified to address this issue in the following manner:

- Take frame i and compare it to frame $i + 1$ by calculating a displacement vector, where each row contains displacement information for a particle in the image.
- If the sum of the displacement vector is non-zero, then frame i and frame $i + 1$ are not duplicates and the velocity calculation can proceed by dividing the displacement vector by the time step to get the velocity vector.
- If the sum of the displacement vector is zero, then frame $i + 1$ is a duplicate of frame i. Even if one were to scan a completely static object twice in a row, there would be enough noise/drift to produce an image that differs by at least a few pixels. So a zero sum displacement vector indicates an identical repeat frame. A value of 1 is added to a counter and the velocity calculation is postponed.
- The next set of images is compared, frame $i + 1$ to frame $i + 2$. If this is another pair of repeat frames then another 1 is added to the counter and the velocity calculation is postponed.
- The code continues to compare frames and postpone the velocity calculation until the sum of the displacement vector is non-zero, indicating that a pair of non-repeat frames has been reached. The velocity is then

calculated by dividing the displacement vector by (the time step * (the counter value +1)).

- The velocity calculation performed on the non-repeat frames is used to fill in values for velocity in the current frame and the previous number of duplicate frames given by the counter. This spreads out the displacement, and subsequent velocity, measured in the last pair of frames over all the previous duplicate frames.
- The counter is reset to zero, and the cycle continues.

Appendix C: Normalization term for measuring the mean distance between particles

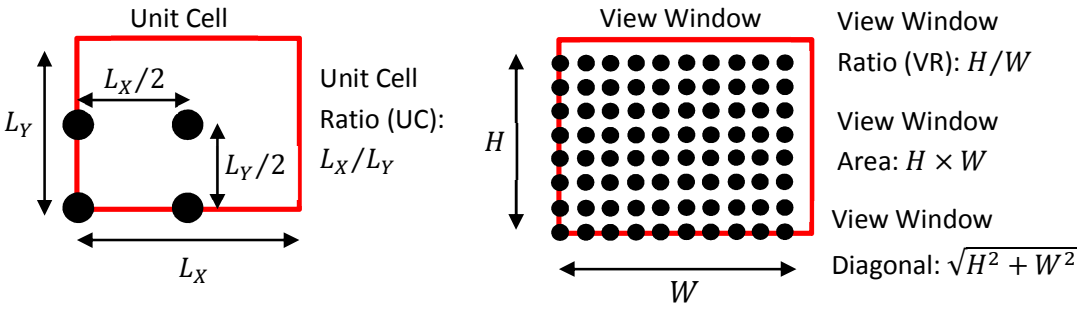

Total number of particles: N

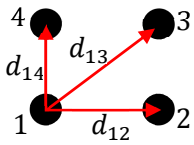

Mean Distance for particle i: $\bar{d}_i = \frac{1}{N-1} \sum_{j=1}^{N} d_{ij}$

e.g., Mean Distance for particle 1: $\overline{d_1} = \frac{d_{11}+d_{12}+d_{13}+d_{14}}{3}$

Ensemble Mean Distance: $\bar{d} = \frac{1}{N} \sum_{i=1}^{N} \bar{d}_i$

For a given system of particles on a grid, as the size of the viewing window increases, so does the total number of particles in view (N), aka particle count. As a

result, the ensemble mean distance, $\bar{d}$, increases because there are more particles located further away from each other. When looking at two images of the same system at different magnifications, the $\bar{d}$ that is measured will be different. Yet these two images represent the same system at the same condition. Thus $\bar{d}$ must be scaled in such a way that the measurement is independent of magnification.

Matlab was used to investigate the relationship between $\bar{d}$ and view window size under various system conditions/factors such as the unit cell size and shape (L_X and L_Y values, which affect concentration), and view window shape (VR: H/W). In each case, the unit cell ratio (L_X/L_Y), and view window ratio (H/W) values were fixed and the size of the view window was varied (i.e., H was varied). $\bar{d}$ was calculated for each view window size and plotted as a function of different variables in order to investigate relationships and find trends. The following plots represent one such case where the unit cell ratio (UC) is 1 with $L_X = 1$ and $L_Y = 1$, and the view window ratio (VR) is 1 ($H/W = 1$).

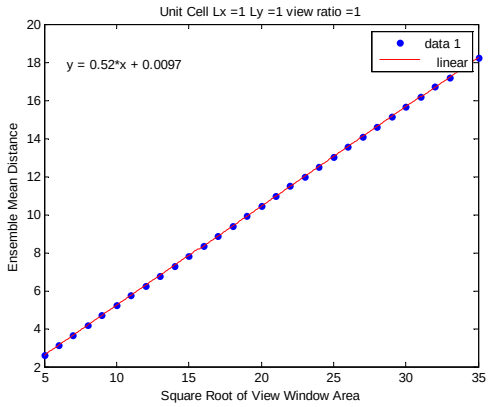

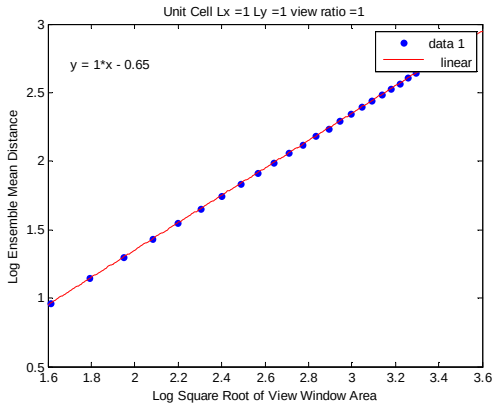

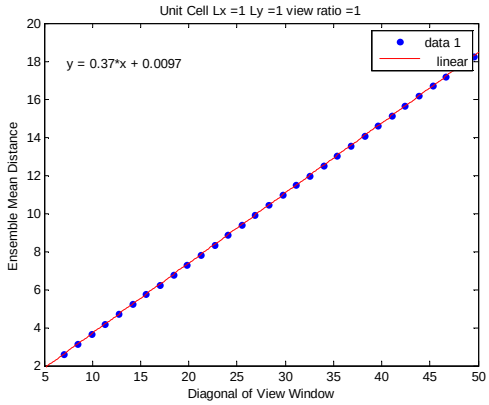

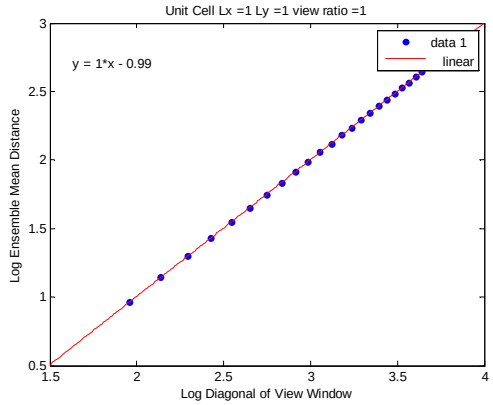

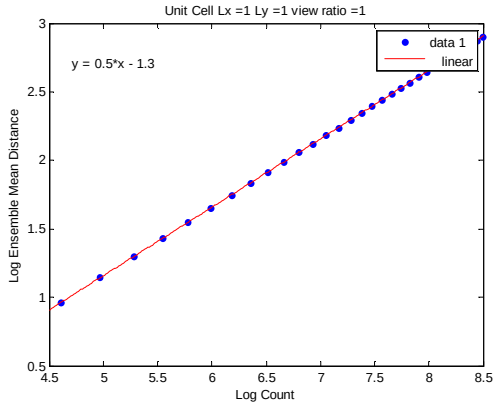

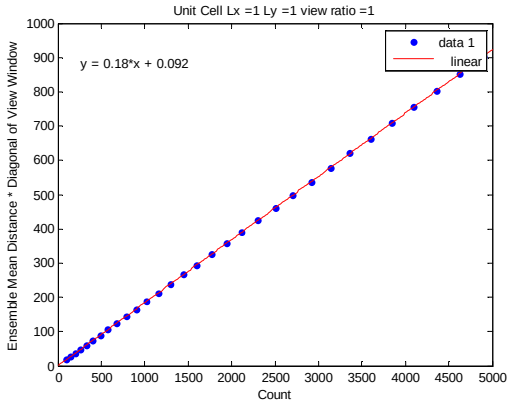

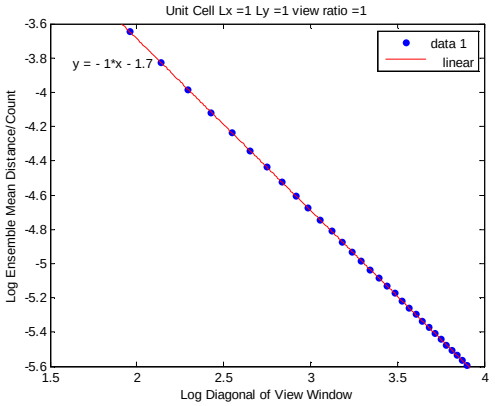

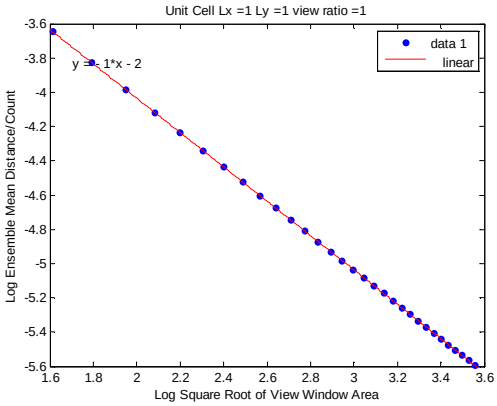

The following table depicts results for all of the systems tested:

Unit Cell Ratio			EMD vs Sqrt(Area)		Log(EMD) vs Log(Sqrt(Area))		EMD vs Diagonal		Log(EMD) vs Log(Diagonal)		Log(EMD) vs Log(Count)		EMD * Diag vs Count		Log(EMD/Count) vs Log(Diagonal)		Log(EMD/Count) vs Log(Sqrt(Area))	
Ly	Lx	VR	Slope	Intercept	Slope	Intercept	Slope	Intercept	Slope	Intercept	Slope	Intercept	Slope	Intercept	Slope	Intercept	Slope	Intercept
0.5	0.5	1	0.5213	0.0025	0.9996	-0.6497	0.3686	0.0025	0.9996	-0.9962	0.4998	-2.0354	0.0461	0.0236	-1.0004	-3.0756	-1.0004	-3.4223
0.5	0.5	2	0.5690	0.0021	0.9997	-0.5629	0.3599	0.0021	0.9997	-1.0209	0.4999	-1.9488	0.0562	0.0320	-1.0003	-2.8772	-1.0003	-3.3354
0.5	0.5	4	0.7137	0.0027	0.9998	-0.3365	0.3462	0.0027	0.9998	-1.0598	0.4999	-1.7225	0.0920	0.0629	-1.0002	-2.3855	-1.0002	-3.1091
0.5	0.5	6	0.8463	0.0033	0.9998	-0.1661	0.3408	0.0033	0.9998	-1.0755	0.4999	-1.5522	0.1314	0.0987	-1.0002	-2.0290	-1.0002	-2.9387
0.5	0.5	8	0.9641	0.0040	0.9998	-0.0358	0.3382	0.0040	0.9998	-1.0830	0.4999	-1.4218	0.1718	0.1364	-1.0002	-1.7607	-1.0002	-2.8083
2	2	1	0.5204	0.0366	0.9935	-0.6297	0.3680	0.0366	0.9935	-0.9741	0.4968	-0.6297	0.7374	0.3541	-1.0065	-0.2809	-1.0065	-0.6297
2	2	2	0.5684	0.0325	0.9962	-0.5499	0.3595	0.0325	0.9962	-1.0064	0.4981	-0.5499	0.8998	0.4930	-1.0038	-0.0901	-1.0038	-0.5499
2	2	4	0.7133	0.0357	0.9976	-0.3278	0.3460	0.0357	0.9976	-1.0496	0.4988	-0.3278	1.4714	0.9908	-1.0024	0.3974	-1.0024	-0.3278
2	2	6	0.8459	0.0383	0.9983	-0.1595	0.3407	0.0383	0.9983	-1.0675	0.4991	-0.1595	2.1018	1.5652	-1.0017	0.7517	-1.0017	-0.1595
2	2	8	0.9638	0.0401	0.9986	-0.0304	0.3381	0.0401	0.9986	-1.0764	0.4993	-0.0304	2.7484	2.1692	-1.0014	1.0185	-1.0014	-0.0304
1	1	1	0.5211	0.0097	0.9983	-0.6455	0.3685	0.0097	0.9983	-0.9915	0.4991	-1.3374	0.1843	0.0925	-1.0017	-1.6846	-1.0017	-2.0318
1	1	2	0.5689	0.0084	0.9990	-0.5602	0.3598	0.0084	0.9990	-1.0179	0.4995	-1.2526	0.2249	0.1264	-1.0010	-1.4879	-1.0010	-1.9465
1	1	4	0.7136	0.0090	0.9994	-0.3348	0.3462	0.0090	0.9994	-1.0579	0.4997	-1.0276	0.3679	0.2505	-1.0006	-0.9972	-1.0006	-1.7211
1	1	6	0.8463	0.0097	0.9996	-0.1650	0.3408	0.0097	0.9996	-1.0741	0.4998	-0.8578	0.5254	0.3940	-1.0004	-0.6413	-1.0004	-1.5512
1	1	8	0.9641	0.0101	0.9996	-0.0349	0.3382	0.0101	0.9996	-1.0820	0.4998	-0.7278	0.6871	0.5450	-1.0004	-0.3734	-1.0004	-1.4212
1	2	1	0.5210	0.0137	0.9976	-0.6432	0.3684	0.0137	0.9976	-0.9890	0.4988	-0.9890	0.3687	0.1337	-1.0024	-0.9890	-1.0024	-1.3364
1	2	2	0.5688	0.0147	0.9983	-0.5575	0.3597	0.0147	0.9983	-1.0149	0.4991	-0.9035	0.4499	0.2232	-1.0017	-0.7917	-1.0017	-1.2507
1	2	4	0.7135	0.0177	0.9988	-0.3325	0.3461	0.0177	0.9988	-1.0552	0.4994	-0.6787	0.7357	0.4917	-1.0012	-0.3014	-1.0012	-1.0257
1	2	6	0.8461	0.0194	0.9991	-0.1631	0.3407	0.0194	0.9991	-1.0719	0.4996	-0.5094	1.0509	0.7919	-1.0009	0.0541	-1.0009	-0.8562
1	2	8	0.9640	0.0204	0.9993	-0.0334	0.3382	0.0204	0.9993	-1.0801	0.4996	-0.3797	1.3742	1.1037	-1.0007	0.3217	-1.0007	-0.7265
1	4	1	0.5219	-0.1489	1.0276	-0.7496	0.3691	-0.1489	1.0276	-1.1058	0.5011	-0.6581	0.7422	1.4867	-1.0231	-0.2124	-1.0231	-0.567
1	4	2	0.5689	0.0079	0.9992	-0.5608	0.3598	0.0079	0.9992	-1.0186	0.4996	-0.5608	0.8998	0.1366	-1.0008	-0.1023	-1.0008	-0.5608
1	4	4	0.7134	0.0248	0.9984	-0.3308	0.3461	0.0248	0.9984	-1.0531	0.4992	-0.3308	1.4714	0.7010	-1.0016	0.3939	-1.0016	-0.3308
1	4	6	0.8460	0.0319	0.9986	-0.1607	0.3407	0.0319	0.9986	-1.0690	0.4993	-0.1607	2.1018	1.3136	-1.0014	0.7502	-1.0014	-0.1607
1	4	8	0.9639	0.0358	0.9988	-0.0311	0.3381	0.0358	0.9988	-1.0773	0.4994	-0.0311	2.7484	1.9460	-1.0012	1.0177	-1.0012	-0.0311
Mean			0.7227	0.0113	0.9998	-0.3501	0.3507	0.0113	0.9998	-1.0467	0.4994	-0.8313	0.8956	0.6265	-1.0022	-0.6150	-1.0022	-1.3132
Standard Dev			0.1660	0.0350	0.0058	0.2364	0.0116	0.0350	0.0058	0.0356	0.0008	0.5698	0.7959	0.6214	0.0045	1.1532	0.0045	1.0675
Std Dev / Mean			22.97%	310.58%	0.58%	-67.52%	3.32%	310.58%	0.58%	-3.40%	0.15%	-68.54%	88.87%	99.19%	-0.45%	-187.51%	-0.45%	-81.29%

There are several conclusions to be drawn from this table and the graphs above.

- For a given system of any UC ratio and VR, as the view window increases, $\bar{d}$ scales with either linear or power law dependence on all of the variables. $\bar{d}$ scales linearly with square root of the area of the view window. $\bar{d}$ scales linearly with the diagonal of the view window. $\bar{d} \times \text{diagonal}$ scales linearly with particle count. $\bar{d}$ scales with power law dependence on particle count. $\bar{d}/\text{particle count}$ scales with power law dependence on square root of the area of the view window. $\bar{d}/\text{particle count}$ scales with power law dependence on the diagonal of the view window.
- When the concentration is changed (by changing L_X or L_Y) the new system has all the same scaling dependencies (linear or power law) as any other system, although the slopes of the dependencies may not be the same. For example, for a fixed VR, $\bar{d} \times \text{diagonal}$ vs particle count slope varies depending on the unit cell size and spacing.
- Similarly, when the view window ratio is changed, all the same variable dependencies hold true, although the slopes, again, may be different. For example, for a fixed UC, the slope of $\bar{d}$ vs square root of the area of the view window varies depending on the VR. Interestingly, when the VR is fixed and the UC is changed, the slope of $\bar{d}$ vs square root of the area of the view window appears to be constant.

- There is, however, one relationship that appears to be constant, regardless of unit cell size, unit cell shape, or view window ratio: $\bar{d}$ vs diagonal of the view window (highlighted blue in the table). Examining the highlighted columns, the relationship $\log(\bar{d}) = \log(\text{diagonal}) - 1$ can be rearranged to give $\bar{d} = \frac{1}{e} \times$ diagonal, which is confirmed by the preceding set of columns for $\bar{d}$ vs diagonal.
- It is interesting to note that the $\bar{d}$ vs diagonal relationship holds approximately true, regardless of particle concentration, as long as there is a regularly distributed system of particles. Thus, this gives a good absolute measure of aggregation. In any system, $\bar{d}/\text{diagonal}$ can at most be equal to $1/e$. Any value less than $1/e$ indicates that the system is aggregated in some way and is not in a state of even distribution. The lower bound of $\bar{d}/\text{diagonal}$ will depend on the size and shape of the particles, and how they pack with each other.

From this analysis, we can conclude that $\bar{d}$ should be scaled by the view window diagonal in order to collapse the initial $\bar{d}$ value to a normalized $\bar{d}$ value that is equivalent across different view window sizes and shapes.

Appendix D: Radial box position coordinate system

We want to explore the idea that particle motion in our system could be dependent on where the particle is located in the image. So we would like to display particle velocity as a function of radial position from the center of the image. The image, however, is not circular, but rather is a rectangle measuring 1024 pixels wide by 881

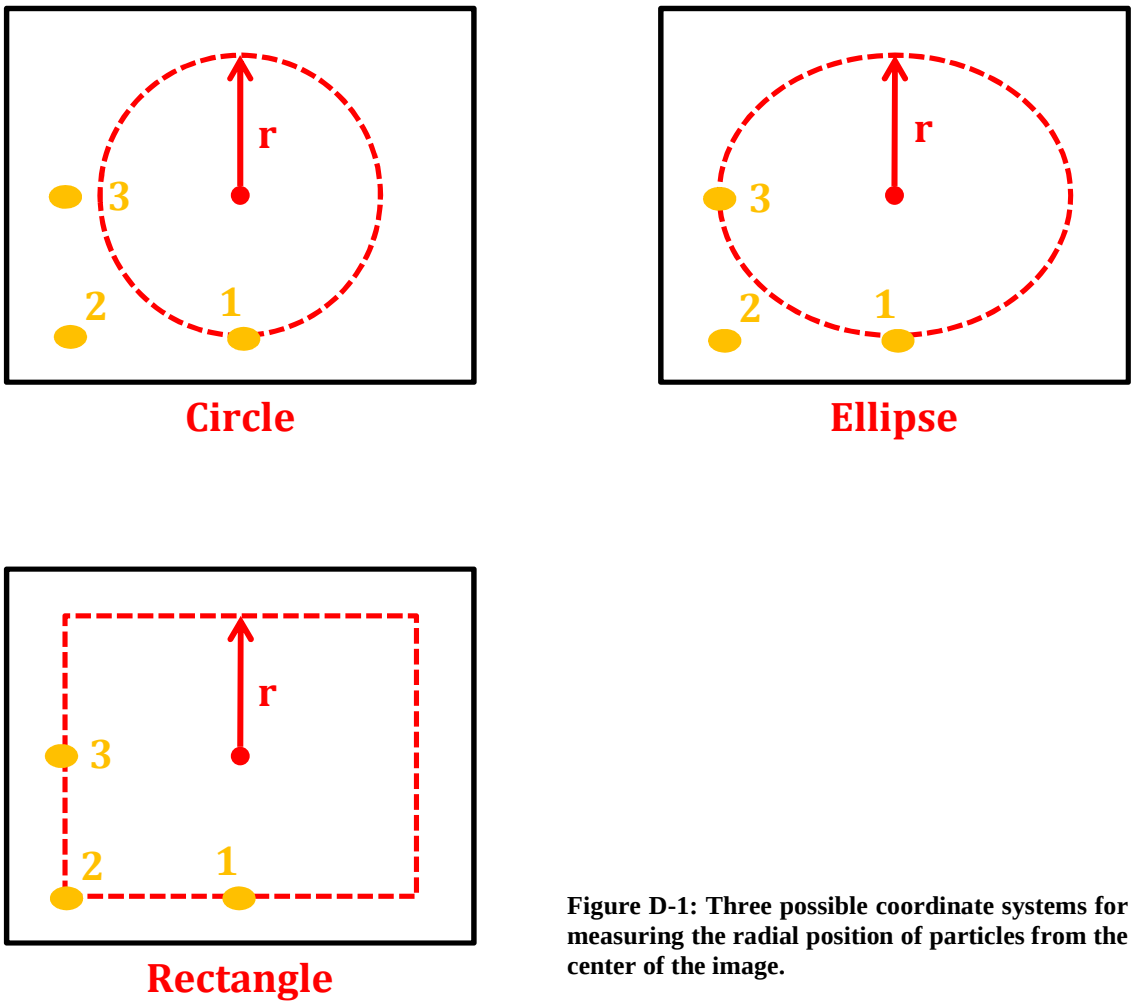

Figure D-1: Three possible coordinate systems for measuring the radial position of particles from the center of the image.

pixels tall. Three possible coordinate systems are illustrated in Figure D-1. Particles 1, 2 and 3 lie at the same distance from an edge of the image, and they should be represented by the same radial position value. A circle that sweeps out from the center of the image captures particle 1, but fails to capture particles 2 and 3 at the same radial position. An ellipse, with an aspect ratio equal to the aspect ratio of the image, that sweeps out from the center of the image captures particles 1 and 3, but fails to capture particle 2 at the same radial position. A rectangle, with an aspect ratio equal to the aspect ratio of the

image, that sweeps out from the center of the image captures particles 1, 2 and 3 at the same radial position. And so the "radial box position" was selected as the coordinate system for representing a particle's position relative to the center of the image. The radial box position of a particle was calculated in the following manner:

- Set the origin to the center of the image and calculate the x and y position relative to the origin.
- Take the absolute value of the x and y position.
- Divide the x value of the particle position by the aspect ratio ($1024/881 = 1.162$) in order to scale the x position to be in the same range as the y position.
- Compare the scaled x value to the y value and take whichever is greater, this gives the radial box position on which the particle lies.

Appendix E: Mean squared displacement due to Brownian motion

Let us consider the one-dimensional random walk of a particle due to Brownian motion, with analysis outlined in "Physicochemical Hydrodynamics" [91]. The probability of finding a particle at position x after n random steps of length l is given by the Gaussian distribution:

$$P(n,x) = (2\,\pi\,n\,l^2)^{-1/2}\,e^{-x^2/2\,n\,l^2}, \tag{E-1}$$

where the number of steps is taken to be proportional to time according to

$$n = K\,t. \tag{E-2}$$

Concentration is then represented as

$$c = c_0\, P(x,t), \tag{E-3}$$

which we plug into the 1-D diffusion equation

$$\frac{\partial c}{\partial t} = D\, \frac{\partial^2 c}{\partial x^2}, \tag{E-4}$$

where D is the diffusion coefficient, to find that

$$K = 2D/l^2. \tag{E-5}$$

Substituting equations (E-2) and (E-5) into (E-1) for a particle on a random walk in one, two, and three dimension produces, respectively,

$$P_{1D}(x,t) = \frac{1}{(4\,\pi\,D\,t)^{1/2}}\; e^{-x^2/4\,D\,t}, \tag{E-6}$$

$$P_{2D}(x,y,t) = \frac{1}{(4\,\pi\,D\,t)}\; e^{-(x^2+y^2)/4\,D\,t}, \tag{E-7}$$

$$P_{3D}(x,y,z,t) = \frac{1}{(4\,\pi\,D\,t)^{3/2}}\; e^{-(x^2+y^2+z^2)/4\,D\,t}. \tag{E-8}$$

The integral of each probability over its domain must be 1, i.e.,

$$\int P_{1D}(x,t)\,dx = 1, \tag{E-9}$$

$$\iint P_{2D}(x,y,t)\,dx\,dy = 1, \tag{E-10}$$

$$\iiint P_{3D}(x,y,z,t)\,dx\,dy\,dz = 1. \tag{E-11}$$

Converting the 2D expression in (E-10) to cylindrical coordinates and the 3D expression in (E-11) to spherical coordinates, and then integrating over the angular terms produces:

$$P_{1D}(r,t) = \frac{1}{2\,(\pi\,D\,t)^{1/2}}\; e^{-r^2/4\,D\,t}, \qquad (-\infty < r < \infty), \tag{E-12}$$

$$P_{2D}(r,t) = r\,\frac{1}{2\,(D\,t)}\; e^{-r^2/4\,D\,t}, \qquad (0 < r < \infty), \tag{E-13}$$

$$P_{3D}(r,t) = r^2 \frac{1}{2\,(\pi\, D\, t)^{1/2}}\, e^{-r^2/4\,D\,t}, \qquad (0 < r < \infty). \tag{E-14}$$

We can now calculate the mean squared displacement of a particle undergoing a random walk in 1, 2, or 3 dimensions by integrating the square of the displacement times the probability of displacement,

$$\langle r^2 \rangle = \int r^2\, P(r,t)\, dr, \tag{E-15}$$

to get

$$\langle r^2 \rangle_{1D} = 2Dt, \tag{E-16}$$

$$\langle r^2 \rangle_{2D} = 4Dt, \tag{E-17}$$

$$\langle r^2 \rangle_{3D} = 6Dt. \tag{E-18}$$

References

[1] P. G. de Gennes, "Wetting: statics and dynamics," *Reviews of Modern Physics*, vol. 57, pp. 827-863, 1985.

[2] M. L. Walker et al., "Two-headed binding of a processive myosin to F-actin," *Nature*, vol. 405, no. 6788, pp. 804-807, Jun. 2000.

[3] "How ESEM Works," *Imaging & Microscopy Facility, UC Merced*, Jun. 2003.

[4] A. Bogner, G. Thollet, D. Basset, P. H. Jouneau, and C. Gauthier, "Wet STEM: A new development in environmental SEM for imaging nano-objects included in a liquid phase," *Ultramicroscopy*, vol. 104, no. 3-4, pp. 290–301, 2005.

[5] Y. A. Cengel and M. A. Boles, *Thermodynamics: An Engineering Approach*, 3rd ed. WCB/McGraw-Hill, 1998.

[6] M. J. Williamson, R. M. Tromp, P. M. Vereecken, R. Hull, and F. M. Ross, "Dynamic microscopy of nanoscale cluster growth at the solid-liquid interface," *Nature Materials*, vol. 2, no. 8, pp. 532-536, 2003.

[7] A. Radisic, P. M. Vereecken, J. B. Hannon, P. C. Searson, and F. M. Ross, "Quantifying Electrochemical Nucleation and Growth of Nanoscale Clusters Using Real-Time Kinetic Data," *Nano Letters*, vol. 6, no. 2, pp. 238-242, Feb. 2006.

[8] K.-L. Liu et al., "Novel microchip for in situ TEM imaging of living organisms and bio-reactions in aqueous conditions," *Lab on a Chip*, vol. 8, no. 11, pp. 1915 - 1921, 2008.

[9] N. de Jonge, D. B. Peckys, G. J. Kremers, and D. W. Piston, "Electron microscopy of whole cells in liquid with nanometer resolution," *Proceedings of the National Academy of Sciences*, vol. 106, no. 7, pp. 2159-2164, Feb. 2009.

[10] H. Zheng, S. A. Claridge, A. M. Minor, A. P. Alivisatos, and U. Dahmen, "Nanocrystal Diffusion in a Liquid Thin Film Observed by in Situ Transmission Electron Microscopy," *Nano Letters*, vol. 9, no. 6, pp. 2460-2465, Jun. 2009.

[11] H. Zheng, R. K. Smith, Y.-wook Jun, C. Kisielowski, U. Dahmen, and A. P. Alivisatos, "Observation of Single Colloidal Platinum Nanocrystal Growth Trajectories," *Science*, vol. 324, no. 5932, pp. 1309-1312, Jun. 2009.

[12] J. F. Creemer et al., "Atomic-scale electron microscopy at ambient pressure," *Ultramicroscopy*, vol. 108, no. 9, pp. 993-998, Aug. 2008.

[13] J. M. Grogan and H. H. Bau, "The Nanoaquarium: A Platform for In Situ Transmission Electron Microscopy in Liquid Media," *Journal of Microelectromechanical Systems*, vol. 19, no. 4, pp. 885-894, 2010.

[14] A. Radisic, P. M. Vereecken, P. C. Searson, and F. M. Ross, "The morphology and nucleation kinetics of copper islands during electrodeposition," *Surface Science*, vol. 600, no. 9, pp. 1817-1826, May 2006.

[15] D. B. Peckys, G. M. Veith, D. C. Joy, and N. de Jonge, "Nanoscale Imaging of Whole Cells Using a Liquid Enclosure and a Scanning Transmission Electron Microscope," *PLoS ONE*, vol. 4, no. 12, p. e8214, Dec. 2009.

[16] E. A. Ring and N. de Jonge, "Microfluidic System for Transmission Electron Microscopy," *Microscopy and Microanalysis*, pp. 1–8, 2010.

[17] J. F. Creemer, S. Helveg, P. J. Kooyman, A. M. Molenbroek, H. W. Zandbergen, and P. M. Sarro, "A MEMS Reactor for Atomic-Scale Microscopy of Nanomaterials Under Industrially Relevant Conditions," *Journal of Microelectromechanical Systems*, vol. 19, no. 2, pp. 254-264, Apr. 2010.
[18] L. Mele et al., "Wafer-level assembly and sealing of a MEMS nanoreactor for in situ microscopy," *Journal of Micromechanics and Microengineering*, vol. 20, p. 085040, 2010.
[19] S. H. Christiansen, R. Singh, and U. Gosele, "Wafer Direct Bonding: From Advanced Substrate Engineering to Future Applications in Micro/Nanoelectronics," *Proceedings of the IEEE*, vol. 94, no. 12, pp. 2060-2106, 2006.
[20] X. X. Zhang and J.-P. Raskin, "Low-temperature wafer bonding: a study of void formation and influence on bonding strength," *Microelectromechanical Systems, Journal of*, vol. 14, no. 2, pp. 368-382, 2005.
[21] G. Ilicali et al., "Use of LPCVD TEOS as a direct bonding material for layer transfer: densified vs. undensified," in *SOI Conference, 2004. Proceedings. 2004 IEEE International*, 2004, pp. 44-45.
[22] T. Suni, "Direct wafer bonding for MEMS and microelectronics," Helsinki University of Technology, 2006.
[23] Q. Y. Tong, G. Cha, R. Gafiteanu, and U. Gosele, "Low temperature wafer direct bonding," *Microelectromechanical Systems, Journal of*, vol. 3, no. 1, pp. 29–35, 1994.
[24] T. Suni, K. Henttinen, A. Lipsanen, J. Dekker, H. Luoto, and M. Kulawski, "Wafer scale packaging of MEMS by using plasma-activated wafer bonding," *Journal of the Electrochemical Society*, vol. 153, no. 1, p. G78-G82, 2006.
[25] A. Doll, M. Rabold, F. Goldschmidtboing, and P. Woias, "Versatile low temperature wafer bonding and bond strength measurement by a blister test method," *Microsystem Technolgies*, vol. 12, no. 5, pp. 418-429, 2006.
[26] G. Kissinger and W. Kissinger, "Void-free silicon-wafer-bond strengthening in the 200-400 °C range," *Sensors and Actuators A: Physical*, vol. 36, no. 2, pp. 149-156, Mar. 1993.
[27] M. Wiegand et al., "Wafer bonding of silicon wafers covered with various surface layers," *Sensors and Actuators A: Physical*, vol. 86, no. 1-2, pp. 91-95, Oct. 2000.
[28] S. Mack, H. Baumann, U. Gösele, H. Werner, and R. Schlögl, "Analysis of Bonding-Related Gas Enclosure in Micromachined Cavities Sealed by Silicon Wafer Bonding," *Journal of the Electrochemical Society*, vol. 144, no. 3, pp. 1106-1111, 1997.
[29] Q. Y. Tong and U. Gösele, "Semiconductor Wafer Bonding: Science and Technology," John Wiley & Sons, Inc., 1999, p. 51.
[30] Q. Y. Tong and U. Gösele, *Semiconductor Wafer Bonding: Science and Technology*. John Wiley & Sons, Inc., 1999.
[31] R. Pelzer, H. Kirchberger, and P. Kettner, "Wafer-to-Wafer Bonding Techniques: From MEMS Packaging to IC Integration Applications," in *Electronic Packaging Technology, 2005 6th International Conference on*, 2005, pp. 1-6.

[32] J. Wei, “Wafer bonding techniques for microsystem packaging,” in *Journal of Physics: Conference Series*, 2006, vol. 34, pp. 943–948.
[33] A. Plößl and G. Kräuter, “Wafer direct bonding: tailoring adhesion between brittle materials,” *Materials Science and Engineering: R: Reports*, vol. 25, no. 1-2, pp. 1-88, Mar. 1999.
[34] M. Miyashita, T. Tusga, K. Makihara, and T. Ohmi, “Dependence of Surface Microroughness of CZ, FZ, and EPI Wafers on Wet Chemical Processing,” *Journal of The Electrochemical Society*, vol. 139, no. 8, pp. 2133-2142, 1992.
[35] Q. Y. Tong and U. Gösele, “Semiconductor Wafer Bonding: Science and Technology,” John Wiley & Sons, Inc., 1999, p. 53.
[36] H.-S. Min, Y.-C. Joo, and O.-S. Song, “Effects of Wafer Cleaning and Annealing on Glass/Silicon Wafer Direct Bonding,” *Journal of Electronic Packaging*, vol. 126, no. 1, pp. 120-123, Mar. 2004.
[37] H. Moriceau, F. Rieutord, C. Morales, and M. Charvet, “Surface plasma treatments enabling low temperature direct bonding,” *Microsystem Technolgies*, vol. 12, no. 5, pp. 378-382, 2006.
[38] S. N. Farrens, J. R. Dekker, J. K. Smith, and B. E. Roberds, “Chemical Free Room Temperature Wafer To Wafer Direct Bonding,” vol. 142, no. 11, pp. 3949 - 3955, 1995.
[39] A. Doll, F. Goldschmidtboeing, and P. Woias, “Low temperature plasma-assisted wafer bonding and bond-interface stress characterization,” in *Micro Electro Mechanical Systems, 2004. 17th IEEE International Conference on. (MEMS)*, 2004, pp. 665-668.
[40] W. P. Maszara, G. Goetz, A. Caviglia, and J. B. McKitterick, “Bonding of silicon wafers for silicon-on-insulator,” *Journal of Applied Physics*, vol. 64, no. 10, pp. 4943-4950, Nov. 1988.
[41] J. Bagdahn, M. Petzold, M. Reiche, and K. Gutjahr, “Characterization of directly bonded silicon wafers by means of the double cantilever crack opening method,” in *Proceedings of the Fourth International Symposium on Semiconductor Wafer Bonding: Science, Technology, and Applications IV*, 1998, vol. PV97-36, pp. 291-298.
[42] L. Chen, T. Chen, and L. Sun, “Measurement Method of Bond Strength for Silicon Direct Wafer Bonding,” in *Information Acquisition, 2006 IEEE International Conference on*, 2006, pp. 1021-1025.
[43] K. T. Turner and S. M. Spearing, “Accurate characterization of wafer bond toughness with the double cantilever specimen,” *Journal of Applied Physics*, vol. 103, no. 1, p. 013514, 2008.
[44] M. M. Visser, S. Weichel, R. de Reus, and A. B. Hanneborg, “Strength and leak testing of plasma activated bonded interfaces,” *Sensors and Actuators A: Physical*, vol. 97-98, pp. 434-440, Apr. 2002.
[45] D. R. Lide, “Handbook of Chemistry and Physics,” 77th ed., CDC Press, Inc., 1996, pp. 10-266.

[46] E. D. Palik, “Handbook of Optical Constants of Solids,” Academic Press, 1998, p. 774.
[47] P. Schiebener, J. Straub, J. M. H. L. Sengers, and J. S. Gallagher, “Refractive index of water and steam as function of wavelength, temperature and density,” *Journal of Physical and Chemical Reference Data*, vol. 19, no. 3, pp. 677-717, 1990.
[48] D. Maier-Schneider, J. Maibach, and E. Obermeier, “A new analytical solution for the load-deflection of square membranes,” *Microelectromechanical Systems, Journal of*, vol. 4, no. 4, pp. 238-241, 1995.
[49] A. Kaushik, H. Kahn, and A. H. Heuer, “Wafer-level mechanical characterization of silicon nitride MEMS,” *Journal of Microelectromechanical Systems*, vol. 14, no. 2, pp. 359-367, Apr. 2005.
[50] J. M. Grogan, L. Rotkina, and H. H. Bau, “In situ liquid-cell electron microscopy of colloid aggregation and growth dynamics,” *Physical Review E*, vol. 83, no. 6, Jun. 2011.
[51] D. A. Weitz and M. Oliveria, “Fractal Structures Formed by Kinetic Aggregation of Aqueous Gold Colloids,” *Physical Review Letters*, vol. 52, no. 16, p. 1433, Apr. 1984.
[52] D. A. Weitz, J. S. Huang, M. Y. Lin, and J. Sung, “Limits of the Fractal Dimension for Irreversible Kinetic Aggregation of Gold Colloids,” *Physical Review Letters*, vol. 54, no. 13, p. 1416, Apr. 1985.
[53] M. Y. Lin, H. M. Lindsay, D. A. Weitz, R. Klein, R. C. Ball, and P. Meakin, “Universal diffusion-limited colloid aggregation,” *Journal of Physics: Condensed Matter*, vol. 2, p. 3093, 1990.
[54] M. Y. Lin, H. M. Lindsay, D. A. Weitz, R. C. Ball, R. Klein, and P. Meakin, “Universality in colloid aggregation,” *Nature*, vol. 339, no. 6223, pp. 360-362, Jun. 1989.
[55] R. L. Penn, “Kinetics of Oriented Aggregation,” *The Journal of Physical Chemistry B*, vol. 108, no. 34, pp. 12707-12712, 2004.
[56] F. Huang, H. Zhang, and J. F. Banfield, “Two-Stage Crystal-Growth Kinetics Observed during Hydrothermal Coarsening of Nanocrystalline ZnS,” *Nano Letters*, vol. 3, no. 3, pp. 373-378, Mar. 2003.
[57] C. Ribeiro, E. J. H. Lee, E. Longo, and E. R. Leite, “A Kinetic Model to Describe Nanocrystal Growth by the Oriented Attachment Mechanism,” *ChemPhysChem*, vol. 6, no. 4, pp. 690-696, 2005.
[58] F. Family, P. Meakin, and J. M. Deutch, “Kinetics of Coagulation with Fragmentation: Scaling Behavior and Fluctuations,” *Physical Review Letters*, vol. 57, no. 6, p. 727, 1986.
[59] N. V. Brilliantov and P. L. Krapivsky, “Nonscaling and source-induced scaling behaviour in aggregation model of movable monomers and immovable clusters,” *Journal of Physics A: Mathematical and General*, vol. 24, pp. 4789–4803, 1991.
[60] V. Privman, D. V. Goia, J. Park, and E. Matijevic, “Mechanism of Formation of Monodispersed Colloids by Aggregation of Nanosize Precursors,” *Journal of Colloid and Interface Science*, vol. 213, no. 1, pp. 36-45, May 1999.

[61] J. Park, V. Privman, and E. Matijevic, “Model of Formation of Monodispersed Colloids,” *The Journal of Physical Chemistry B*, vol. 105, no. 47, pp. 11630-11635, Nov. 2001.
[62] T. O. Drews, M. A. Katsoulakis, and M. Tsapatsis, “A Mathematical Model for Crystal Growth by Aggregation of Precursor Metastable Nanoparticles,” *The Journal of Physical Chemistry B*, vol. 109, no. 50, pp. 23879-23887, Dec. 2005.
[63] J. Zhang, F. Huang, and L. Zhang, “Progress of nanocrystalline growth kinetics based on oriented attachment.,” *Nanoscale*, vol. 2, no. 1, pp. 18-34, 2010.
[64] K.-S. Cho, D. V. Talapin, W. Gaschler, and C. B. Murray, “Designing PbSe Nanowires and Nanorings through Oriented Attachment of Nanoparticles,” *Journal of the American Chemical Society*, vol. 127, no. 19, pp. 7140-7147, May 2005.
[65] Y.-wook Jun, M. F. Casula, J.-H. Sim, S. Y. Kim, J. Cheon, and A. P. Alivisatos, “Surfactant-Assisted Elimination of a High Energy Facet as a Means of Controlling the Shapes of TiO2 Nanocrystals,” *Journal of the American Chemical Society*, vol. 125, no. 51, pp. 15981-15985, Dec. 2003.
[66] R. L. Penn and J. F. Banfield, “Oriented attachment and growth, twinning, polytypism, and formation of metastable phases: insights from nanocrystalline TiO 2,” *Am. Mineral*, vol. 83, no. 9-10, pp. 1077–1082, 1998.
[67] R. L. Penn and J. F. Banfield, “Imperfect Oriented Attachment: Dislocation Generation in Defect-Free Nanocrystals,” *Science*, vol. 281, no. 5379, pp. 969-971, 1998.
[68] C. Ribeiro, E. Longo, and E. R. Leite, “Tailoring of heterostructures in a SnO2/TiO2 system by the oriented attachment mechanism.,” *Applied Physics Letters*, vol. 91, no. 10, p. 103105, 2007.
[69] P. Meakin, “Aggregation Kinetics,” *Physica Scripta*, vol. 46, no. 4, pp. 295-331, 1992.
[70] K. D. Hermanson, S. O. Lumsdon, J. P. Williams, E. W. Kaler, and O. D. Velev, “Dielectrophoretic Assembly of Electrically Functional Microwires from Nanoparticle Suspensions,” *Science*, vol. 294, no. 5544, pp. 1082-1086, 2001.
[71] E. U. Donev and J. T. Hastings, “Electron-Beam-Induced Deposition of Platinum from a Liquid Precursor,” *Nano Letters*, vol. 9, no. 7, pp. 2715-2718, Jul. 2009.
[72] C.-T. Pham, G. Berteloot, F. Lequeux, and L. Limat, “Dynamics of complete wetting liquid under evaporation,” *Europhysics letters*, vol. 92, no. 5, 2010.
[73] P. A. Kralchevsky and K. Nagayama, “Capillary forces between colloidal particles,” *Langmuir*, vol. 10, no. 1, pp. 23–36, 1994.
[74] K. Nagayama, “Two-dimensional self-assembly of colloids in thin liquid films* 1,” *Colloids and Surfaces A: Physicochemical and Engineering Aspects*, vol. 109, pp. 363–374, 1996.
[75] M. Yamaki, J. Higo, and K. Nagayama, “Size-dependent separation of colloidal particles in two-dimensional convective self-assembly,” *Langmuir*, vol. 11, no. 8, pp. 2975–2978, 1995.

[76] K. Chen, S. V. Stoianov, J. Bangerter, and H. D. Robinson, “Restricted meniscus convective self-assembly,” *Journal of colloid and interface science*, vol. 344, no. 2, pp. 315–320, 2010.
[77] M. I. Bodnarchuk, M. V. Kovalenko, W. Heiss, and D. V. Talapin, “Energetic and Entropic Contributions to Self-Assembly of Binary Nanocrystal Superlattices: Temperature as the Structure-Directing Factor,” *Journal of the American Chemical Society*, vol. 132, no. 34, pp. 11967-11977, 2010.
[78] Z. Zhao, J. Zhang, F. Dong, and B. Yang, “Supercrystal structures of polyhedral PbS nanocrystals,” *Journal of Colloid and Interface Science*, 2011.
[79] A. Sangani, C. Lu, K. Su, and J. Schwarz, “Capillary force on particles near a drop edge resting on a substrate and a criterion for contact line pinning,” *Physical Review E*, vol. 80, no. 1, Jul. 2009.
[80] H. Du, P. Chen, F. Liu, F.-dong Meng, T.-jin Li, and X.-yi Tang, “Preparation and assembly of nanosized polymer latex,” *Materials Chemistry and Physics*, vol. 51, no. 3, pp. 277-282, Dec. 1997.
[81] N. D. Denkov, O. D. Velev, P. A. Kralchevsky, I. B. Ivanov, H. Yoshimura, and K. Nagayama, “Two-dimensional crystallization,” *Nature*, vol. 361, no. 6407, p. 26, Jan. 1993.
[82] L. Malaquin, T. Kraus, H. Schmid, E. Delamarche, and H. Wolf, “Controlled Particle Placement through Convective and Capillary Assembly,” *Langmuir*, vol. 23, no. 23, pp. 11513-11521, Nov. 2007.
[83] F Bresme and M Oettel, “Nanoparticles at fluid interfaces,” *Journal of Physics: Condensed Matter*, vol. 19, 2007.
[84] P. A. Kralchevsky and K. Nagayama, “Capillary interactions between particles bound to interfaces, liquid films and biomembranes,” *Advances in Colloid and Interface Science*, vol. 85, no. 2-3, pp. 145–192, 2000.
[85] P. A. Kralchevsky and N. D. Denkov, “Capillary forces and structuring in layers of colloid particles,” *Current Opinion in Colloid & Interface Science*, vol. 6, no. 4, pp. 383-401, Aug. 2001.
[86] Y.-H. Ye, S. Badilescu, V.-V. Truong, P. Rochon, and A. Natansohn, “Self-assembly of colloidal spheres on patterned substrates,” *Applied Physics Letters*, vol. 79, no. 6, p. 872, 2001.
[87] “Maria Kilfoil - Software - Biological and soft condensed matter physics.” [Online]. Available: http://www.physics.mcgill.ca/~kilfoil/downloads.html. [Accessed: 02-Jun-2011].
[88] J. Israelachvili, *Intermolecular and Surface Forces*, 2nd ed. Academic Press, 2003.
[89] C. A. Miller and E. Ruckenstein, “The origin of flow during wetting of solids,” *Journal of Colloid and Interface Science*, vol. 48, no. 3, pp. 368-373, Sep. 1974.
[90] V. S. Ajaev, T. Gambaryan-Roisman, and P. Stephan, “Static and dynamic contact angles of evaporating liquids on heated surfaces,” *Journal of Colloid and Interface Science*, vol. 342, no. 2, pp. 550-558, Feb. 2010.
[91] R. F. Probstein, *Physicochemical Hydrodynamics*, 2nd ed. Wiley-Interscience, 2003.

[92] F. M. White, *Fluid Mechanics*, Fourth Edition. McGraw-Hill, 1999.
[93] K. Katoh, H. Fujita, and E. Imazu, "Motion of a Particle Floating on a Liquid Meniscus Surface," *Journal of Fluids Engineering*, vol. 114, no. 3, pp. 411-416, 1992.
[94] T. Smith, "The hydrophilic nature of a clean gold surface," *Journal of Colloid and Interface Science*, vol. 75, no. 1, pp. 51-55, May 1980.
[95] J. C. Berg, *An Introduction to Interfaces & Colloids*. World Scientific Publishing, 2010.
[96] T. Pinedo Rivera, O. Lecarme, J. Hartmann, E. Rossitto, K. Berton, and D. Peyrade, "Assisted convective-capillary force assembly of gold colloids in a microfluidic cell: Plasmonic properties of deterministic nanostructures," *Journal of Vacuum Science & Technology B: Microelectronics and Nanometer Structures*, vol. 26, no. 6, p. 2513, 2008.
[97] O. Lecarme, T. Pinedo Rivera, L. Arbez, T. Honegger, K. Berton, and D. Peyrade, "Colloidal optical waveguides with integrated local light sources built by capillary force assembly," *Journal of Vacuum Science & Technology B: Microelectronics and Nanometer Structures*, vol. 28, no. 6, p. C6O11, 2010.
[98] K. Keseroğlu and M. Çulha, "Assembly of Nanoparticles at the Contact Line of a Drying Droplet under the Influence of a Dipped Tip," *Journal of Colloid and Interface Science*, Apr. 2011.
[99] R. K. Golding, P. C. Lewis, E. Kumacheva, M. Allard, and E. H. Sargent, "In Situ Study of Colloid Crystallization in Constrained Geometry," *Langmuir*, vol. 20, no. 4, pp. 1414-1419, Feb. 2004.
[100] D. J. Harris, J. C. Conrad, and J. A. Lewis, "Evaporative lithographic patterning of binary colloidal films," *Philosophical Transactions of the Royal Society A: Mathematical, Physical and Engineering Sciences*, vol. 367, no. 1909, p. 5157, 2009.
[101] D. Harris, H. Hu, J. Conrad, and J. Lewis, "Patterning Colloidal Films via Evaporative Lithography," *Physical Review Letters*, vol. 98, no. 14, Apr. 2007.
[102] D. J. Harris and J. A. Lewis, "Marangoni Effects on Evaporative Lithographic Patterning of Colloidal Films," *Langmuir*, vol. 24, no. 8, pp. 3681-3685, Apr. 2008.
[103] Z. Tang, N. A. Kotov, and M. Giersig, "Spontaneous Organization of Single CdTe Nanoparticles into Luminescent Nanowires," *Science*, vol. 297, no. 5579, pp. 237-240, 2002.
[104] R. L. Penn and J. F. Banfield, "Morphology development and crystal growth in nanocrystalline aggregates under hydrothermal conditions: insights from titania," *Geochimica et Cosmochimica Acta*, vol. 63, no. 10, pp. 1549-1557, May 1999.
[105] Z. L. Wang, "Transmission Electron Microscopy of Shape-Controlled Nanocrystals and Their Assemblies," *The Journal of Physical Chemistry B*, vol. 104, no. 6, pp. 1153-1175, Feb. 2000.
[106] J. T. Sampanthar and H. C. Zeng, "Arresting Butterfly-Like Intermediate Nanocrystals of β-Co(OH)2 via Ethylenediamine-Mediated Synthesis," *Journal of the American Chemical Society*, vol. 124, no. 23, pp. 6668-6675, Jun. 2002.

[107] X. W. Lou and H. C. Zeng, “Complex α-MoO3 Nanostructures with External Bonding Capacity for Self-Assembly,” *Journal of the American Chemical Society*, vol. 125, no. 9, pp. 2697-2704, Mar. 2003.
[108] B. A. Korgel and D. Fitzmaurice, “Self-Assembly of Silver Nanocrystals into Two-Dimensional Nanowire Arrays,” *Advanced Materials*, vol. 10, no. 9, pp. 661-665, 1998.
[109] “Particle tracking using IDL.” [Online]. Available: http://www.physics.emory.edu/~weeks/idl/. [Accessed: 02-Jun-2011].